NTech
Lehrstuhl für
Nukleartechnik

Technische Universität München

Lehrstuhl für Nukleartechnik
Fakultät für Maschinenwesen

# Validation of the TRACE Code for the System Dynamic Simulations of the Molten Salt Reactor Experiment and the Preliminary Study on the Dual Fluid Molten Salt Reactor

Xun He

Vollständiger Abdruck der von der Fakultät für Maschinenwesen der Technischen Universität München zur Erlangung des akademischen Grades eines

Doktor-Ingenieurs (Dr. –Ing.)

genehmigten Dissertation.

| | |
|---|---|
| Vorsitzender: | Univ.-Prof. Wolfgang Polifke, Ph. D. |
| Prüfer der Dissertation | 1. Univ.-Prof. Rafael Macián-Juan, Ph. D. |
| | 2. Prof. Dr. Konrad Czerski, Universität Stettin, Stettin, Polen |

Die Dissertation wurde am 28.01.2016 bei der Technischen Universität München eingereicht und durch die Fakultät für Maschinenwesen am 14.06.2016 angenommen.

# Erklärung

Hiermit versichere ich, die vorliegende Arbeit selbstständig und ohne Hilfe Dritter angefertigt zu haben. Gedanken und Zitate, die ich aus fremden Quellen direkt oder indirekt übernommen habe, sind als solche kenntlich gemacht. Diese Arbeit hat in gleicher oder ähnlicher Form noch keiner Prüfungsbehörde vorgelegen und wurde bisher nicht veröffentlicht.

Ich erkläre mich damit einverstanden, dass die Arbeit durch den Lehrstuhl für Nukleartechnik der öffentlichkeit zugänglich gemacht werden kann.

München, den 03.07.2016

Xun HE

# Acknowledgment

Hereby I would like to express a great appreciation to my supervisor, Prof. Macián-Juan, who gave me a lot of support, freedom as well as the specific guidance during my Ph.D. study. I feel quite comfortable and motivated to work under his supervision and it is my great honor of being his student.

Second, I will thank Dr. Seidl, my second supervisor and sponsor, who truly taught me a lot of specific knowledges about the nuclear engineering. His strictness always reminds me to work hard and his huge passion for the nuclear engineering encourages me all the time. For me he becomes not only the mentor but also the friend and doubtless it is my great honor and luck once of being the student of him.

Third, I also want to thank Mr. Zhuoqi Du, my colleague and sincere, dependable friend. We always have cordial and efficient cooperations.

Furthermore, I would like to appreciate my parents for all they have done in my life until now.

Finally, my special acknowledgment goes to my wife, Aiyu. Without her love, patience, giving and support I couldn't finish my Ph.D. so smoothly.

# Abstract

Molten Salt Reactor (MSR), which was confirmed as one of the six Generation IV reactor types by the GIF (Generation IV International Forum in 2008), recently draws a lot of attention all around the world. Due to the application of liquid fuels the MSR can be regarded as the most special one among those six GEN-IV reactor types in a sense. A unique advantage of using liquid nuclear fuel lies in that the core melting accident can be thoroughly eliminated. Besides, a molten salt reactor can have several fuel options, for instance, the fuel can be based on $^{235}$U, $^{232}$Th-$^{233}$U, $^{238}$U-$^{239}$Pu cycle or even the spent nuclear fuel (SNF), so the reactor can be operated as a breeder or as an actinides burner both with fast, thermal or epi-thermal neutron spectrum and hence, it has excellent features of the fuel sustainability and for the non-proliferation. Furthermore, the lower operating pressure not only means a lower risk of the explosion as well as the radioactive leakage but also implies that the reactor vessel and its components can be lightweight, thus lowering the cost of equipments.

So far there is no commercial MSR being operated. However, the MSR concept and its technical validation dates back to the 1960s to 1970s, when the scientists and engineers from ORNL (Oak Ridge National Laboratory) in the United States managed to build and run the world's first civilian molten salt reactor called MSRE (Molten Salt Reactor Experiment). The MSRE was an experimental liquid-fueled reactor with 10MW thermal output using $^{4}$LiF-$BeF_2$-$ZrF_4$-$UF_4$ as the fuel also as the coolant itself. The MSRE is usually taken as a very important reference case for many current researches to validate their codes and simulations. Without exception it works also as a benchmark for this thesis.

The current thesis actually consists of two main parts. The first part is about the validation of the current code for the old MSRE concept, while the second one is

about the demonstration of a new MSR concept using the mathematic tools.

In particular, the aim of the first part is to demonstrate the suitability of the TRACE code for the similar MSR designs by using a modified version of the TRACE code to implement the simulations for the steady-state, transient and accidental conditions. The basic approach of this part is to couple the thermal-hydraulic model and the modified point-kinetic model. The equivalent thermal-hydraulic model of the MSRE was built in 1D with three loops including all the critical main components. The point-kinetic model was improved through considering the precursor drift in order to produce more practical results in terms of the delayed neutron behavior. Additionally, new working fluids, namely the molten salts, were embedded into the source code of TRACE. Most results of the simulations show good agreements with the ORNL's reports and with another recent study and the errors were predictable and in an acceptable range. Therefore, the necessary code modification of TRACE appears to be successful and the model will be refined and its functions will be extended further in order to investigate new MSR design.

Another part of this thesis is to implement a preliminary study on a new concept of molten salt reactor, namely the Dual Fluid Reactor (DFR). The DFR belongs to the group of the molten salt fast reactors (MSFR) and it is recently considered to be an option of minimum-waste and inherently safe operation of the nuclear reactors in the future. The DFR is using two separately circulating fluids in the reactor core. One is the fuel salt based on the mixture of tri-chlorides of uranium and plutonium ($UCl_3$-$PuCl_3$), while another is the coolant composed of the pure lead (Pb). The current work focuses on the basic dynamic behavior of a scaled-down DFR with 500MW thermal output (DFR-500) instead of its reference design with 3000MW thermal output (DFR-3000). For this purpose 10 parallel single fuel channels, as the representative samples, were selected from different core regions. Moreover, the 2D/1D coupled-physical models were developed both for steady state and transient simulations. The Monte Carlo code SERPENT was applied to do the reactor physics evaluation, while other mathematic tools, such as MATLAB® or MATHCAD® were used to perform the coupled-physical simulations. The criticality and heat transfer calculations were done to prove the feasibility of the DFR, while the transient/accidental simulations evaluated the safety-related characteristics of

the DFR. The results of the simulations were qualitatively comparable with other MSFR's design and thereby can be used initially as a reference case for future studies.

**Keyword:** Molten Salt Reactor, Dual Fluid Reactor, Coupled-physical Simulation, System Dynamics, TRACE, SERPENT, MATLAB, MATHCAD

# Contents

# List of Figures

# List of Tables

# List of Acronyms

| | |
|---|---|
| **AERE** | Atomic Energy Research Establishment |
| **ANP** | Aircraft Nuclear Propulsion |
| **ARE** | Aircraft Reactor Experiment |
| **BDF** | Backward Differentiation Formula |
| **BEU** | Backward Euler method |
| **BUL** | Bulirsch-Stöer method |
| **BWR** | Boiling Water Reactor |
| **CAMP** | Code Application and Maintenance Program |
| **CAS** | Chinese Academy of Sciences |
| **CPS** | Coolant Pump Shutdown accident |
| **DDE** | Delayed Differential Equation |
| **DFR** | Dual Fluid Reactor |
| **DMSR** | Denatured Molten Salt Reactor |
| **DNP** | Delayed Neutron Precursor |
| **DOE** | Department of Energy (U. S.) |
| **EVOL** | Evaluation and Viability of Liquid fuel fast reactor system |
| **FEU** | Forward Euler method |
| **FHR** | Fluoride salt-cooled High temperature Reactor |

**FPS** Fuel Pump Shutdown accident

**GBS** Gragg-Bulirsch-Stöer method

**GEN-IV** Generation IV

**GIF** Generation IV International Forum

**HTGR** High Temperature Gas-cooled Reactor

**HTRE** Heat Transfer Reactor Experiment

**IFK** Institute für Festkörper-Kernphysik

**IHX** Intermediate Heat Exchanger

**IMSR** Integrated Molten Salt Reactor

**INL** Idaho National Laboratory

**IVP** Initial Value Problem

**LFTR** Liquid Fluoride Thorium Reactor

**LOCA** Loss of Coolant Accident

**LWR** Light Water Reactor

**MARS** Minor Actinides Recycling in Molten Salt

**MOSART** Molten Salt Actinides Recycler and Transmuter

**MOX** Mixed Dioxide

**MPI** Message Passing Interface

**MSFR** Molten Salt Fast Reactor

**MSR** Molten Salt Reactor

**MSRE** Molten Salt Reactor Experiment

**ND** Neutron Dynamics

**NEPA** Nuclear Energy for the Propulsion of Aircraft

**NPP** Nuclear Power Plant

**NRC** National Regulatory Commission

**ODE** Ordinary Differential Equation

**ORNL** Oak Ridge National Laboratory

**PARCS** Purdue Advanced Reactor Core Simulator

**PIT** Plutonium Injection Transient

**PPU** Pyro-Processing Unit

**PRHRS** Passive Residual Heat Removal System

**PWR** Pressurized Water Reactor

**PVM** Parallel Virtual Machine

**RAD** Radau-IIA method

**RIAR** Research Institute of Atomic Reactors

**ROS** Rosenbrock method

**SETS** Stability Enhancing Two-Step method

**SINAP** The Shanghai Institute of Applied Physics

**SJC** Single Junction Component

**SMR** Small Modular Reactor

**SNAP** Symbolic Nuclear Analysis Package

**SNF** Spent Nuclear Fuel

**TH** Thermal-hydraulic

**TMSR-SF** Thorium-based Molten Salt Reactor with Solid Fuel

**TMSR-LF** Thorium-based Molten Salt Reactor with Liquid Fuel

**TPS** Two-Pump Shutdown accident

**TRACE** TRAC/RELAP Advanced Computational Engine

**TRISO** Tristructural Isotropic

**TRPZD** Trapezoidal method

**UOX** Uranium Dioxide

**VHTR** Very High Temperature Reactor

# List of Nomenclature

| | |
|---|---|
| $A$ | heat transfer area between the fuel salt and the liquid lead for the DFR core |
| $A^j$ | heat transfer area between the fuel salt and the liquid lead at the $j$th node for the DFR core |
| $A_{1,reg}$ | heat transfer area of a sub-region for the fuel salt for the DFR |
| $A_2$ | flow area of the liquid lead in the reactor core for the DFR |
| $A_{2,reg}$ | heat transfer area of a sub-region for the liquid lead for the DFR |
| $a_{ij}$ | coefficient for the Runge-Kutta method |
| $a_t$ | time factor for the pump shutdown process for the MSRE |
| $b_i$ | coefficient for the Runge-Kutta method |
| $C_i$ | number of precursors for a certain delay neutron group |
| $C_i^j(t)$ | time-dependent number of precursors for a certain delay neutron group at the $j$th node |
| $c_i$ | coefficient for the Runge-Kutta method |
| $c_p$ | heat capacity at constant pressure |
| $c_{p,1}$ | heat capacity at constant pressure for the fuel salt for the DFR |
| $c_{p,2}$ | heat capacity at constant pressure for the liquid lead for the DFR |
| $c_{p,f}$ | heat capacity at constant pressure for the fuel salt for the MSRE |

| | |
|---|---|
| $c_{p,c}$ | heat capacity at constant pressure for the coolant for the MSRE |
| $D_g$ | neutron diffusion coefficient |
| $e$ | specific internal energy |
| $f(t,y)$ | a time-dependent function |
| $H$ | big time step size |
| $H_{core}$ | height of the reactor core |
| $h$ | time step size |
| $J$ | Jacobian Matrix |
| $K$ | friction factor |
| $k_{eff}(\rho,T)$ | density- and temperature-dependent criticality value |
| $k_{eff,analog}$ | criticality value calculated through analog method |
| $k_{eff,collision}$ | criticality value calculated through collision method |
| $k_{eff,implicit}$ | criticality value calculated through implicit method |
| $k_j$ | coefficient for the Runge-Kutta method |
| $L_n^{ID}$ | height or length of a certain component with its ID number |
| $\dot{m}_f$ | fuel salt mass flow rate |
| $\dot{M}_{f,c}$ | fuel salt inventory in the reactor core for the MSRE |
| $\dot{m}_{new}$ | new value of mass flow for the pump transient simulation for the MSRE |
| $\dot{m}_{nominal}$ | nominal mass flow |
| $\dot{m}_{rate1}$ | change rate of the mass flow for the pump initialization for the MSRE |
| $\dot{m}_{rate2}$ | change rate of the mass flow for the pump tansient simulation for the MSRE |
| $N(t)$ | time-dependent neutron population |

| | |
|---|---|
| $N_0$ | initial neutron population |
| $N_n$ | neutron population at a certain time step |
| $N_{n+1}$ | neutron population at the next time step |
| $Nu_1$ | Nusselt number of the fuel salt for the DFR |
| $Nu_2$ | Nusselt number of the liquid lead for the DFR |
| $P$ | reactor power |
| $P_0$ | initial reactor power |
| $P_{nominal}$ | nominal reactor power |
| $P_{peak}$ | peak reactor power |
| $P_{rate}$ | change rate of the reactor power for the power initialization process for the MSRE |
| $P_t$ | time-dependent reactor power |
| $P^j(t)$ | time-dependent reactor power at the $j$th node |
| $\Delta P(t)$ | time-dependent power change |
| $Pr_1$ | Prandtl number of the fuel salt for the DFR |
| $Pr_2$ | Prandtl number of the liquid lead for the DFR |
| $p$ | pressure |
| $Q_{out}$ | thermal output of the reactor for the DFR |
| $R_0$ | initial compensative reactivity |
| $R(\rho, T)$ | density- and temperature-dependent reactivity |
| $R(t)$ | time-dependent global reactivity |
| $R_{capture}$ | capture rate |
| $R_{fission}$ | fission rate |

| | |
|---|---|
| $R_{inelastic}$ | inelastic scattering rate |
| $R_{insert}$ | externally inserted reactivity |
| $R_{leakage}$ | leakage rate |
| $R_{ramp,rate}$ | rate of the ramp reactivity insertion |
| $R_{step}$ | value of the step-wise reactivity insertion |
| $Re_1$ | Reynolds number of the fuel salt for the DFR |
| $Re_2$ | Reynolds number of the liquid lead for the DFR |
| $\mathbf{r}$ | position vector |
| $r_i$ | inner radius of the fuel tube for the DFR |
| $r_o$ | outer radius of the fuel tube for the DFR |
| $S$ | internal heat source |
| $T$ | temperature |
| $T^{i,j-1/2}$ | inlet edge temperature at the $j$th node $i$th region for the DFR core |
| $T^{i,j+1/2}$ | outlet edge temperature at the $j$th node $i$th region for the DFR core |
| $T_1^{i,j}$ | fuel temperature at the $j$th node $i$th region for the DFR core |
| $T_1$ | fuel salt temperature for the DFR core |
| $T_{1,0}$ | fuel salt inlet temperature for the DFR core |
| $T_{1,1}$ | fuel salt outlet temperature for the DFR core |
| $T_2$ | liquid lead temperature for the DFR core |
| $T_{2,0}$ | liquid lead inlet temperature for the DFR core |
| $T_{2,1}$ | liquid lead outlet temperature for the DFR core |
| $T_2^{i,j}$ | liquid lead temperature at the $j$th node $i$th region for the DFR core |
| $T_f$ | fuel salt temperature for the MSRE |

| | |
|---|---|
| $T_f^j(t)$ | time-dependent fuel salt temperature in the $j$th node for the MSRE |
| $T_{f,avg,0}$ | initial average fuel salt temperature for the MSRE |
| $T_{f,in}$ | fuel salt inlet temperature for the MSRE |
| $T_{f,out}$ | fuel salt outlet temperature for the MSRE |
| $T_g$ | graphite temperature for the MSRE |
| $T_g^j(t)$ | time-dependent graphite temperature in the $j$th node for the MSRE |
| $T_{g,avg,0}$ | initial average graphite temperature for the MSRE |
| $T_{melt,f}$ | melting point of the fuel salt for the MSRE |
| $T_{melt,c}$ | melting point of the coolant salt for the MSRE |
| $T_w$ | wall temperature |
| $\Delta T_{log}$ | logarithmic mean temperature difference for the DFR core |
| $t$ | time |
| $t_{end}$ | end of the calculation time |
| $t_{end,pt}$ | time end of the pump transient |
| $t_{end,ramp}$ | time end of the ramp reactivity insertion |
| $t_{init,ps}$ | transient initiating time for the pump shutdown |
| $t_{init,pt}$ | transient initiating time for the pump transient |
| $t_{init,ramp}$ | transient initiating time for the ramp reactivity insertion |
| $t_{init,step}$ | transient initiating time for the step-wise reactivity insertion |
| $U$ | overall heat transfer coefficient |
| $U(u_1, u_2)$ | velocity-dependent overall heat transfer coefficient |
| $U_1$ | overall heat transfer coefficient calculated by energy conservation |
| $U_2$ | overall heat transfer coefficient calculated by engineering formulas |

| | |
|---|---|
| $u$ | velocity |
| $u_1$ | fuel salt velocity for the DFR |
| $u_2$ | liquid lead velocity for the DFR |
| $u_{f,core}$ | fuel salt velocity in the reactor core for the MSRE |
| $u_{f,n}^{ID}$ | fuel salt velocity in a certain component with its ID number for the MSRE |
| $V$ | control volume |
| $V_1^j$ | control volume of the fuel salt at the $j$th node for the DFR core |
| $V_2^j$ | control volume of the liquid lead at the $j$th node for the DFR core |
| $v_g$ | neutron velocity for a certain group |
| $\Delta x$ | length of each node |
| $y'$ | 1st-order derivation of a function |
| $y_n$ | value of the current time step |
| $y_{n+1}$ | value of the next time step |

**Greek Alphabet**

| | |
|---|---|
| $\alpha_1$ | heat transfer coefficient of the fuel salt for the DFR |
| $\alpha_2$ | heat transfer coefficient of the liquid lead for the DFR |
| $\alpha_{T,1}$ | fuel salt temperature coefficient of reactivity feedback for the DFR |
| $\alpha_{T,2}$ | liquid lead temperature coefficient of reactivity feedback for the DFR |
| $\alpha_{T,f}$ | fuel salt temperature coefficient of reactivity feedback for the MSRE |
| $\alpha_w$ | heat transfer coefficient on the wall |

| | |
|---|---|
| $\beta$ | total delay neutron fraction |
| $\beta_i$ | delay neutron fraction for a certain group |
| $\kappa$ | thermal conductivity |
| $\kappa_1$ | thermal conductivity of the fuel salt for the DFR |
| $\kappa_2$ | thermal conductivity of the liquid lead for the DFR |
| $\kappa_f$ | thermal conductivity of the fuel salt for the MSRE |
| $\kappa_c$ | thermal conductivity of the coolant salt for the MSRE |
| $\Lambda_i$ | prompt neutron generation time |
| $\lambda_i$ | decay constant for a certain delay neutron group |
| $\mu$ | dynamic viscosity |
| $\mu_f$ | dynamic viscosity of the fuel salt for the MSRE |
| $\mu_c$ | dynamic viscosity of the coolant salt for the MSRE |
| $\overline{\nu}$ | average number of neutron production per fission |
| $\xi$ | friction factor |
| $\Phi_g$ | neutron flux for a certain group |
| $\rho$ | density |
| $\rho_1$ | fuel salt density for the DFR |
| $\rho_2$ | liquid lead density for the DFR |
| $\rho_f$ | fuel salt density for the MSRE |
| $\rho_c$ | coolant salt density for the MSRE |
| $\Sigma_a$ | macroscopic cross-section of absorption |
| $\Sigma_f$ | macroscopic cross-section of fission |
| $\Sigma_s$ | macroscopic cross-section of scattering |

| | |
|---|---|
| $\sigma_f$ | surface tension of the fuel salt for the MSRE |
| $\sigma_c$ | surface tension of the coolant salt for the MSRE |
| $\tau_c$ | transient time of the fuel salt in the reactor core of the MSRE |
| $\tau_l$ | transient time of the fuel salt in the primary loop outside the reactor core of the MSRE |
| $\chi_g$ | spectrum of neutrons produced by fission |
| $\chi_{g,i}$ | spectrum of neutrons produced by precursors decay |

**Other Symbols**

| | |
|---|---|
| $\partial$ | partial differentiation |
| $\nabla$ | divergence in cartesian coordinate |

# Chapter 1

# Introduction of Molten Salt Reactor

## 1.1 Basic Concept of Molten Salt Reactor

Other than any other types of reactor using solid nuclear fuel no matter in the form of rods or pebbles, the molten salt reactor (MSR) usually uses liquid fuel for its primary loop and simultaneously the fuel itself works also as the primary coolant. In particular, instead of the traditional UOX or MOX fuel (e.g. $UO_x$, $PuO_x$ or $ThO_x$), the fuel used in MSR is usually in the form of the fluoride or chloride ($UCl_x$, $PuCl_x$ or $ThCl_x$), which is dissolved in a mixture of other fluorides or chlorides of the alkali metals, for instance, the Lithium (LiF) or Beryllium fluoride ($BeF_2$). The reasons of selecting such carrier salts are due to its good thermal stability, small density and relative low melting point. For the working fluid in the secondary loop, the MSR system usually has options, for instance, it can choose just the carrier salt without fuel composition, another kind of salt or liquid metals, which can be lead or sodium.

The working principle of a MSR can be explained briefly with Figure 1.1. The fuel salt flows into the reactor core, where the nuclear chain reactions take place thus the fuel salt will be heated up internally. Then the fuel salt releases its energy to the coolant salt at the intermediate heat exchanger and finally the coolant salt heats up the water, which is going to drive the turbines.

Similar to some other GEN-IV reactor types, the MSR has, for example, the possibility of waste-minimizing, fuel-breeding operation, non-proliferation, high fuel utility and higher thermal efficiency, but due to the application of the liquid fuel the MSR has some huge advantages than the other candidate reactors:

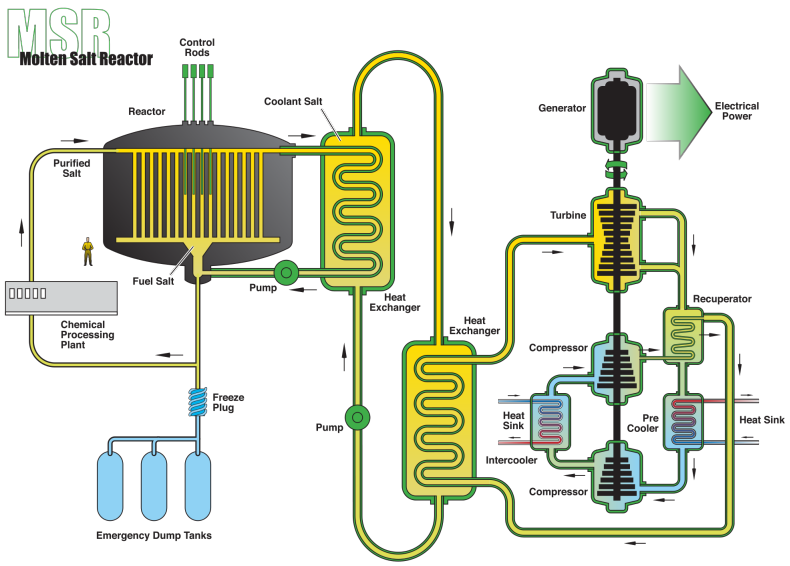


**Figure 1.1**: General system layout of molten salt reactor [1]

1. **No core molting accident:** As known, the core melting accident is nearly the most severe accident for the nuclear power plants, because this accident always brings about a large leakage of high level radioactive materials and an irreversibly lethal damage to the reactor vessel. All the three most catastrophic accidents in the history, namely in Chernobyl, Three-Miles Island and Fukushima, are accompanied by the core melting accidents. However, for the MSR this kind of extreme accident is completely eliminated, which is the unique advantage of the MSR and makes MSR inherently safe.

2. **Online refueling:** The current large commercial PWRs or BWRs need to be shut down to be refueled, while for MSR the fresh fuel can be injected online at the reprocessing unit without the necessity of reactor shutdown. Simultaneously, online refueling means the possibility of online removal of the fission products and the extraction of the fertile materials for the fuel breeding.

3. **No fabrication and handle for solid fuel:** Since MSR is using liquid fuel, there is no demand for the fabrication and handling of the fuel assembly, which takes a large part of operating cost of the nuclear power plants at the moment.

4. **Low operating pressure:** The MSR can be operated with much lower pressure (normally several bars) compared to a PWR and a BWR, because the saturation temperature of most molten salt mixtures applied in MSR can be

up to around 1700K or even higher under the atmospheric pressure. Regarding their melting points (usually around 700K to 900K) the salts can maintain one-phase (liquid) in a large range of about 1000K, which means all the equipments of the primary or secondary loop can be designed only for a liquid working fluid thus enormously lowering the cost of the equipment manufacturing. Additionally, low operating pressure means limited explosion damage and less amount of radioactive leakage in case of the breaks in the primary loop.

Of course, as the other GEN-IV reactors the MSR is also facing some challenges at present:

1. **Radioactive shielding:** The fuel salt flows through the entire primary loop, which definitely brings stress on the radioactive shielding. Traditionally no matter for the PWRs, BWRs or other GEN-IV reactors, the fuel is fixed in the reactor core during operation all the time and the reactor vessel is a critical barrier against radioactive leakage. However, for the MSR this shielding doesn't work well any more, because some precursors with long half-life will be brought out of the reactor core by the carrier salt and their decays can occur everywhere in the primary loop. Furthermore, the online maintenance become more difficult and the radioactive damages to the instruments in containment should be paid more attention to.

2. **Material limitation:** This can be a universal challenge for all the GEN-IV reactors, because they are developed to be operated with a significantly higher temperature than the current GEN-II or GEN-III reactors. Although the MSR can be operated with only several bars, the operating temperature of a MSR can be up to 1000K or even higher, which implies that the risk of the material deformation and even failure of the structures still remains.

3. **Corrosion to the structures:** In order to avoid corrosion issue, the molten salts must be highly purified and usually be operated under the protection of the dry inert gas, for instance, helium. This is because the hydrogen in water will combine with flour to be the hydrogen fluoride, which is extremely chemically aggressive to the structural materials.

4. **Lack of research tools and data:** That the working fluid itself is the fuel means the behavior of the neutron dynamics and the thermal-hydraulics are

strongly coupled. That's why the researches in recent years focus on the multi-physical simulations for the MSR. However, so far it is hard to find a specific and widely recognized code for this reactor type and moreover, the molten salts are not easily available for the experimental work, which leads to a fact that till now the database of the molten salts cannot yet support the R&D about MSR well.

## 1.2 Historical Evolution of Molten Salt Reactor

### 1.2.1 MSR Projects in the United States

The United States ever took the leading position of the MSR researches and the world's first MSR concept was proposed by the project Nuclear Energy for the Propulsion of Aircraft (NEPA) initiated in 1947 by the United States Army Air Forces, whose purpose was to build nuclear-powered bomber. The program was transfered to Aircraft Nuclear Propulsion (ANP) after 4 years and was canceled in 1961. During these years the world's first molten salt reactor called Aircraft Reactor Experiment (ARE) was built and operated for a 1000-hour cycle at the Idaho National Laboratory (INL) in 1954. The ARE was a BeO-moderated thermal nuclear reactor with 2.5 MW output using NaF-$ZrF_4$-$UF_4$ and sodium as the fuel and secondary coolant respectively. In 1956 another experimental reactor called Heat Transfer Reactor Experiment-1 (HTRE-1) and its improved version HTRE-3 (Figure 1.2) were developed and successfully drove the J47s engine by General Electric (GE) using direct air cycle. Additionally, in 1957 the Oak Ridge National Laboratory (ORNL) made another reactor (PWAR-1) critical in the framework of the project Circulating-fuel Reactor Program supported by the Pratt and Whiteney Aircraft Company. This experiment reactor fueled and cooled with NaF-$ZrF_4$-$UF_4$ was run shortly at zero power and able to maintained the design operating temperature approximately at 950K. [2] [3] [6]

In 1962 the construction of the Molten Salt Reactor Experiment (MSRE) began and it went critical in 1965 and was run until 1969 with equivalent 9000 full-power hours totally. The MSRE was a graphite-moderated thermal reactor with 10MW output and it used the salt mixtures $^7$LiF-$BeF_2$-$ZrF_4$-$UF_4$ (65.0-29.1-5.0-0.9 mole%) as the fuel and $^7$LiF-$BeF_2$ (66-34 mole%) as the secondary coolant. The enrichment of the

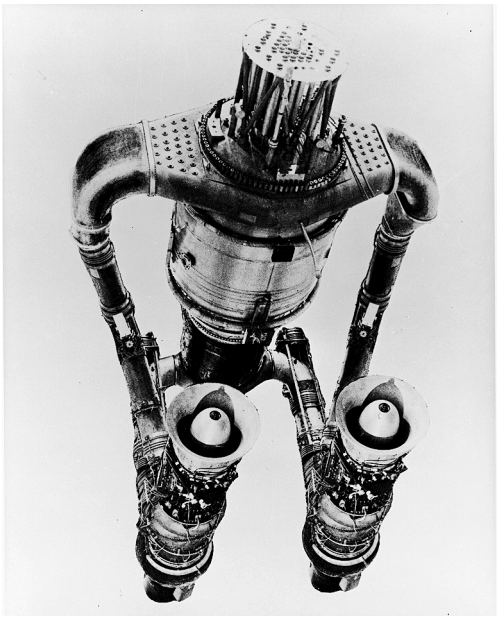

**Figure 1.2**: The heat transfer reactor experiment-3 (HTRE-3)[6]

$^{235}$U reached up to 33%. After the first normal shutdown $^{233}$U was added to the carrier salt making MSRE the world's first reactor fueled with this fissile material. [4] [5]

The Haselloy-N was chosen as the structural material and the helium worked as the cover gas offering the protection for the structures from corrosion. The entire size of the reactor vessel of the MSRE was about 1.5m in diameter and 2.4m in height and the graphite-made channels were installed on the moderator support grid (Figure 1.3). The average operating temperature of the fuel salt was about 920K, while for the coolant salt it was around 840K. The air-cooled radiator in the secondary loop was developed to remove the heat generated in the reactor core (Figure 1.4).

Actually the MSRE was the inheritor of the technology from the military project NEPA or ANP, but its great potential of civilian use was found by the people at that moment. During the project the MSRE had been technically proven that this reactor type was dynamically stable, reliable and inherently safe; the online salt handling was quite practical and no corrosion problem came up as worried before.

Additionally, the research team of the ORNL had developed another MSR concept in a commercial scale with a 3 GWth output, namely the MSBR (Molten Salt

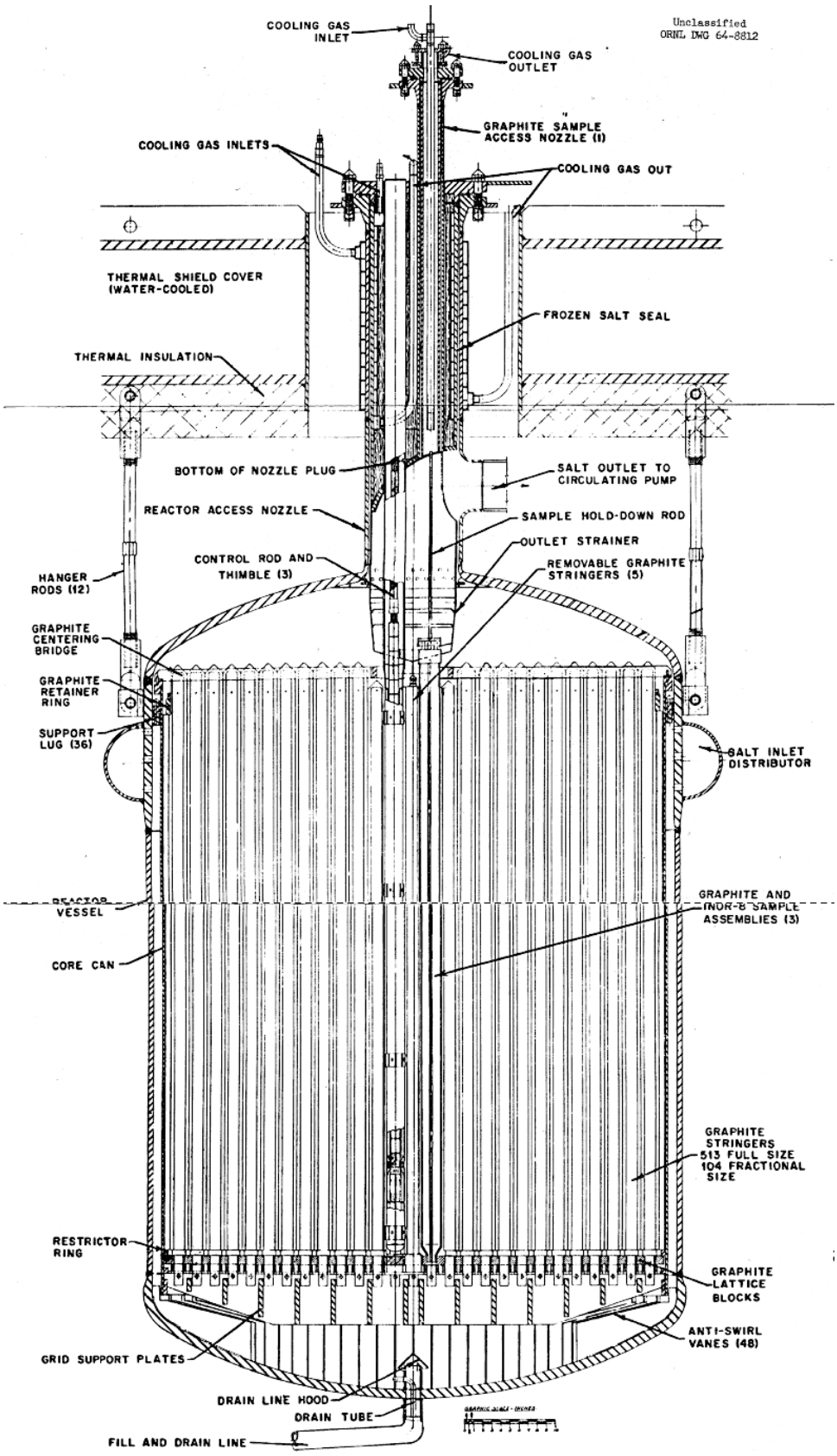


**Figure 1.3**: The reactor vessel of MSRE [24]

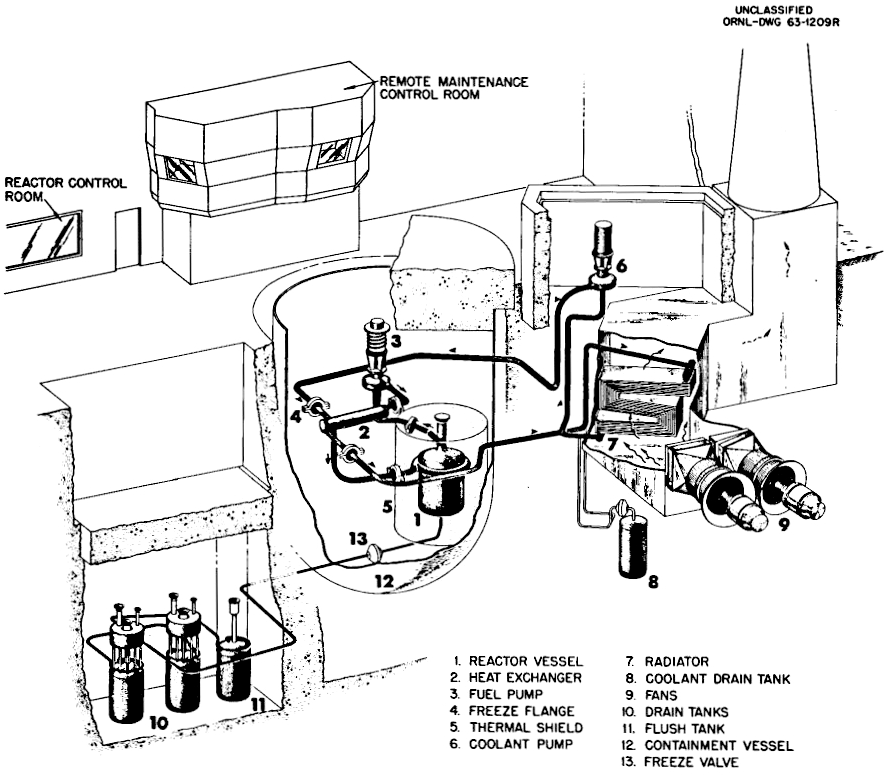


**Figure 1.4**: The system layout of MSRE [29]

Breeder Reactor) with $^{232}$Th-$^{233}$U fuel cycle having a much better breeding behavior than the MSRE. However, due to the end of funding and strong competition from other candidate reactors, MSRE project was terminated in 1970s. Generally, the achievement of the MSRE has not only shown the public the possibility of building a liquid-fueled nuclear reactor but also provided the researches in the future with the reliable experiences and the critical benchmark.

### 1.2.2 MSR Projects in Other Countries

Not just in the United States, Russia attempted to build its own molten salt reactor late in 1970s. This program was taken charge of by the Kurchatov Institute. Unfortunately, the Russian was not able to put its MSR project into practical implementation due to the Chernobyl accident, although large amount of theoretical and experimental work had been accomplished before.

A little bit later than the MSRE program, the Britain's Atomic Energy Research

Establishment (AERE) launched its own MSR project. They focused on the Molten Salt Fast Reactor (MSFR), which was supposed to be a plutonium burner based on the amount of its stockpiles in U. K.. The MSFR was design to have 2.5 GW electric output and to be fueled with plutonium chloride cooled by lead or alternatively by helium. The theoretical and experimental tasks were finished in 1973, but one year later another competitor, namely the Prototype Fast Reactor at Dounreay, went critical and took the preemptive opportunity to become the priority of the work, which partly induced the end of the MSFR project.

## 1.3 Recent Development of Molten Salt Reactor

Since a decade ago the MSR has been drawing a lot of attention all around the world. Nowadays most research teams or governments are interested in three highlights of this reactor type: **fuel breeding**, **high operating temperature** and **waste burner**, which are correspondent to the three hot topics of the energy issue: sustainable development, rapid increasing power demand and nuclear waste treatment.

### 1.3.1 United States: FHR

In 2002 the staff members from ORNL, the University of California at Berkley and Sandia National Laboratories re-thought about the possibility to restart the research of the molten salt reactor. For this time they opted to the salt-cooled rather than the salt-fueled reactor type. Particularly, the conceptual design of the FHR (Fluoride salt-cooled High temperature Reactor) is to use coated particle fuel cooled by the Flibe (LiF-$BeF_2$) (Figure 1.5). Since 2004 they have been getting support from the DOE (Department of Energy) Office of Nuclear Energy but on a small scale. During 2004 to 2011 some theoretical and experimental works were finished. Afterwards ORNL and SINAP (The Shanghai Institute of Applied Physics) got contact and initialized collaboration and finally obtained the governmental support, as the DOE and Chinese Academy of Sciences (CAS) signed the relevant memorandum of understanding in 2011. [7] [8]

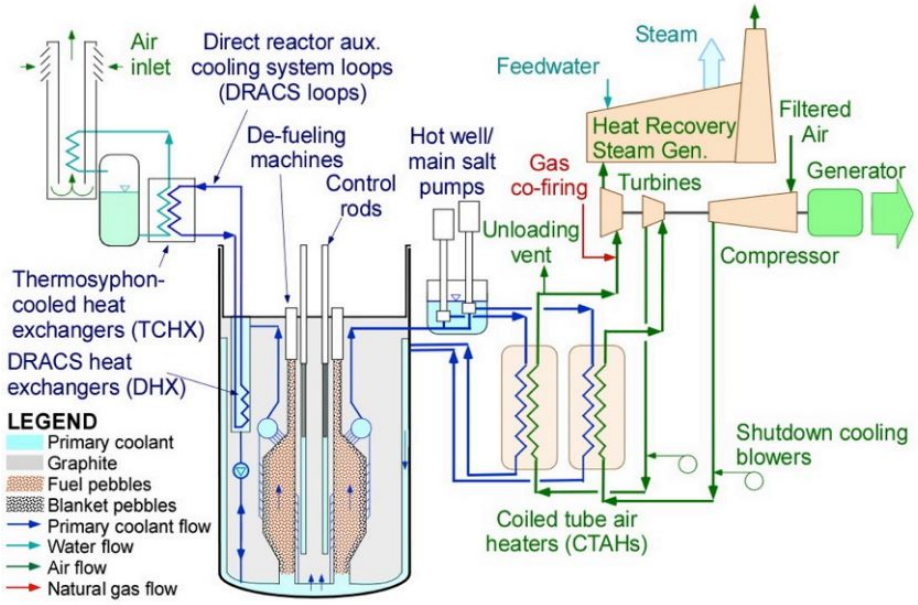


**Figure 1.5**: System layout of FHR concept [8]

Furthermore, in the United States there are still some startup private companies intending to join MSR market such as *Flibe Energy* who is pursuing to build a 10 MW to 50 MW or up to 250 MW small LFTR (Liquid Fluoride Thorium Reactor) for remote locations [9] and besides, the *Transatomic Power* is working on a thermal MSR capable to load the fuel much easier available such as fresh uranium or spent nuclear fuel. [10]

### 1.3.2 China: TMSR-SF/TMSR-LF

The development of the MSR in China seems to get a solid support from the government since they started to cooperate with the United States. The Shanghai Institute of Applied Physics (SINAP), branch of the Chinese Academy of Sciences (CAS), is now the leading research team attempting to commercialize the MSR in China. The whole program was divided into two parallel sub-projects: one is TMSR-SF (Thorium-based Molten Salt Reactor with Solid Fuel) and TMSR-LF (Thorium-based Molten Salt Reactor with Liquid Fuel). The TMSR-SF concept is considered to be a molten salt-cooled Very High Temperature Reactor (VHTR) using the TRISO (Tristructural Isotropic) fuel from the pebble bed High Temperature Gas-cooled Reactor (HTGR), while the TMSR-LF is the real liquid-fueled reactor

using fluoride salt mixture (Figure 1.6). The road map of the program was clearly scheduled, that the test and experimental reactors will be built before 2020 and after 2040 both reactors will be finally commercialized. The current status shows that the program is getting progresses steadily, for instance, the test facilities of the circulation loop with nitrate salt has been built and the technical problems of the circulating pump, heat exchanger and frozen valves were basically solved. Moreover, the technologies of the fluoride volatility, distillation and electrochemical separation connected with the online reprocessing have also obtained some remarkable achievements. [11] [12]

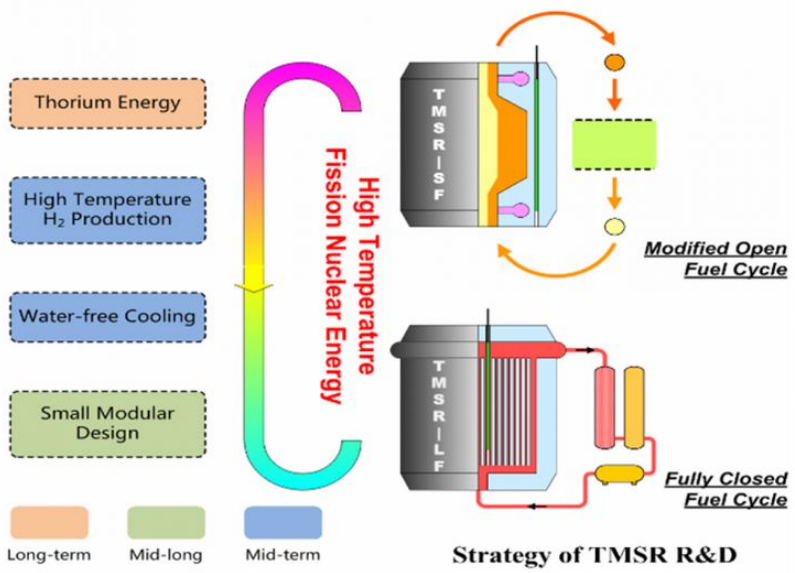


**Figure 1.6**: The TMSR-SF and TMSR-LF concept from SINAP [12]

### 1.3.3 Russia: MOSART

The MOSART (Molten Salt Actinide Recycler and Transmuter) is actually a part of the MARS (Minor Actinide Recycling in Molten Salt) project, in which the RIAR (Research Institute of Atomic Reactors), Kurchatov Institute and other institutions are involved. As its name, the MOSART focuses on the waste conversion rather than the fuel breeding. It is developed to use Flibe (LiF-$BeF_2$) as the carrier salt and transuranic fluorides from the LWR's SNF (spent nuclear fuel) as the dissolved fuel composition. According to its configuration, the MOSART has a cylindrical homogeneous core with a height of 3.6m and a diameter of 3.4m wrapped by a 0.2m

thick graphite layer as the reflector peripherally. The design fuel temperature in primary loop lies in a range from 600°C to 720°C and it gives a 2400 MW thermal output. Recently another fuel option for the MOSART was proposed, which means that the $^{232}$Th-$^{233}$U fuel cycle can be introduced into this system too. [13] [14]

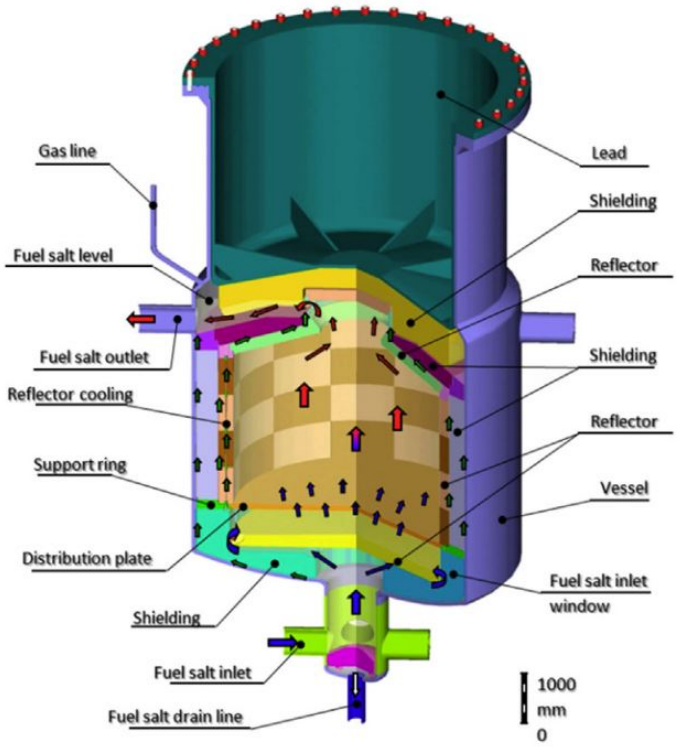


**Figure 1.7**: The conceptual design of MOSART [13]

### 1.3.4 Europe: EVOL

the EVOL, abbreviation of Evaluation and Viability of Liquid fuel fast reactor system, is a tight-linked project to the MOSART. In the framework of the EVOL a concept of a MSFR (Molten Salt Fast Reactor) was presented. This MSFR is regarded as an integrated and compatible MSR, which means the reactor core, the main pump and the heat exchanger are located in a single reactor vessel (Figure 1.8). The MSFR contains totally 18m$^3$ fuel salt based on lithium fluoride in the core and outputs 3000 MWth with 750°C operating temperature. Theoretical and experimental studies have been done and the feasibility of this MSFR design was basically verified. [13].

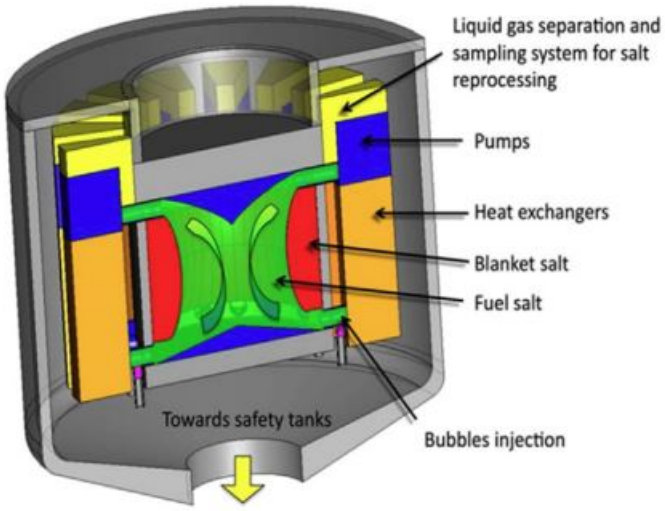


**Figure 1.8**: The conceptual design of MSFR from EVOL project [13]

### 1.3.5 Canada: IMSR

The *Terrestrial Energy Inc.* (TEI), located in Canada is developing an Integrated Molten Salt Reactor (IMSR) (Figure 1.9) which belongs to the category of the DMSR (Denatured Molten Salt Reactor). It seems that Canadian are not interested in fuel breeding and it might be a spontaneous choice of them, as they are experienced in low-enriched uranium for years and have a complete supply chain and less obstacle to license this fuel. The first-of-a-kind IMSR can have a output from 30 MWe up to 300 MWe and as a SMR (Small Modular Reactor) it is easily replaceable by a new modular after 7-year operation and the process of the long-term storage for the discharged reactor is similar to the existing industry protocols for the long-term nuclear waste containment. Furthermore, the IMSR can be arrayed in a multi-unit facility for the demand of larger power generation. Miniaturization and modularity also guarantee the possibility of batch production like "batteries", lower-cost shipment and shorter construction time. Similar to other MSR, the IMSR has only one-third of fission product waste and far more less plutonium as the current commercial NPPs due to high fuel utility and when extra connected to a reprocessing unit the near waste-free operation wouldn't be a dream any more. [15]

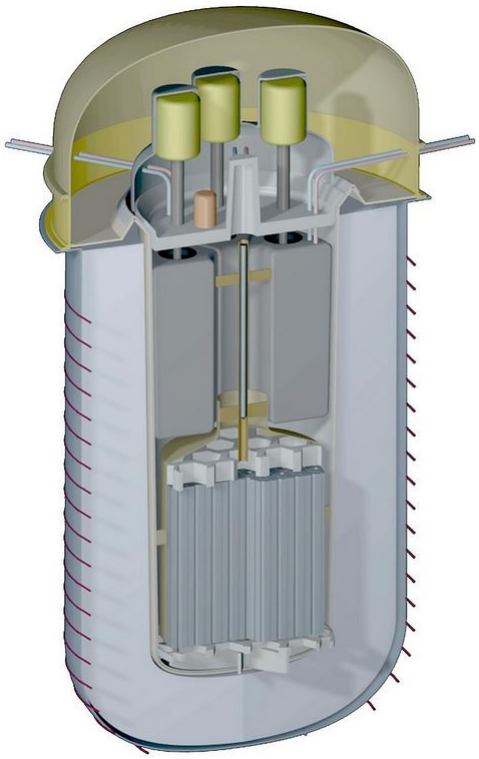

**Figure 1.9**: The conceptual design of IMSR from TEI [15]

### 1.3.6 Japan: FUJI MSR

A Japan-based company, International Thorium Energy & Molten Salt Technology Inc., is taking charge of the R&D for the FUJI MSR. The previous plan is to build a 10 MWe reactor called MiniFUJI to be applied for the power demand of computer server parks in the IT Industry or for the charging station of the electric cars. The current research foresees a 200 MWe FUJI MSR for the typical electric power grids. The FUJI MSR has a similar design to the MSRE developed by ORNL in 1960s. It is a graphite-moderated thorium-based thermal reactor in purpose of near-breeding operation (Figure 1.10). Till now this reactor is still in the stage of conceptual design and it seems they are suffering from funding issue. [17] [18]

### 1.3.7 Germany: DFR

Although Germany is going to phase out the nuclear industry, a startup company called IFK (Institut für Festkörper-Kernphysik) standing in Berlin, is still looking forward to having their own MSR called Dual Fluid Reactor (DFR). The DFR is

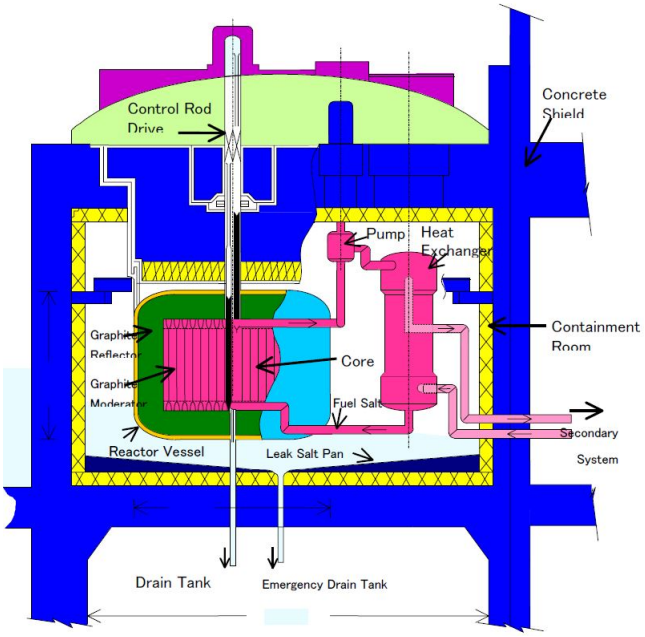


**Figure 1.10**: containment layout of FUJI MSR [16]

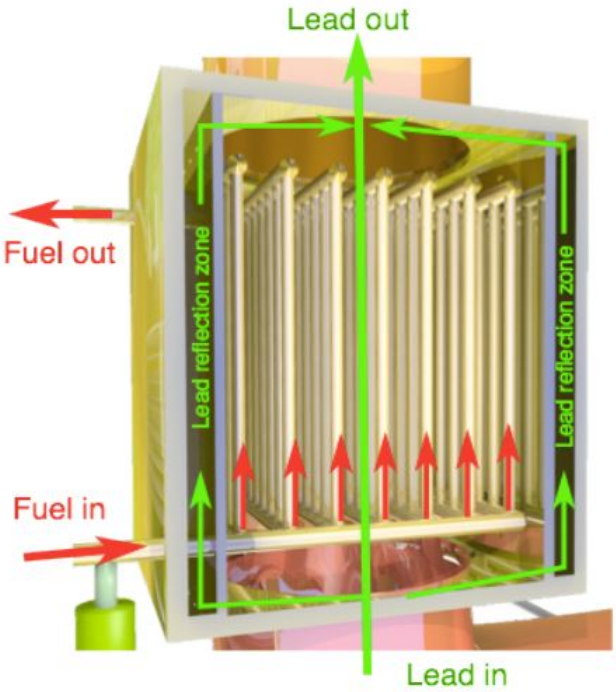


**Figure 1.11**: Core design of the DFR by IFK [53]

a high-temperature lead-cooled fast molten salt reactor. The reactor vessel of the DFR is in fact a heat exchanger, where the nuclear reactions occur and heat up the fuel salt based on uranium and plutonium chlorides, who immediately transfer their

heat to the liquid lead flowing in. The DFR gives a 3 GWth output and the outlet temperature of liquid lead can reach above 1000°C, thus high efficiency ($\geq$50%) is promised. Now this project is getting connections with relevant universities both at home and abroad and the theoretical calculation is being done at present. [53]

# Chapter 2

# Methodology of Adapting TRACE for MSRE Simulation

## 2.1 Basic R&D Approach

Other than the solid fuel reactor, the neutron physics and thermal-hydraulics of the MSR is more directly and probably more strongly coupled. First, as a internal heat source the power fluctuation may directly change the temperature of the fuel salt inducing the change of the cross-section and the neutron energy due to the density and Doppler effect, which in turn changes the power production. Second, the fact that the fuel is moving through the reactor core means that the neutron flux is intensively dependent on the fuel distribution across the reactor core, which is also connected to the reactor core structures. Moreover, the moving nuclear fuel may carry part of the precursors out from the core resulting in the precursor loss and consequently the decays of some precursors take place in the fuel circuit outside the reactor core, if the fuel salt velocity is fast enough. This means that the power production and distribution can also be fuel velocity-dependent. Third, the fuel salt velocity is a critical factor which impacts the heat transfer between the fuel salt and the structures or the internal heat transfer through convection. Finally, the temperature-dependent physical properties like the density, heat capacity and the viscosity can also be influential to the temperature behavior of the reactor. In a word, considering the "dual role" of the fuel salt the study on the molten salt reactor eventually becomes a multi-physical problem.

$$
\begin{cases}
\text{Fluid Dynamics:} \\
\begin{cases}
\dfrac{\partial \rho}{\partial t} + \nabla \cdot (\rho \mathbf{u}) = 0 \\
\rho \dfrac{\partial u}{\partial t} = -\nabla p + \mu \nabla^2 u + \rho \mathbf{g} \\
\dfrac{\partial \rho c_p T}{\partial t} + \nabla \cdot (\rho c_p T u) = \nabla \cdot \kappa \nabla T + U(T' - T) + S
\end{cases} \\
\text{Neutron Dynamics:} \\
\begin{cases}
\dfrac{1}{v_g}\dfrac{\partial}{\partial t}\Phi_g(\mathbf{r},t) = \nabla \cdot D_g(\mathbf{r}) \nabla \Phi_g(\mathbf{r},t) - \Sigma_{a_g}\Phi_g(\mathbf{r},t) - \displaystyle\sum_{g'>g}^{G} \Sigma_{s_{g,g'}}\Phi_g(\mathbf{r},t) \\
\qquad\qquad + \displaystyle\sum_{g'=1}^{G} (\chi_g \overline{\nu}\Sigma_{f_{g'}}(1-\beta) + \Sigma_{s_{g',g}})\Phi_{g'}(\mathbf{r},t) \\
\qquad\qquad + \displaystyle\sum_{i=1}^{I} \chi_{g,i}\lambda_i C_i(\mathbf{r},t), \\
\qquad\qquad\qquad\qquad g = 1,2,...,G \\
\dfrac{\partial}{\partial t} C_i(\mathbf{r},t) = -\nabla \cdot (\mathbf{u} C_i) + \beta_i \displaystyle\sum_{g=1}^{G} \nu \Sigma_{f_g}\Phi_g(\mathbf{r},t) - \lambda_i C_i(\mathbf{r},t) \\
\text{or point-kinetic model} \\
\dfrac{dN(t)}{dt} = \dfrac{R(t)-\beta}{\Lambda} N(t) + \displaystyle\sum_{n=1}^{I} \lambda_i C_i(t) \\
\dfrac{dC_i(t)}{dt} = -\lambda_i C_i + \dfrac{\beta_i}{\Lambda} N(t) - \dfrac{C_i(t)}{\tau_c} \\
\qquad\qquad\qquad\qquad i = 1,2,...,I
\end{cases}
\end{cases}
\tag{2.1}
$$

Fundamentally, the universal multi-physical model (considering the precursor loss) for the molten salt reactor is a set of the time-dependent three-dimensional differential equations composed of the neutron dynamic model and the thermal-hydraulic model. The thermal-hydraulic model contains the mass, the momentum (for a incompressible newton fluid) and the energy conservation based on the theorems of the fluid mechanics and thermodynamics. The neutron dynamic model consists of the neutron diffusion equations or the point-kinetic equations for neutron population

**Table 2.1**: Overview of some research approaches presented in recent years

| Author (year) | Reactor Type | ND Code | TH Code | Model | Analysis Type |
|---|---|---|---|---|---|
| A. Cammi (2011) | MSBR | NEWT, 2D | COMSOL, 3D | Flow Channel | Transient |
| C. Guerrieri (2013) | MSBR | 1D | 1D | RC and HX | Transient |
| E. Linden (2012) | MSFR | DALTON, 3D | HEAT, 3D | RC | Transient |
| Z. Guo (2013) | MSRE | MCNP4c, 3D | MAC, 3D | RC | Steady-State |
| C. Nicolino (2008) | MOSART | 2D | 2D | RC | Transient |

and the precursor concentrations (Eq. (2.1)). The data shared between thermal-hydraulic model and neutron dynamic model is the heat source ($S$) in the energy conservation determined by the neutron flux ($\Phi_g$) or neutron population ($N(t)$) as well as the temperature ($T$) in the energy conservation directly impacting the values of the macroscopic cross-section ($\Sigma_a, \Sigma_s, \Sigma_f$) in the diffusion equations or the reactivity feedback ($R(t)$) in the point-kinetic equations. Once the model is built, the next step is to decide in which way or particularly by which code these equations are going to be solved.

Table 2.1 gives an overview of the methodologies presented in some research papers of recent years. It shows clearly that those teams selected different modified or even in-house made tools for their coupled simulations, which in turn implies that there is no specific and authoritative code currently available for the MSR's simulation. Additionally, writing a coupling code for two independent codes requires massive efforts to modify the bottom of the code or even if the MPI (Message Passing Interface) or PVM (Parallel Virtual Machine) is applied, still amount of the code modifications needs to be done. However, in this work a new modeling method was introduced. One highlight of this method is that it uses all built-in functions and components to implement the coupled-physical simulations within a single code which means the complex code modification is not imperative and the coupling between the neutron physics and the thermal-hydraulics is inherently synchronized in each time step.

## 2.2 Methodology of Current Work

### 2.2.1 Introduction of TRACE

The system code TRACE was selected as the default analysis tool for the current work and the MSRE serves as the benchmark.

The TRAC/RELAP Advanced Computational Engine (TRACE) is a modernized thermal-hydraulic code developed by NRC (National Regulatory Commission of the United States). TRACE is an enhanced and consolidated version of the NRS's three legacy safety codes: TRAC-P, TRAC-B and RELAP, so it is capable to analyze the large or small loss of coolant accident (LOCA) or other system transients such as pump coast-down. Basically TRACE is a one-dimensional code, but for some certain components such as the reactor vessel, the capability of simulating the three-dimension thermal-hydraulic phenomena has been extended. In addition, TRACE is convenient to couple the built-in point-kinetic model or the diffusion code - PARCS (Purdue Advanced Reactor Core Simulator) externally to produce more comprehensive results for the evaluation of the reactor system. Now TRACE is the flagship thermal-hydraulic analysis tool of NRC. [20]

Moreover, the SNAP (Symbolic Nuclear Analysis Package) is a graphical user interface offering the modeler a visualized and comprehensive view of their system model and assisting in writing the input file correctly. For the post-processing the SNAP provides with a plug-in called AptPlot, with which the results can be easily plotted. [20]

The computational engine for the thermal-hydraulics of TRACE was programmed based on the Stability Enhancing Two-Step (SETS) method in default mode. This method has the advantage of avoiding Courant stability limits on time-step size but has the disadvantages of relative high numerical diffusion. Another method available in TRACE is the semi-implicit method having substantially less numerical diffusion, but the time-step size is restricted by the Courant material limit [21]. The basic form of one-dimensional field equations to be solved in TRACE are shown in Eq. (2.2)

$$\begin{cases} \dfrac{\partial \rho}{\partial t} + \dfrac{\partial}{\partial x}(\rho u) = 0 \\ \dfrac{\partial u}{\partial t} + u\dfrac{\partial u}{\partial x} = -\dfrac{1}{\rho}\dfrac{\partial p}{\partial x} - Ku|u| \\ \dfrac{(\rho e)}{\partial t} + \dfrac{\partial}{\partial x}(\rho e u) = -p\dfrac{\partial u}{\partial x} + \dfrac{\alpha_w}{V}(T_w - T) + S \end{cases} \tag{2.2}$$

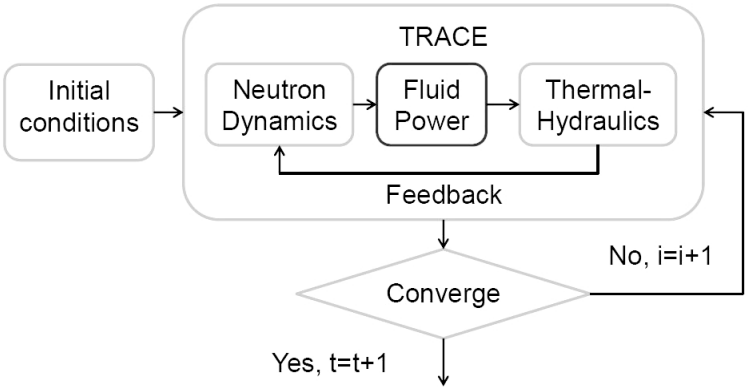


**Figure 2.1**: Coupling approach

### 2.2.2 TRACE Adaptation for MSRE

To adapt TRACE for the MSR's simulations, two main tasks must be achieved: first, coupling thermal-hydraulics and neutron physics and second, adding new working fluids. The reason to select TRACE for the current study is that for one thing the source code of TRACE is available for all the CAMP (Code Application and Maintenance Program) member countries, so it is possible to embed new working fluids, namely the molten salts into the source code of TRACE; more importantly, TRACE integrates a crucial function called "*Fluid Power*", which is used to simulate the energy directly deposited to the fluid. Hence, the "*Fluid Power*" eventually serves as the internal heat source of the working fluid, which is exactly the way how the liquid-fueled reactor produces the power. Furthermore, this "*Fluid Power*" can be configured to be dependent on an input variable thus it gives the possibility to couple the neutron dynamics and thermal-hydraulics together. The approach of coupling is illustrated in Figure 2.1.

The point-kinetic model was considered to be sufficient for a preliminary study, because the simulations focus mainly on the dynamic behavior of the entire MSRE system. Unfortunately the built-in point-kinetics model of TRACE is only able to be configured within the "*Power Component*" developed to power the solid fuel at the moment. What's more, for the situation of the MSRE, the precursor drift needs to be taken into account principally, which causes massive modification work to the governing point-kinetic equations at the bottom of the code. Thus we have to build a new numerical solver which can read the system reactivity in and output

the point-kinetic power. The modified point-kinetic equations were set up as follows (Eq. (2.3)). Other than the classical form of point-kinetic equations, the modified version includes the items calculating the rate of the precursors loss $\frac{C_i(t)}{\tau_c}$ and the rate of the re-entering $\frac{C_i(t-\tau_l)}{\tau_c}e^{-\lambda_i\tau_l}$ depending on the circulating time of the fuel salt in the reactor core ($\tau_c$) and in the primary loop outside the reactor core ($\tau_l$). This makes the former equations the delay differential equations (DDEs).

$$\begin{cases} \dfrac{dN(t)}{dt} = \dfrac{R(t)-\beta}{\Lambda}N(t) + \sum\limits_{n=1}^{6}\lambda_i C_i(t) \\ \dfrac{dC_i(t)}{dt} = -\lambda_i C_i + \dfrac{\beta_i}{\Lambda}N(t) - \dfrac{C_i(t)}{\tau_c} + \dfrac{C_i(t-\tau_l)}{\tau_c}e^{-\lambda_i\tau_l} \end{cases} \tag{2.3}$$

### Selection of the Numerical Solver

To solve these ordinary differential equations numerically, three numerical solvers are supposed to be sufficient for a preliminary study: the forward Euler method (FEU), backward Euler method (BEU) and the trapezoidal rule (TRPZD).

The forward Euler method is a first-order explicit method and its local truncation error is proportional to the square of the time step size ($h^2$). Assuming a basic form of the ODEs to be like Eq. (2.4), the forward Euler method determines the value of next step by adding the multiplier of the current value and the step size (Eq. (2.5)). The Euler method is a one-step lower-cost numerical solution suitable for non-stiff equations.

$$y' = f(t, y) \tag{2.4}$$

$$y_{n+1} = y_n + hf(t, y) \tag{2.5}$$

The backward Euler method is defined in Eq. (2.6). Evidently it is an implicit method requiring another step to solve the equations. The backward Euler method gives the same accuracy as the forward Euler method, but it is applicable for stiff equations.

$$y_{n+1} = y_n + hf(t + h, y_{n+1}) \tag{2.6}$$

The third one is the trapezoidal rule, which can be considered as the consolidation

of the two methods above. The trapezoidal rule enhances the accuracy one order better to the cubic of the time-step size ($h^3$) and offers a more confident stability for the stiff equations, but as an implicit method it has a heavier computational load than the explicit method.

$$y_{n+1} = y_n + \frac{h}{2}(f(t, y_n) + f(t + h, y_{n+1})) \tag{2.7}$$

Then the task is to select a proper numerical solver for the point-kinetic equations. Before building the complex TRACE loop model and its control system, it is essential to investigate the precision and the stability of the three methods above. Hence, a simple exponential differential equation was defined in Eq. (2.8) and it is reasonable to evaluate this function firstly, because on one hand, with its fast change rate this equation can be stiff, which can roughly represent and simulate the large transient during the reactor operation and on the other hand, the analytical solution of this equation is easily derivable. Thus the comparison between the numerical and exact solution is possible.

$$y' = e^t \tag{2.8}$$

A MATLAB® code was developed to evaluate the accuracy and the time efficiency of the three numerical solvers for variant time step sizes. The code was run on a 64-bit Windows® 8.1 laptop machine equipped by the Intel® Core™ i5-4200U 1.6GHz and having 8GB RAM. Figure 2.2 illustrates the comparison between the three numerical solvers and the exact values. Table 2.2 gives the error evaluation at the selected time point, while Table 2.3 offers an overview of the time efficiency of the solvers. It is clear that no matter in large or small time-step sizes, the TRPZD method produces more accurate results than the others, however, the time required by the FEU method is much less than the implicit BEU and TRPZD methods and with a small time-step size the FEU can also produce a good precision.

To test the suitability of the numerical solvers further and to obtain a more practical reference case, a simplified coupled-physical MSR model was built, which contains the classical form of the point-kinetic equations considering the first two groups with temperature feedback coupled with the energy conservation of the fuel salt (Eq. (2.9)). During the simulation a step insertion of reactivity with 600pcm was added, because this scenario is considered to be the most severe reactivity initial-

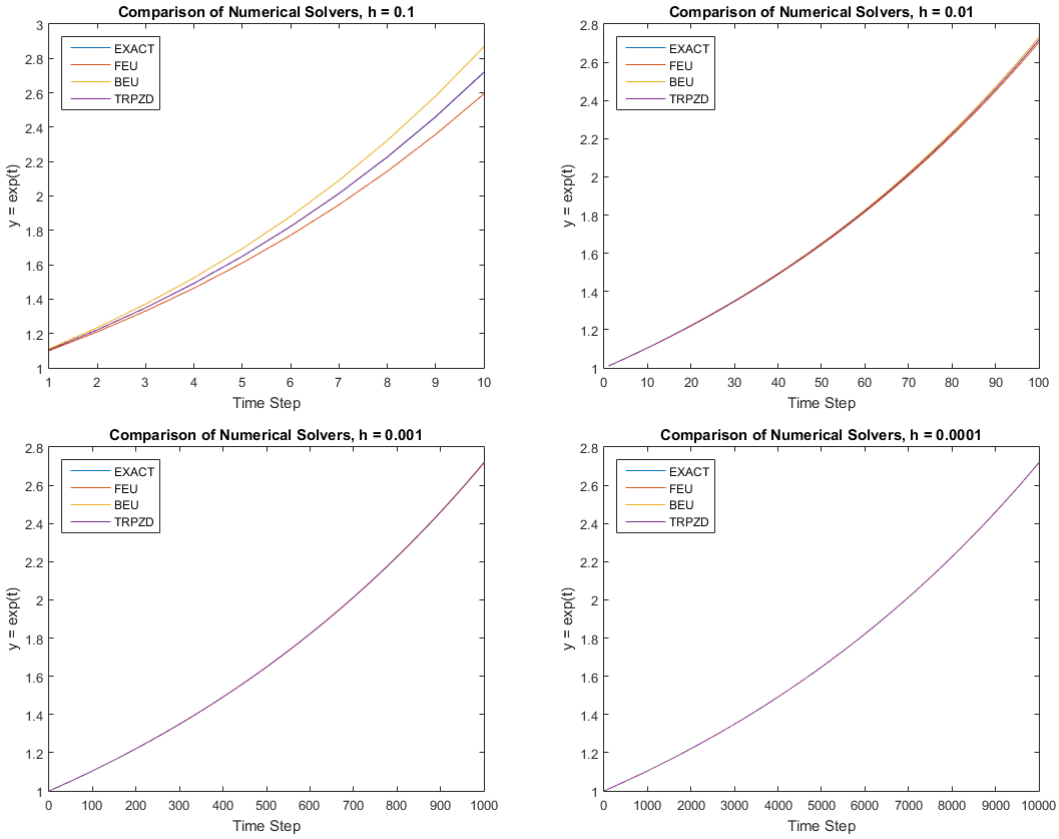


**Figure 2.2**: Comparison of the Forward Euler, Backward Euler and Trapezoidal methods to the exact solution in different time-step sizes

**Table 2.2**: Local error of the Forward, Backward and Trapezoidal Method to the exact solution at the selected time point

| | t | 0.1 | 0.2 | 0.3 | 0.4 | 0.5 | 0.6 | 0.7 | 0.8 | 0.9 | 1.0 |
|---|---|---|---|---|---|---|---|---|---|---|---|
| FEU | h=0.1 | 6.155 | 10.269 | 13.045 | 14.901 | 16.146 | 16.975 | 17.535 | 17.909 | 18.160 | 18.329 |
| | h=0.01 | 0.659 | 1.103 | 1.389 | 1.596 | 1.720 | 1.807 | 1.865 | 1.906 | 1.932 | 1.951 |
| | h=0.001 | 0.055 | 0.114 | 0.154 | 0.162 | 0.177 | 0.183 | 0.186 | 0.194 | 0.195 | 0.196 |
| | h=0.0001 | 0.012 | 0.024 | 0.004 | 0.021 | 0.014 | 0.020 | 0.016 | 0.018 | 0.020 | 0.020 |
| BEU | h=0.1 | 7.050 | 11.748 | 14.906 | 17.019 | 18.445 | 19.394 | 20.033 | 20.460 | 20.746 | 20.940 |
| | h=0.01 | 0.682 | 1.099 | 1.412 | 1.615 | 1.745 | 1.831 | 1.893 | 1.930 | 1.958 | 1.976 |
| | h=0.001 | 0.079 | 0.110 | 0.147 | 0.161 | 0.175 | 0.180 | 0.191 | 0.193 | 0.193 | 0.196 |
| | h=0.0001 | 0.012 | 0.021 | 0.027 | 0.020 | 0.013 | 0.017 | 0.020 | 0.018 | 0.018 | 0.020 |
| TRPZD | h=0.1 | 0.414 | 0.740 | 0.930 | 1.069 | 1.150 | 1.205 | 1.249 | 1.274 | 1.295 | 1.306 |
| | h=0.01 | 0.012 | 0.021 | 0.004 | 0.020 | 0.013 | 0.017 | 0.014 | 0.014 | 0.013 | 0.013 |
| | h=0.001 | 0.012 | 0.021 | 0.004 | 0.001 | 0.001 | 0.002 | 0.002 | 0.002 | 0.001 | 0.000 |
| | h=0.0001 | 0.012 | 0.021 | 0.004 | 0.001 | 0.001 | 0.002 | 0.002 | 0.002 | 0.001 | 0.000 |

ized accident related to the uncontrolled rod withdrawal. Therefore, it is worth performing this calculation as an extreme situation to demonstrate the stability of the three numerical solutions, particularly to see when the equations become stiff. The constants needed are listed in Table 2.4 and the set of equations will be solved

**Table 2.3**: CPU time (s) of the numerical solvers for 1s calculation

| | h=0.1 | h=0.01 | h=0.001 | h=0.0001 |
|---|---|---|---|---|
| FEU | 0.0020 | 0.0170 | 0.1510 | 1.3690 |
| BEU | 1.9280 | 18.3260 | 200.0430 | 2718.3 |
| TRPZD | 1.9270 | 19.2270 | 207.9320 | 4109.7 |

**Table 2.4**: Constants used for solving the coupled equations (Eq. 2.9)

| item | name | value | unit |
|---|---|---|---|
| fuel salt mass flow rate | $\dot{m}_f$ | 200 | kg/s |
| specific heat of fuel salt | $c_{p,f}$ | 2386 | J/kg/K |
| fuel inlet temperature | $T_{f,in}$ | 908 | K |
| fuel initial average temperature | $T_{f,avg,0}$ | 922 | K |
| fuel inventory in the core | $M_{f,c}$ | 1308 | kg |
| initial reactor power | $P_0$ | 10 | MW |
| prompt neutron life time | $\Lambda$ | 4.0E-4 | s |
| decay constant (group 1) | $\lambda_1$ | 0.0126 | 1/s |
| decay constant (group 2) | $\lambda_2$ | 0.0337 | 1/s |
| delay neutron fraction (group 1) | $\beta_1$ | 22.8E-5 | - |
| delay neutron fraction (group 2) | $\beta_2$ | 78.8E-5 | - |
| temperature feedback coefficient | $\alpha_{T,f}$ | -11.3E-5 | 1/K |
| end of calculation time | $t_{end}$ | 100 | s |
| transient initiating time | $t_{init,step}$ | 50 | s |
| reactivity insertion | $R_{insert}$ | 6.0E-3 | - |

by a MATLAB® module. The code was run on the same laptop machine.

$$\begin{cases} \dfrac{dT_f}{dt} = \dfrac{P(t) - \dot{m}_f c_{p,f}(T_{f,out} - T_{f,in})}{M_{f,c} c_{p,f}} \\ \dfrac{dP(t)}{dt} = \dfrac{R(t) + R_{insert} - \beta}{\Lambda} P(t) + \sum_{i=1}^{I} \lambda_i C_i(t) \\ \dfrac{dC_i}{dt} = -\lambda_i C_i + \dfrac{\beta_i}{\Lambda} P(t) \qquad i = 1, 2, ...I \\ R(t) = \alpha_{T,f}(T_f - T_{f,avg,0}) \end{cases} \tag{2.9}$$

The results of the transient calculation for the coupled model (Eq. 2.9) was presented in Figure 2.3, which describes the power responses with different time-step sizes. The non-convergence issue was not observed for all the numerical solvers. Furthermore, with the reduction of the time step size the explicit forward Euler method could also produce a stable and accurate solution (Table 2.5). Thus with

**Table 2.5**: Relative local error of Forward Euler and Backward Euler method referring to the Trapezoidal method at the selected time point

| | | | | | | | | | | |
|---|---|---|---|---|---|---|---|---|---|---|
| h=0.1 | | | | | | | | | | |
| FEU | 0.498 | 0.727 | 0.826 | 0.815 | 0.460 | 5.698 | 443.496 | 164.251 | 147.864 | 174.852 |
| BEU | 2.020 | 0.252 | 2.281 | 0.407 | 5.162 | 5.442 | 100.740 | 32.923 | 10.630 | 1.813 |
| h=0.05 | | | | | | | | | | |
| FEU | 0.287 | 0.468 | 0.566 | 0.526 | 0.071 | 1.699 | 2.768 | 0.302 | 0.403 | 0.275 |
| BEU | 0.966 | 2.129 | 1.463 | 0.096 | 0.601 | 0.633 | 0.463 | 0.142 | 0.196 | 0.287 |
| h=0.01 | | | | | | | | | | |
| FEU | 0.074 | 0.130 | 0.155 | 0.099 | 0.069 | 0.187 | 0.153 | 0.062 | 0.017 | 0.056 |
| BEU | 0.090 | 0.167 | 0.190 | 0.077 | 0.094 | 0.152 | 0.118 | 0.051 | 0.015 | 0.054 |
| h=0.005 | | | | | | | | | | |
| FEU | 0.038 | 0.069 | 0.081 | 0.046 | 0.038 | 0.086 | 0.069 | 0.030 | 0.007 | 0.027 |
| BEU | 0.042 | 0.078 | 0.089 | 0.041 | 0.044 | 0.077 | 0.061 | 0.027 | 0.006 | 0.026 |
| h=0.001 | | | | | | | | | | |
| FEU | 0.008 | 0.014 | 0.017 | 0.009 | 0.008 | 0.016 | 0.013 | 0.006 | 0.001 | 0.005 |
| BEU | 0.008 | 0.015 | 0.017 | 0.008 | 0.008 | 0.016 | 0.013 | 0.006 | 0.001 | 0.005 |
| h=0.0005 | | | | | | | | | | |
| FEU | 0.004 | 0.007 | 0.008 | 0.004 | 0.004 | 0.008 | 0.006 | 0.003 | 0.001 | 0.003 |
| BEU | 0.004 | 0.007 | 0.008 | 0.004 | 0.004 | 0.008 | 0.006 | 0.003 | 0.001 | 0.003 |

**Table 2.6**: CPU time (s) of the numerical solvers for 10s calculation

| | h=0.1 | h=0.05 | h=0.01 | h=0.005 | h=0.001 | h=0.0005 |
|---|---|---|---|---|---|---|
| FEU | 0.029 | 0.051 | 0.224 | 0.415 | 2.016 | 5.235 |
| BEU | 8.397 | 16.933 | 87.389 | 169.561 | 786,883 | 1551.7 |
| TRPZD | 8.434 | 16.812 | 87.048 | 169.249 | 779,799 | 1561.4 |

the help of this mathematical verification, a safe selection of a certain numerical solution and a time-step size can be ensured. So now it is not surprising to choose the more time-efficient forward Euler method to build the numerical solver for the point-kinetic equations in TRACE.

### Building the ODE-Solver

Based on the forward Euler method, the point-kinetic equations can be rewritten in the form of Eq. (2.10), where it is found that the polynome on the right hand side consists of the basic algorithm, which can be easily implemented by using the "Control Blocks" of TRACE. The "Control Blocks" provide the user with a powerful tool to realize the functions of the signal-related operating units, such as the time-related, algorithm, calculus, logical, switch and measurement components (Table 2.7). Therefore, the Eq. (2.10) can be sliced into many small items and each of them has only one single basic operation, for instance, sum, multiply or divide,

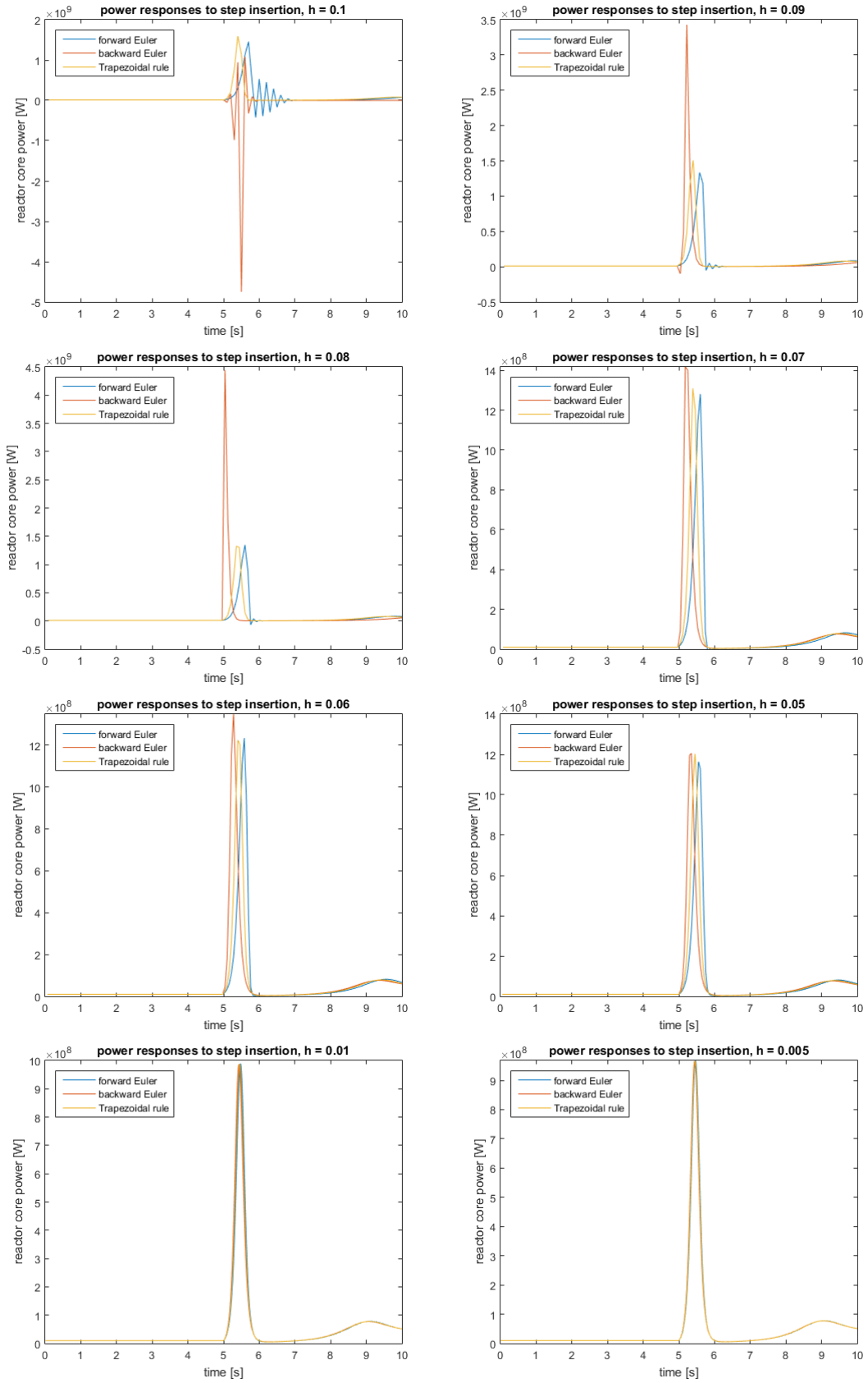


**Figure 2.3**: Comparison of the Forward Euler, Backward Euler and Trapezoidal methods for the power responses to 600pcm step insertion of reactivity with different time-step sizes

which then can be converted to a single "Control Block". Specifically, the operation of the item $\frac{R(t)-\beta}{\Lambda}N(t)$ can be divided into four sequential steps:

1. measure the time-dependent reactivity feedback $R(t)$ from fuel and graphite,
2. minus the delayed neutron fraction: $R(t)-\beta$,
3. be divided by the prompt neutron generation time: $\frac{R(t)-\beta}{\Lambda}$
4. multiply the neutron population: $\frac{R(t)-\beta}{\Lambda}N(t)$,

which then can be "graphically" programmed by applying the blocks of *Sum*, *Subtract*, *Divide* and *Multiply* (Figure 2.4). The *Input Switch* is a critical node to close the iteration loop of the Euler method. It helps to read the initial condition through its second channel ($X_2$) when $t=0$ is true ($X_3=1$) and switch to read the result calculated by the initial condition on the first channel ($X_1$) when $t=0$ is false ($X_3=0$) and then the output of the *Input Switch* will be used as the input for the calculation of the next step and finally the result will be sent back to the first channel of this *Input Switch* again. In addition, the time-step size ($h$) is controlled by the block "*Current Timestep Size*", which guarantees that the ODE-solver and the computational engine of the thermal-hydraulics of the TRACE code are using the same step size for all time points.

$$\begin{cases} N(t+h) = N(t) + h \cdot [\dfrac{R(t)-\beta}{\Lambda}N(t) + \sum\limits_{n=1}^{6}\lambda_i C_i(t)] \\ C_i(t+h) = C_i(t) + h \cdot [-\lambda_i C_i + \dfrac{\beta_i}{\Lambda}N(t) - \dfrac{C_i(t)}{\tau_c} + \dfrac{C_i(t-\tau_l)}{\tau_c}e^{-\lambda_i \tau_l}] \end{cases} \tag{2.10}$$

According to this approach, finally we built a complex "circuit solver" (Figure 2.5) to achieve the dynamic calculation of the neutron population with six groups. The group constants (Table 2.8) were offered by another control system built mostly with the block "*Constant*" (Figure 2.6). In a word, the input of this circuit is a time-dependent reactivity ($R(t)$) composed of the reactivity feedback from the fuel salt and graphite, the given initial reactivity and the external reactivity insertion. The output of this circuit is the reactor core power connected to the "*Fluid Power*", which heats up the fuel salt and in turn the fuel salt produces the temperature

**Table 2.7**: Some necessary control blocks to build the ODE-solver for the point-kinetic equations

| block name | Input | Operation | Output |
|---|---|---|---|
| Problem Time | | | $t$ |
| Current Timestep Size | | | $h$ |
| Delay | $X(t), \delta t$ | delay | $X(t-\delta t)$ |
| Constant | $X_1$ | | $X_1$ |
| Sum | $X_i$ | sum | $\sum_{i=1}^{n} X_i$ |
| Subtract | $X_1, X_2$ | subtract | $X_1 - X_2$ |
| Multiply | $X_1, X_2$ | multiply | $X_1 \cdot X_2$ |
| Divide | $X_1, X_2$ | divide | $\frac{X_1}{X_2}$ |
| Exponentiate | $X_1$ | exponentiate | $exp(X_1)$ |
| Logical AND | $X_1, X_2$ | judge $X_1 = 1 \& X_2 = 1$ | 0 or 1 |
| Greater Than or Equal to | $X_1, X_2$ | judge $X_1 \geq X_2$ | 0 or 1 |
| Input Switch | $X_1, X_2, X_3$ | judge $X_3 = 1$ or not | $X_1, (X_3 = 1); X_2(X_3 \neq 1)$ |
| Pressure Signal | $p_{i,j}$ | measure | $p_{i,j}$ |
| Temperature Signal | $T_{i,j}$ | measure | $T_{i,j}$ |
| Mass Flow Rate | $m_{i,j}$ | measure | $m_{i,j}$ |

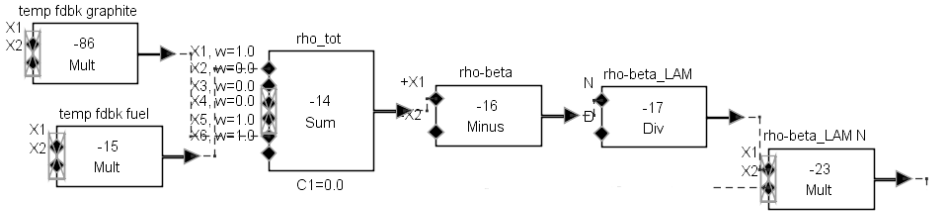


**Figure 2.4**: Graphical expression of the item $\frac{R(t)-\beta}{\Lambda}N(t)$ in point-kinetic equation using control blocks

feedback referring to the set-point of the fuel temperature.

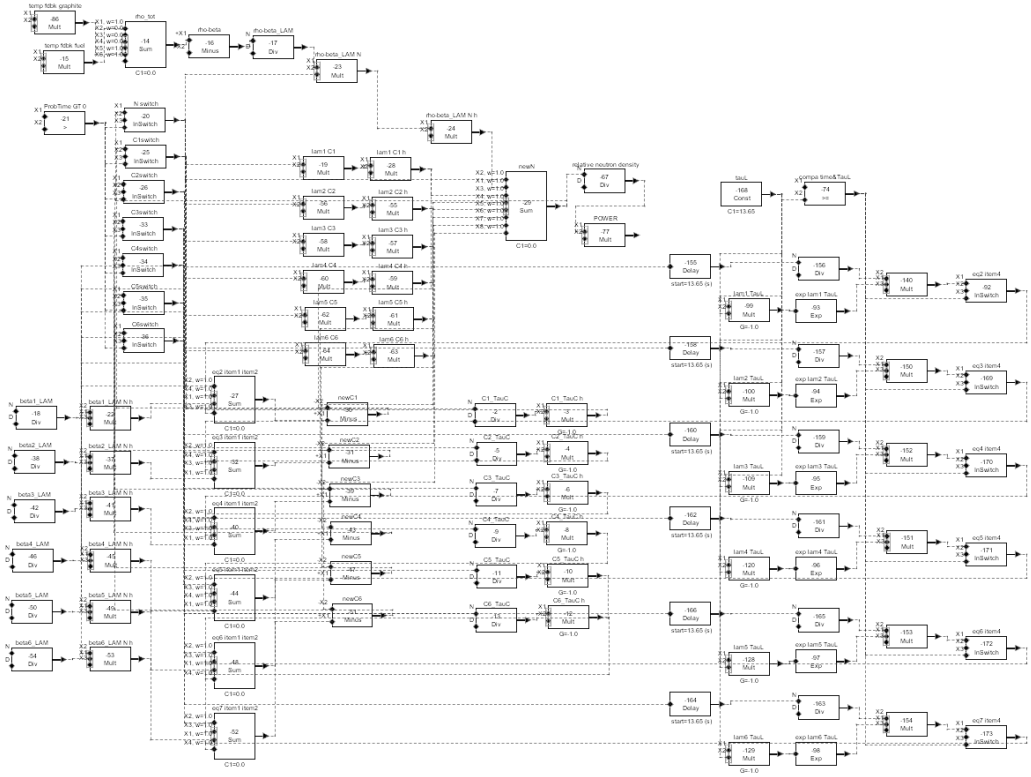

**Figure 2.5**: The circuit for solving the point-kinetic equations

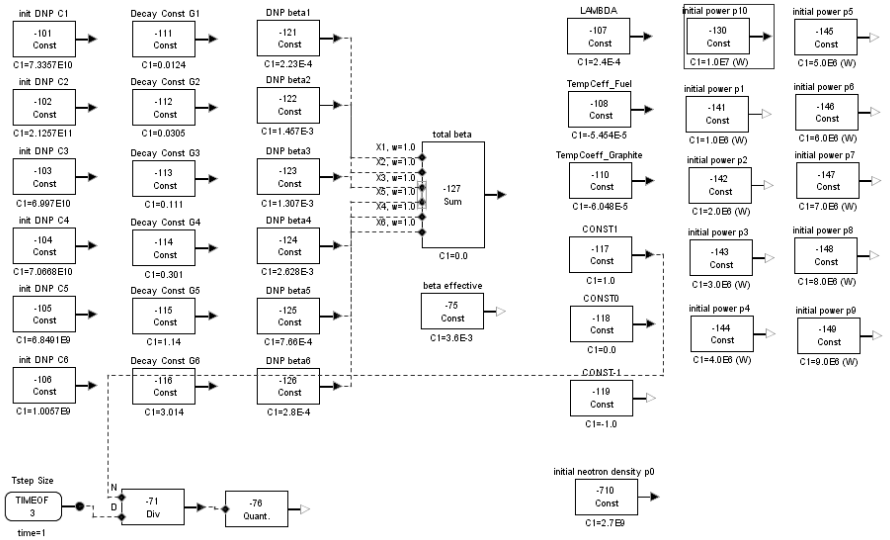


**Figure 2.6**: The control system offering the group constants

**Table 2.8**: Point-kinetic parameters of $^{233}$U- and $^{235}$U-based fuel for MSRE [33]

| | Unit | $^{235}$U-based | $^{233}$U-based |
|---|---|---|---|
| fuel temperature coefficient | pcm/K | -8.71 | -11.3 |
| graphite temperature coefficient | pcm/K | -6.66 | -5.81 |
| neutron generation time | s | 2.4E-4 | 4.0E-4 |
| compensative reactivity | pcm | 245.92 | 111.7 |
| decay constant | | | |
| group 1 | 1/s | 0.0124 | 0.0126 |
| group 2 | 1/s | 0.0305 | 0.0337 |
| group 3 | 1/s | 0.1110 | 0.1390 |
| group 4 | 1/s | 0.3010 | 0.3250 |
| group 5 | 1/s | 1.1400 | 1.1300 |
| group 6 | 1/s | 3.0140 | 2.5000 |
| delayed neutron fraction | | | |
| group 1 | – | 22.3E-5 | 22.8E-5 |
| group 2 | – | 145.7E-5 | 78.8E-5 |
| group 3 | – | 130.7E-5 | 66.4E-5 |
| group 4 | – | 262.8E-5 | 73.6E-5 |
| group 5 | – | 76.6E-5 | 13.6E-5 |
| group 6 | – | 28.0E-5 | 8.8E-5 |

**Table 2.9**: The formulas for calculating the parameters of the physical properties (fuel&coolant salt) [22] [23] [29]

| item | Unit | Working Fluids | Formula |
|---|---|---|---|
| Density | kg/m$^3$ | Fuel | $\rho_f(T) = 2810.7 - 0.6707 \cdot (T - T_{melt})$ |
| | | Coolant | $\rho_c(T) = 2279.7 - 0.4884 \cdot (T - 273.15)$ |
| Viscosity | Pa·s | Fuel | $\mu_f(T) = 8.4 \cdot 10^{-5} exp(4340/T)$ |
| | | Coolant | $\mu_c(T) = 1.16 \cdot 10^{-4} exp(3755/T)$ |
| Heat Capacity | J/(kg·K) | Fuel | $c_{p,f} = 1884$ |
| | | Coolant | $c_{p,c} = 2386$ |
| Thermal Conductivity | W/(m·K) | Fuel | $\kappa_f = 1.0$ |
| | | Coolant | $\kappa_c = 1.1$ |
| Surface Tension | N·m | Fuel | $\sigma_f = 0.004778$ |
| | | Coolant | $\sigma_c(T) = -1.2 \cdot 10^{-4}(T - 273.15) + 0.26$ |
| Melting Point | $K$ | Fuel | $T_{melt,f} = 722.15K$ |
| | | Coolant | $T_{melt,c} = 731.15K$ |

### Modification of the Fluid Library

Originally TRACE provides the users with seven working fluids including water, heavy water, nitrogen, air, helium, sodium and lead-bismuth. Here the sodium and the lead-bismuth were selected to be replaced by the new physical properties of the

fuel salt ($^7$LiF-$BeF_2$-$ZrF_4$-$UF_4$) and the coolant salt ($^7$LiF-$BeF_2$) respectively. It is reasonable to choose these two fluids, because only one phase is basically allowed for sodium and lead-bismuth in original version and comparing to other fluids their physical properties are somewhat close to the molten salts.

In the source code of TRACE there are three subroutines related to the fluid library: *EosDataM*, *EosInitM* and *EosM*. The *EosDataM* defines the fluid index and the molecular weight for each fluid. The *EosInitM* gives the initial values of the physical properties at the reference temperatures or pressures as well as the upper or lower limit of the temperatures and pressures for the calculation. The *EosM* contains all the important formulas to work out the temperature- or pressure-dependent properties. According to the ORNL's report about the physical properties of the fuel and coolant salts, the following formulas (Table 2.6) were newly written into the source code.

# Chapter 3

# MSRE System Modeling with TRACE

## 3.1 General Description of the MSRE System

This chapter has two main topics. One is about the introduction of the main components in the MSRE system, while another is about the methodology of the simplified or equivalent modeling with TRACE for the MSRE components.

The MSRE system has two loops (Figure 3.1). The fuel salt also as the primary coolant ($^7$LiF-$BeF_2$-$ZrF_4$-$UF_4$) flows in the primary loop, while the intermediate coolant salt ($^7$LiF-$BeF_2$) flows in the secondary loop. The primary loop contains a reactor vessel, an intermediate heat exchanger (shell-side) and a centrifugal sump-type pump for the fuel circulation, while the secondary loop includes the tube-side of the heat exchanger, another centrifugal pump for the coolant circulation and a radiator cooled by two blowers with the air. Additionally, two sub-critical drain tanks for the fuel salt parking and a flush tank for the storage of the loop flushing salt are connected to the reactor vessel and another drain tank for the intermediate coolant salt is installed in the secondary loop. However, since the process of discharging the fuel and coolant salts were not considered in this work, so the drain tanks or the flush tank were not built in the TRACE model.

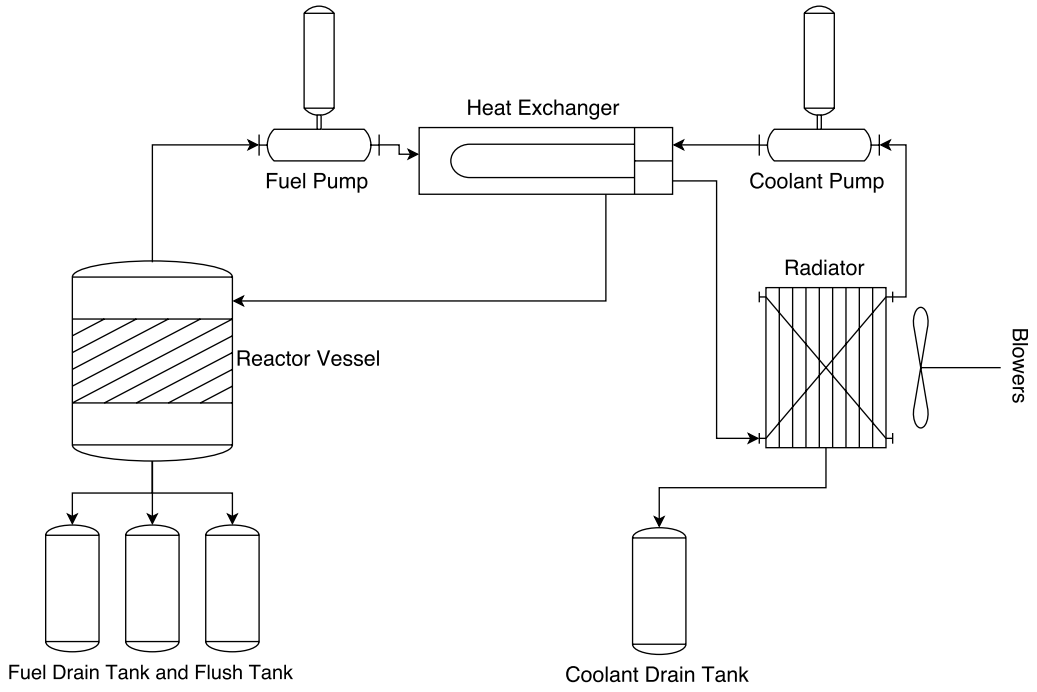


**Figure 3.1**: The MSRE loop layout

## 3.2 Component Description and TRACE Modeling

### 3.2.1 Reactor Vessel

The reactor vessel (Figure 3.2) of the MSRE is about 2.438m (8 ft.) high with a diameter of 1.524m (5 ft.). Because of the low operating pressure the thickness of the reactor vessel is only about 0.01429m (9/16 in.) in the cylindrical portion and 0.0254m (1 in.) in the top region separately. At the entrance of the reactor vessel there is a flow distributor, which distributes the fuel salt uniformly into the annular down comer through 84 holes around the vessel's wall. At the exit of the down comer there are 48 anti-swirl vanes helping maintain the flow in laminar regime. The reactor core wrapped in the core can consists of 513 graphite blocks, which are supported by the supporting grid at the bottom of the reactor core entrance. The structure of the graphite block as well as the flow channel for the fuel salt was illustrated in Figure 3.3. The top of each graphite block is tapered in order to reduce the amount of the remaining fuel salt in the reactor core after the draining process. Furthermore, three control rods and a removable sample rod containing some specimens of the structural and moderator materials are positioned in the center region

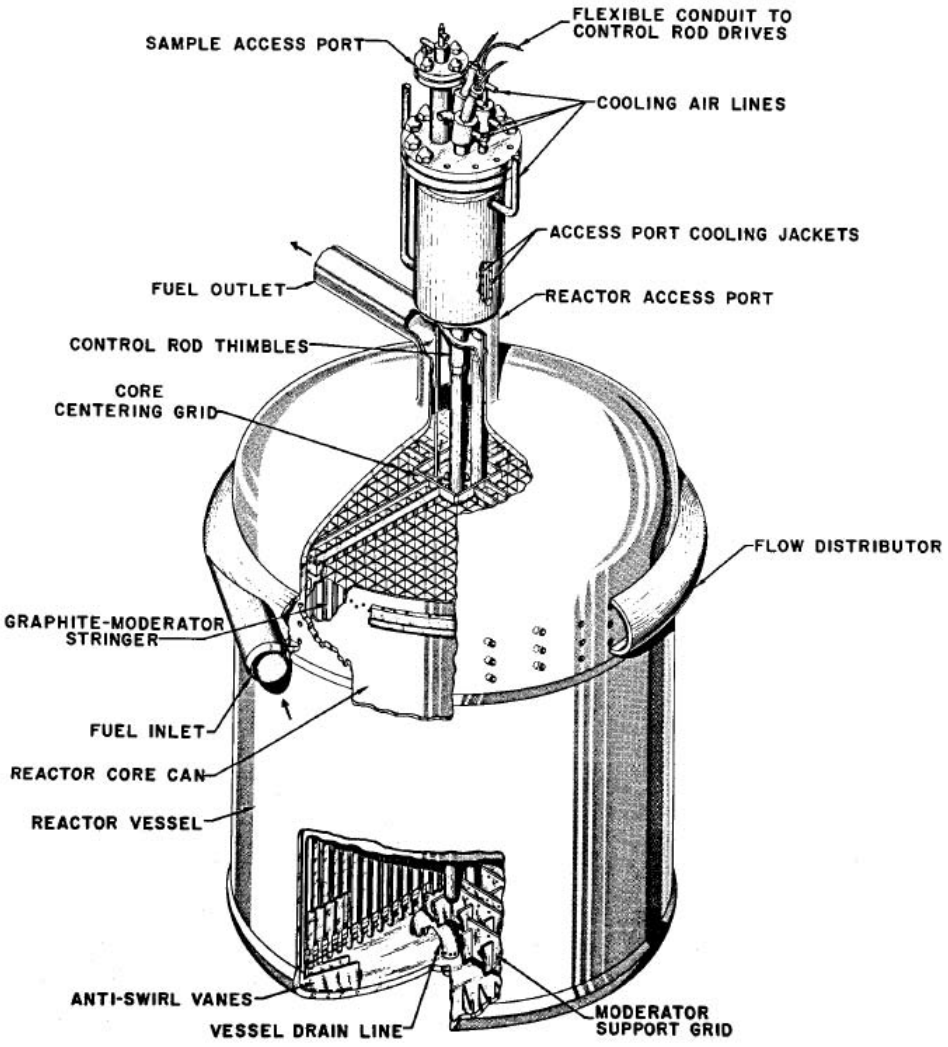


**Figure 3.2**: MSRE reactor vessel[24]

of the reactor core (Figure 3.4). Other important design data for the modeling is listed in Table 3.1.

Since the dynamic behavior of the entire MSRE system is concerned here, the in-core structures like the supporting grid or the anti-swirl vanes were neglected. On the other hand, principally the TRACE code is only capable for the 1D thermal-hydraulic simulation, so the components with the complex 3D geometry were modeled in an equivalent way. For instance, the graphite core with fuel channels were modeled as a tube bundle, which has the same number of the tubes as the fuel channels in the reactor core. Besides, each tube has the same flow area and hydraulic

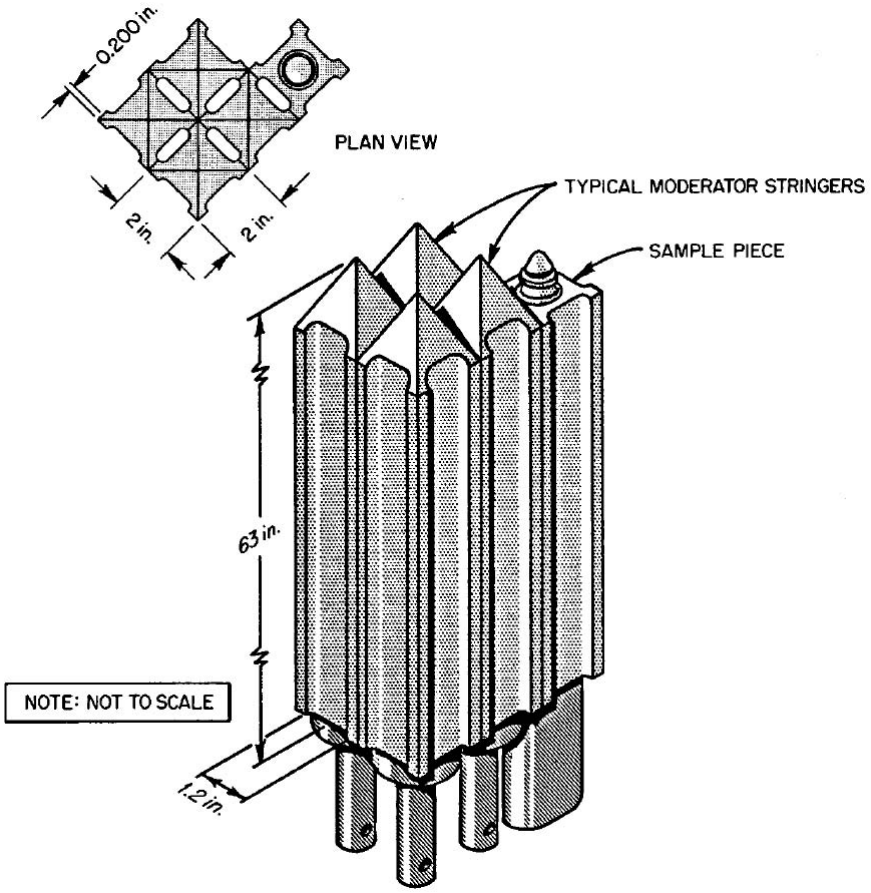


**Figure 3.3**: MSRE graphite block[24]

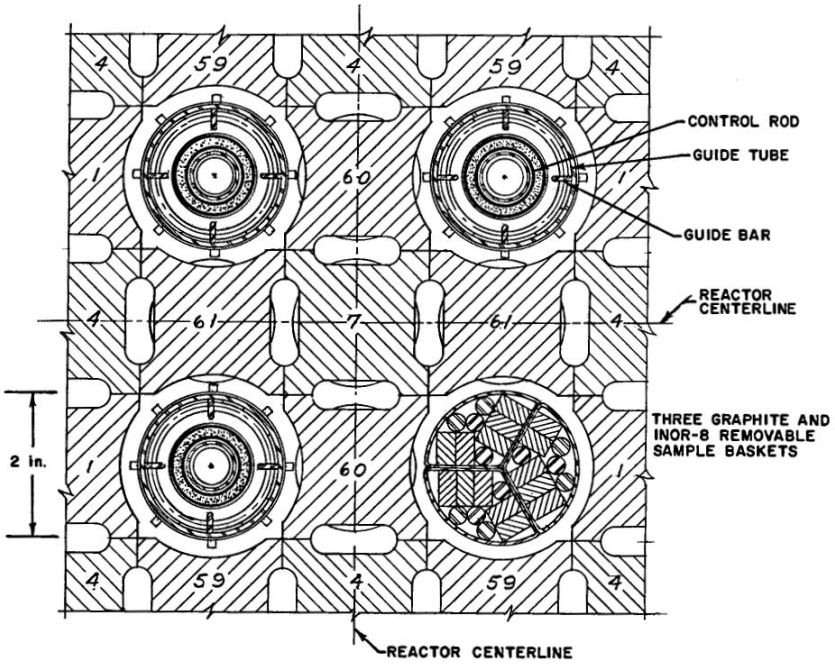


**Figure 3.4**: MSRE control rod and sample rod[24]

**Table 3.1**: Geometric data for MSRE reactor core and vessel

| Name | value | unit |
|---|---|---|
| height of reactor core | 1.6256 | m |
| diameter of reactor core | 1.397 | m |
| side length of graphite block in cross section | 0.0508 | m |
| the radius of the arc edge of the flow channel | 0.01016 | m |
| the length of the straight edge of the flow channel | 0.03048 | m |
| flow area of single flow channel | 2.8755E-4 | $m^2$ |
| hydraulic diameter of single flow channel | 0.015852 | m |
| number of flow channels counting the fractional ones | 1140 | - |
| height of the plenum | 0.1744 | m |
| height of the down comer | 1.6256 | m |
| hydraulic diameter of the down comer | 0.0508 | m |

diameter as the real fuel channel, which guarantees the same fuel volume and flow conditions such as the same Reynolds number during the operation. Moreover, the graphite region between the flow channels were built with the "*heat structure*" component, which was usually used to define the solid domain between two fluid domains for the heat transfer calculation. For the current work the graphite block was modeled as the "tube wall" having the thickness equal to the distance between the block axis to the inner surface of the new equivalent flow channel (Figure 3.5). Based on this symmetric model and on the hypothesis of a homogeneous power distribution, the outer boundary of the tube can be assumed to be adiabatic. Finally, the material properties of the graphite and the structures (INOR-8) can be added to the user-defined material library according to Table 3.2.

The rough half-ellipsoid upper/lower plenum was modeled with a "*pipe*" component having the same diameter as the reactor vessel and roughly the same volume as the real plenum. The annular down comer was equivalently built also with a "*pipe*" component having the same height as the core and the same flow area as well as the hydraulic diameter as the original one. Since the down comer model was a single "*pipe*", which means the flow distribution inside is already homogeneous, thus the modeling of the flow distributor can be neglected.

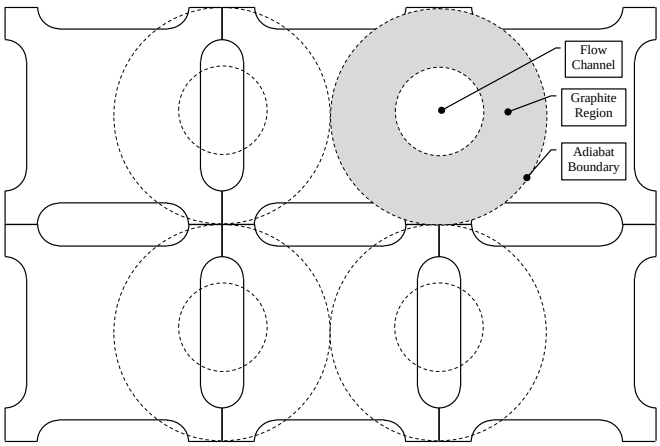


**Figure 3.5**: Equivalent modeling for the flow channel in TRACE

**Table 3.2**: Material properties of the graphite and INOR-8

| Temperature [K] | Density [kg/m$^3$] | Heat capacity [J/(kg·K)] | Thermal conductivity [W/(m·K)] | Emissivity - |
|---|---|---|---|---|
| graphite | | | | |
| 588.0 | 2160.0 | 1380.0 | 200.0 | 0.75 |
| 813.0 | 2160.0 | 1630.0 | 200.0 | 0.75 |
| 923.0 | 2160.0 | 1760.0 | 200.0 | 0.75 |
| 1033.0 | 2160.0 | 1890.0 | 200.0 | 0.75 |
| 1143.0 | 2160.0 | 2010.0 | 200.0 | 0.75 |
| 1253.0 | 2160.0 | 2130.0 | 200.0 | 0.75 |
| 1363.0 | 2160.0 | 2240.0 | 200.0 | 0.75 |
| 1473.0 | 2160.0 | 2350.0 | 200.0 | 0.75 |
| 1583.0 | 2160.0 | 2450.0 | 200.0 | 0.75 |
| INOR-8 | | | | |
| – | 8774.5 | 577.8 | 21.98 | 0.2 |

### 3.2.2 Intermediate Heat Exchanger

The intermediate heat exchanger (IHX) used in the MSRE system is a so-called shell-and-tube heat exchanger (Figure 3.6). Its overall shell length is about 2.4384m (8 ft.) and the shell diameter is about 0.4m (16 in.). The IHX has 159 U-tubes in total and the average length of the tubes is 4.2672m. Six 25%-cut baffle plates are installed in the shell enhancing the heat transfer efficiency. The geometric data of the IHX for the modeling is summarized in Table 3.3. The basic approach for the IHX modeling in TRACE is to build the shell and the U-tube bundle separately with three "*pipe*" components. The first "*pipe*" was built for the shell side having

**Table 3.3**: Geometric data of the intermediate heat exchanger

| Name | value | unit |
|---|---|---|
| Overall shell length | 2.4384 | m |
| Active shell length | 1.8288 | m |
| Shell diameter | 0.4046 | m |
| Outer diameter of the tubes | 0.0127 | m |
| Thickness of the tubes | 0.001 | m |
| Average length of the tubes | 4.2672 | m |
| Number of the tubes | 159 | - |
| Length of the coolant salt header | 0.2223 | m |

the same active shell length and the same hydraulic diameter. The second and the third "*pipes*" were separately built as two tube bundles in half-U form. The heat transfer between the fuel salt in shell-side and the coolant salt in tube-side was realized by associating all the "*pipes*" with a "*heat structure*" which has the same geometry and the material property as the U-tubes. The coolant header was divided into two separate "*pipes*" in TRACE. One is for the coolant salt inlet, while another is for coolant salt outlet. Each "*pipe*" has the same length, flow area and hydraulic diameter as the coolant salt header of the original design. On the other hand, the model of the baffle plates were neglected, because the flow behavior near the baffle plates is too complicated to model with a 1D code.

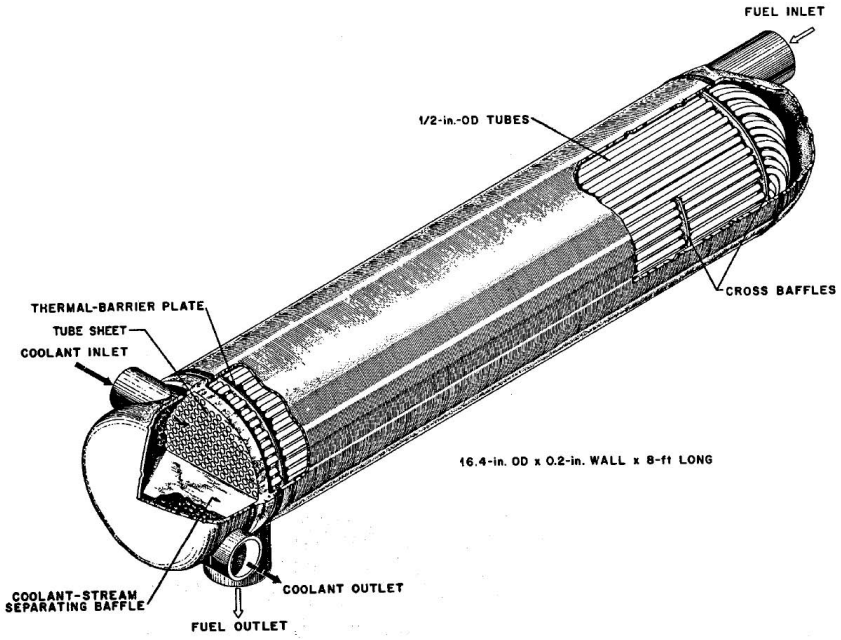


**Figure 3.6**: MSRE intermediate heat exchanger[24]

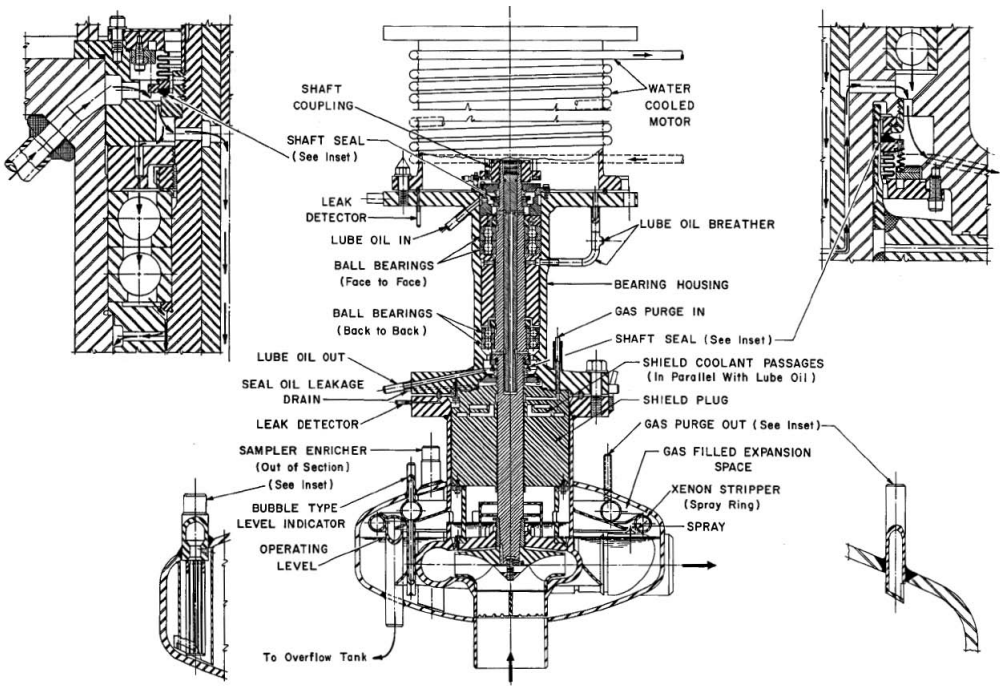


**Figure 3.7**: Fuel circulating pump of the MSRE[24]

### 3.2.3 Fuel&Coolant Circulating Pump

The fuel and coolant circulating pumps are both the same centrifugal sump-type pump (Figure 3.7). The fuel circulating pump is driven by a 56kW motor through a vertical shaft and produces a mass flow rate of about 200kg/s ( 1200 gallon/min.) for the normal operation. The pump bowl is about 0.9144m (36 in.) in diameter and the entire height of the pump assembly including the motor is about 2.4384m (8 ft.). The design of the coolant circulating pump is mostly identical with the fuel circulating pump. The main difference between these two pumps is that they have different hydraulic characteristics, such as different operating speeds and impeller diameters.

Instead of stabilizing the system pressure through a pressurizer, the MSRE system implements the pressurizing through the overflow pipe located inside the pump bowl. In particular, the liquid level in the pump bowl rises due to the fuel salt expansion and when the nozzle of the overflow pipe is submerged by the liquid level, the fuel salt will be discharged through the pipe into the overflow tank installed under the pump bowl. Thus the fuel circulating pump of the MSRE system serves also for releasing the pressure overload. Moreover, the helium flows into the pump bowl to

remove the fission gas like xenon and krypton to the off-gas disposal system. Simultaneously the helium also protects the structures from the air and water vapor, which will likely react with the florid salt to become a very corrosive acid to the structural material.

Based on the description above three main requirements should be satisfied for the pump model in TRACE:

1. It is very clear that the flow rate of the pump can be controlled according to various scenarios of the pump transients or accidents.
2. The expanded fuel salt can be discharged at the pump or the pressures at the inlet&outlet of the pump remains nearly constant.
3. The component configuration should be simplified as much as possible, because for a preliminary study on the entire loop system, the point of the pump model is just to give a adjustable driving force for the fuel circulation.

Therefore, it seems not suitable to use the built-in "*pump*" component or the "*pump with single junction component (SJC)*" in TRACE. This consideration is based on following two reasons:

1. the "*pump*" component in TRACE was developed for the pumps used in a BWR or a PWR originally and the detailed design data required by the component configuration in TRACE is not available in the ORNL's reports.
2. the "*SJC pump*" has a simple component configuration, but it doesn't have the capability of simulating the release of the fuel salt expansion.

Thus a new equivalent way of modeling the salt circulating pump is to use the component combination "*fill*"&"*break*" of TRACE. Specifically speaking, the "*break*" component simulating the pump inlet gives a constant pressure boundary condition, while the "*fill*" component defines the boundary condition at the outlet of the pump. The boundary condition of the fuel temperature used in the "*fill*" component is associated with the temperature at the inlet of the "*break*" component to solve the problem of temperature continuity in the pump. The mass flow rate is controlled by the corresponding control system. The approach of the pump modeling is shown in Figure 3.8.

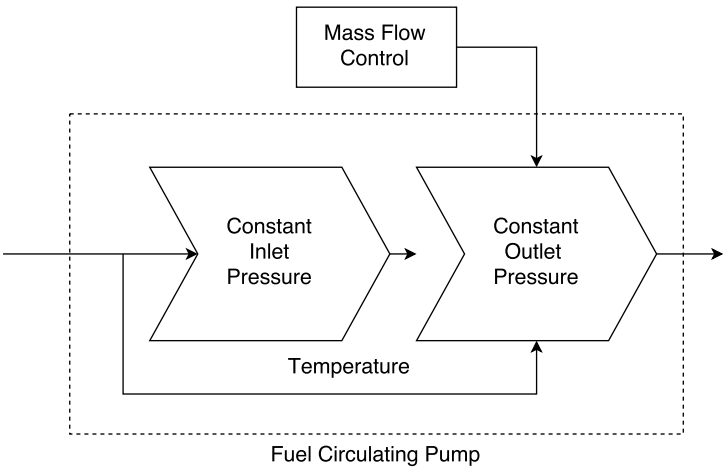


**Figure 3.8**: Equivalent pump modeling approach

### 3.2.4 Radiator

The design of the radiator is presented in Figure 3.9. The radiator has 120 tubes with 0.01905m (0.75 in.) in outer diameter and 9.144m (30 ft.) in length averagely. The cooling air flows through the radiator in the direction vertical to the plane of the coil tubes. The tubes are arrayed triangularly with a pitch length of 0.0381m (1.5 in.). The mass flux of the cooling air is controlled by two doors hanged over the radiator enclosure by the drive mechanism, which can quickly adjust the flow area of the cooling air.

The equivalent radiator model in TRACE consists of four parts: the coil tubes, air flow channel, main headers and sub-headers. The door drive mechanism was simply modeled with the "*fill*" component, which can give a fast control on the mass flux of the cooling air. The coil tubes composed of three "*pipe*" components were modeled as a tube bundle, while the flow channel of the cooling air was also built with the "*pipe*" component having roughly the same hydraulic diameter as the real one. What should be noticed is that due to the limitation of the dimensionality in TRACE, the cooling air channel can only be built on the same plane, where the coil tubes are located (Figure 3.12). The inlet and the outlet of the tube bundle were connected to the main headers and sub-headers giving extra volume for the fluid mixing. The geometric data for the modeling is given in Table 3.4.

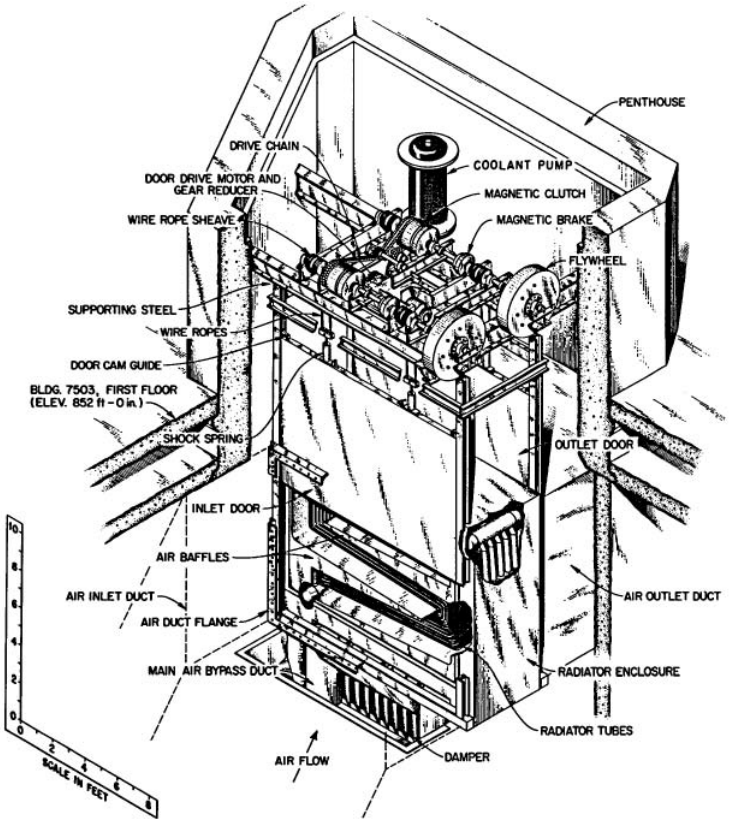


**Figure 3.9**: Radiator of the MSRE[24]

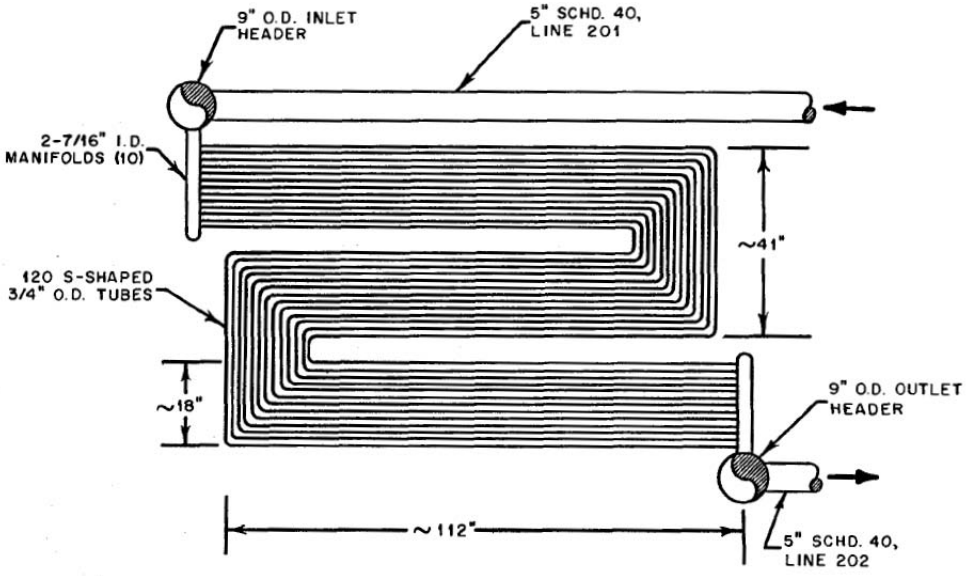


**Figure 3.10**: Radiator coil tubes[24]

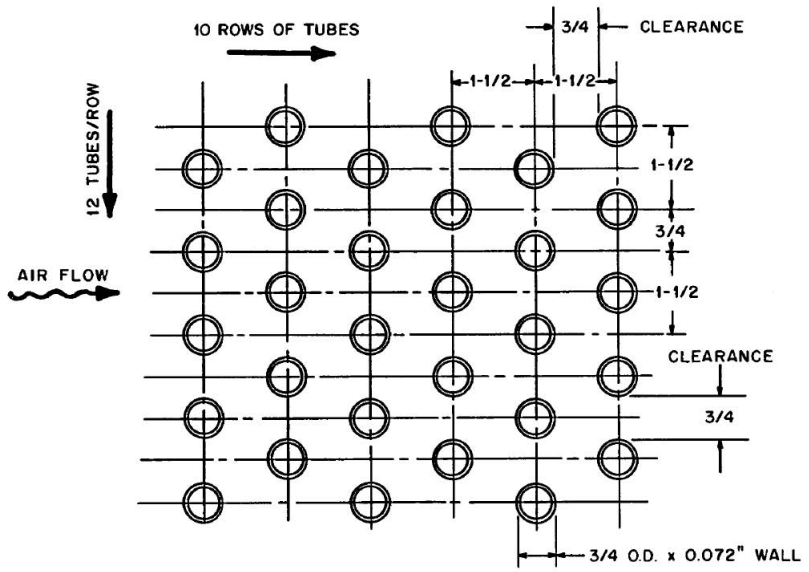


**Figure 3.11**: Radiator tube array[24]

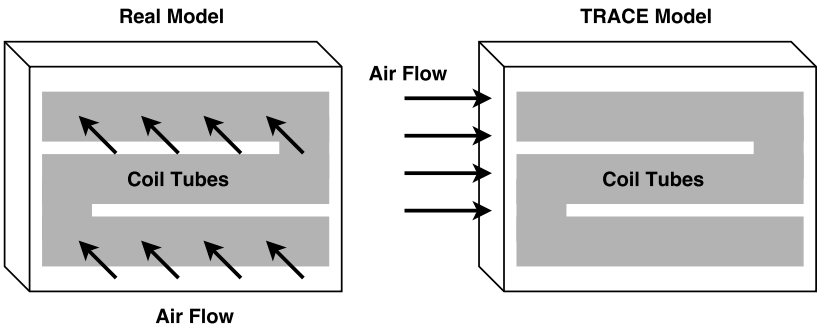


**Figure 3.12**: Equivalent model of the radiator in TRACE

### 3.2.5 Pipelines

The pipelines between the main components in the primary and secondary loops were built with the "*pipe*" component. The exact lengths of the pipes seem hardly available in the ORNL's reports, thus the lengths of the pipelines were estimated through the mass flow rate of the working fluids and the transporting time between the components. One requirement of this estimation should be roughly satisfied, that is to have a comparable total circulating time of the working fluids in the primary and secondary loops. On the other hand, the diameters of the pipelines can be obtained by the nozzle parameters of each component. Table 3.5 gives an overview about the pipeline models.

**Table 3.4**: Geometric data of the radiator

| Name | value | unit |
|---|---|---|
| Radiator enclosure | - | m |
| Average tube length | 9.144 | m |
| Tube outer diameter | 0.01905 | m |
| Tube wall thickness | 0.0183 | m |
| Pitch length of the tube array | 0.0381 | m |
| Diameter of the main headers | 0.2032 | m |
| Diameter of the sub-headers | 0.0635 | m |
| Hydraulic diameter for the air flow channel | 0.10014 | m |

**Table 3.5**: Geometric data of the pipeline models

| Name | inner diameter [m] | pipe length [m] |
|---|---|---|
| Reactor to fuel pump | 0.127 | 1.934 |
| Fuel pump to heat exchanger | 0.127 | 0.530 |
| Heat exchanger to reactor | 0.127 | 3.967 |
| Heat exchanger to radiator | 0.127 | 7.000 |
| Radiator to coolant pump | 0.127 | 6.217 |
| Coolant pump to heat exchanger | 0.127 | 1.000 |

After the discussion of all main components, the MSRE system model with two loops was built with TRACE (Figure 3.13). Table 3.6 gives a summary about the "*hydraulic components*" and the "*heat structures*" used to build the TRACE model.

### 3.2.6 Control Systems

Except the "circuit solver" for the point-kinetic equations shown in the previous chapter, other control circuits need to be built in order to realize the functions like detecting the temperatures of the fuel and graphite, inserting the step-wise or ramp-wise reactivity, adjusting the flow rate of the pumps, initializing the power deposition to the fluid and calculating the transient times in the reactor core and the external loop. In following each control system was presented with its mathematical explanation.

**System of the Temperature Detection**

In order to realize the temperature reactivity feedback to the point-kinetic model, the average fuel salt&graphite temperature in each time step must be detected and

**Table 3.6**: Overview of the components in the TRACE model

| Component name | Component type | Component number | Node number |
|---|---|---|---|
| lower plenum | pipe | 20 | 3 |
| reactor core | pipe | 11 | 10 |
| graphite block | heat structure | 58 | 10 |
| upper plenum | pipe | 21 | 3 |
| pipeline (reactor to fuel pump) | pipe | 22 | 6 |
| fuel pump inlet | break | 30 | 1 |
| fuel pump outlet | fill | 31 | 1 |
| pipeline (fuel pump to heat exchanger) | pipe | 23 | 2 |
| heat exchanger shell-side | pipe | 51 | 10 |
| pipeline (heat exchanger to reactor, part 1) | pipe | 24 | 3 |
| pipeline (heat exchanger to reactor, part 2) | pipe | 25 | 10 |
| down comer | pipe | 26 | 10 |
| coolant inlet header | pipe | 54 | 2 |
| U-tube, part 1 | pipe | 52 | 10 |
| tube wall, part 1 | heat structure | 56 | 10 |
| U-tube, part 2 | pipe | 53 | 10 |
| tube wall, part 2 | heat structure | 57 | 10 |
| coolant outlet header | pipe | 55 | 2 |
| pipeline (heat exchanger to radiator, part 1) | pipe | 62 | 5 |
| pipeline (heat exchanger to radiator, part 2) | pipe | 63 | 10 |
| radiator inlet main header | pipe | 73 | 1 |
| radiator inlet sub-header | pipe | 74 | 1 |
| radiator coil tube, part 1 | pipe | 70 | 10 |
| tube wall, part 1 | heat structure | 90 | 10 |
| radiator coil tube, part 2 | pipe | 71 | 10 |
| tube wall, part 2 | heat structure | 91 | 10 |
| radiator coil tube, part 3 | pipe | 72 | 10 |
| tube wall, part 3 | heat structure | 92 | 10 |
| radiator outlet sub-header | pipe | 75 | 1 |
| radiator outlet main header | pipe | 76 | 1 |
| pipeline (radiator to coolant pump, part 1) | pipe | 64 | 10 |
| pipeline (radiator to coolant pump, part 2) | pipe | 65 | 3 |
| coolant pump inlet | break | 33 | 1 |
| coolant pump outlet | fill | 32 | 1 |
| pipeline (coolant pump to heat exchanger) | pipe | 61 | 5 |
| door drive mechanism of the radiator | fill | 81 | 1 |
| air flow channel in the radiator | pipe | 80 | 10 |
| outlet of the air flow channel | break | 82 | 1 |

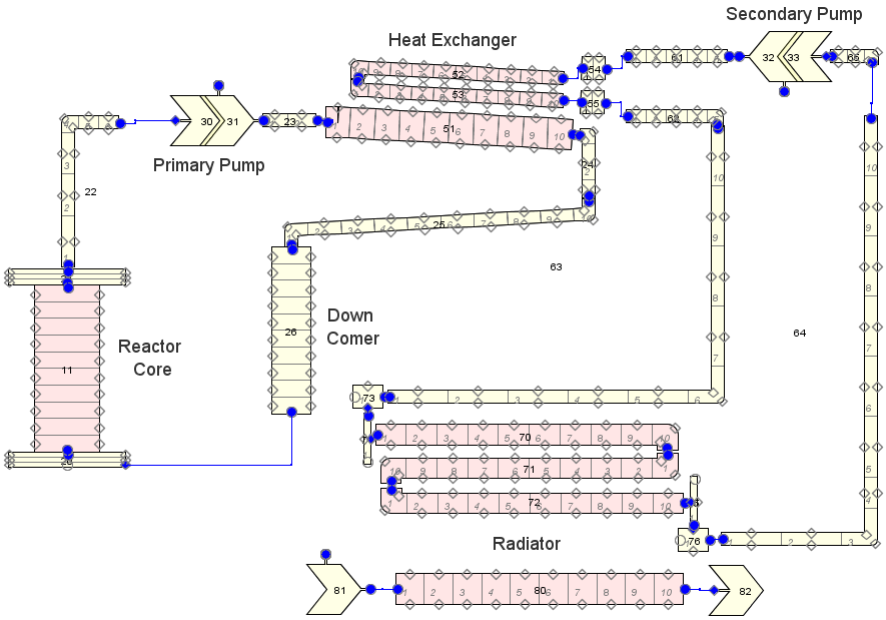


**Figure 3.13**: TRACE loop model of the MSRE system

associated with the reactivity input block of the ODE-solver for the point-kinetic equations (Figure 2.5). For this purpose the signal components like "*volumetric signal*" and "*heat signal*" were introduced to measure the real-time temperatures of the specific node of the working fluid and the structures respectively. With the help of the arithmetic blocks, the average temperatures of the "*hydraulic component*" or the "*heat structure*" can be calculated. Figure 3.14 and Figure 3.15 present the system for detecting and calculating the fuel&graphite average temperatures and their mathematical expressions are shown in Eq. 3.1 and Eq. 3.2.

For Figure 3.14 its mathematical expression can be written as follows:

$$\frac{\sum_{j=1}^{N} T_f^j(t)}{\sum_{j=1}^{N} j} - T_{f,avg,0} \longrightarrow \Delta T_f(t) \tag{3.1}$$

where the $N$ is the number of the component nodes, while the $j$ is the node number.

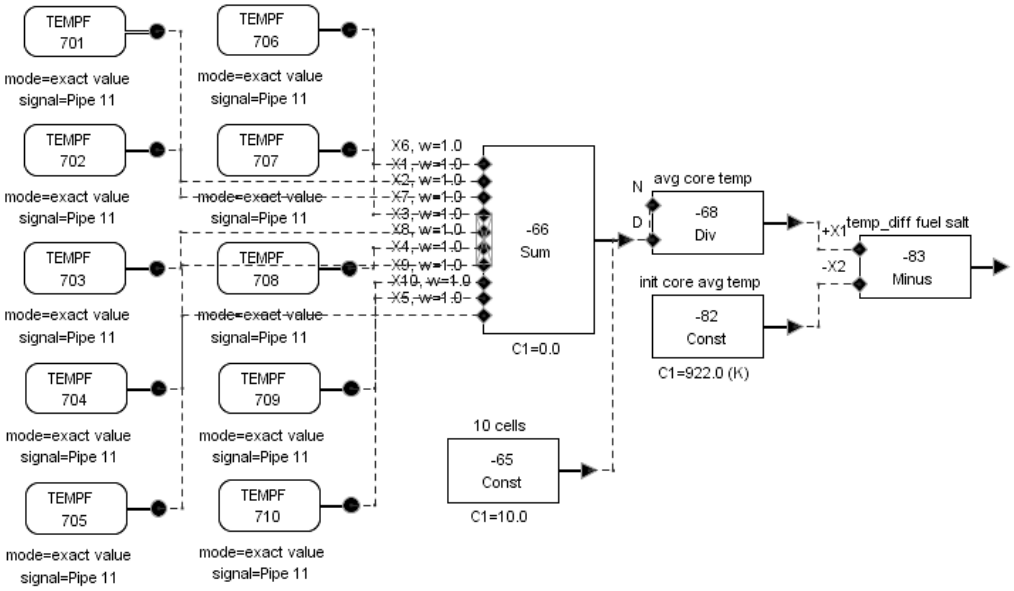


**Figure 3.14**: System for detecting the average temperature of the fuel salt

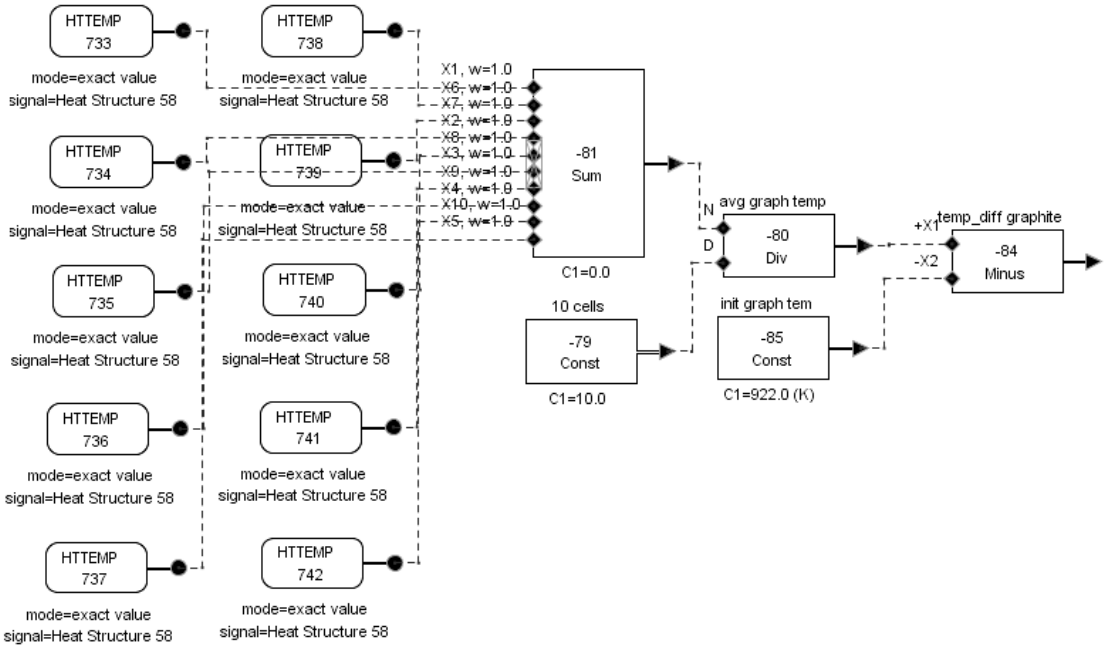


**Figure 3.15**: System for detecting the average temperature of the graphite blocks

Similar to this, the mathematic explanation for Figure 3.15 can be written as follows:

$$\frac{\sum_{j=1}^{N} T_g^j(t)}{\sum_{j=1}^{N} j} - T_{g,avg,0} \longrightarrow \Delta T_g(t) \tag{3.2}$$

**System of the Reactivity Insertion**

Figure 3.16 and Figure 3.17 illustrate the control system for manually inserting the reactivity as required by the safety analysis. In fact, the "*Step*" and "*Ramp*" blocks are already provided by TRACE, but here the systems were built through the combination of the arithmetic and logical blocks to produce the same controlling behavior. One advantage of doing this is to have an extended flexibility of controlling for more complex signal inputs for future studies, for instance, to be able to perform a ramp insertion with a time-dependent rate, to implement a staircase reactivity insertion or to regulate the reactivity according to the operating conditions in real-time. However, in current work only simple step and ramp insertions were considered.

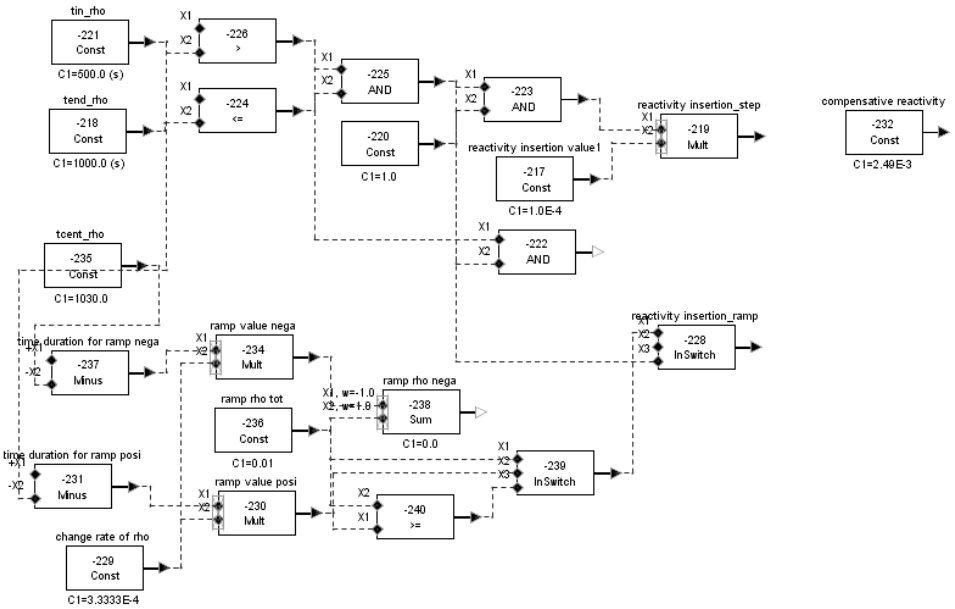


**Figure 3.16**: System for the reactivity insertions

The mathematical interpretations for the system for the step insertion of reactivity

is shown in Eq. 3.3. The $R_{step}$ is the step value to be inserted, while the $t_{init,step}$ is the time point, when the reactivity is added.

$$R(t) = \begin{cases} 0, & t < t_{init,step} \\ R_{step}, & t \geq t_{init,step} \end{cases} \tag{3.3}$$

And the system for the ramp insertion of reactivity is mathematically explained in Eq. 3.4. The $t_{init,ramp}$ and $t_{end,ramp}$ define the time period of the ramp insertion process, while the $R_{ramp,rate}$ presents the rate of the ramp insertion with the unit of pcm/s.

$$R(t) = \begin{cases} 0, & t < t_{init,ramp} \\ R_{ramp,rate}(t - t_{init,ramp}), & t_{init,ramp} \leq t \leq t_{end,ramp} \\ R_{ramp,rate}(t_{end,ramp} - t_{init,ramp}), & t_{end,ramp} < t \end{cases} \tag{3.4}$$

**System of the Pump Control**

The control system presented in Figure 3.17 is the fuel pump controller consisting of three sub-systems, which can perform three types of pump behaviors respectively. The first one was built for the steady-state operation. This part gives the pump an initialization time, which means the pump flow rate starts from zero and increases in a ramp way until it reaches the nominal value. The advantage of doing this is to avoid the convergence failure sometimes occurring during the initialization of TRACE. The second sub-system is used to perform the pump transient simulation, which means the nominal pump flow rate will be changed to another value in a ramp way in order to study the system responses to the flow rate fluctuation. The third sub-system is used to simulate the pump failure or the plant blackout. Particularly, the pump flow rate during the shutdown process is calculated through an exponential function with a constant time factor, which can control the speed of the shutdown process. On the other hand, the structure of the coolant pump controller is basically the same as the fuel pump controller but with different controlling parameters.

The pump control system can be presented with three mathematical expressions separately. The steady-state control system was explained in Eq. 3.5, where $\dot{m}_{rate1}$ is the increasing rate of the mass flux and $\dot{m}_{nominal}$ is the nominal pump flow rate.

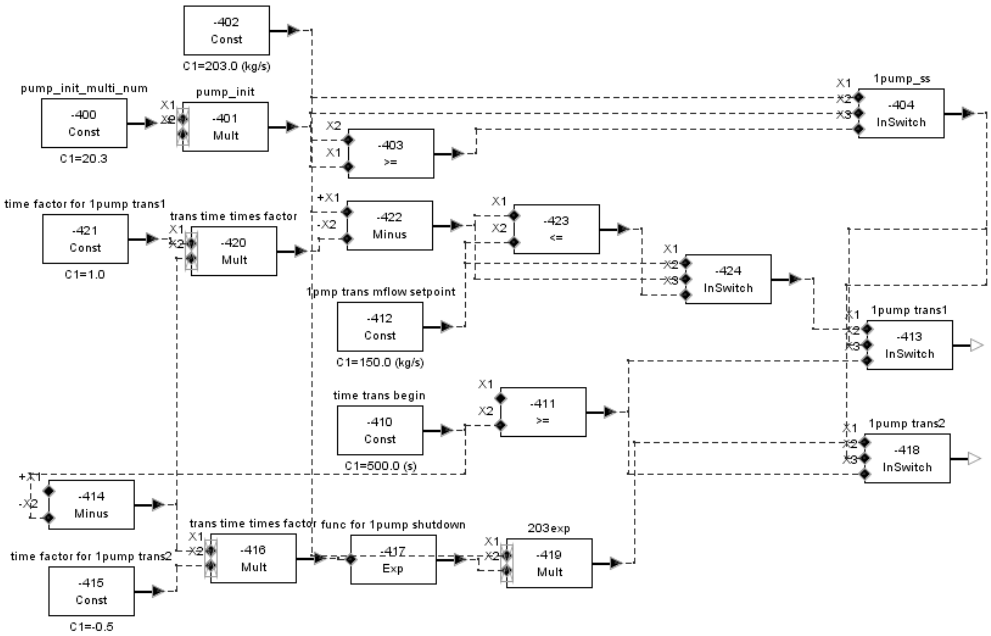


**Figure 3.17**: System for the pump control

$$\dot{m}(t) = \begin{cases} \dot{m}_{rate1} \cdot t, & t > 0 \\ \dot{m}_{nominal}, & \text{when } \dot{m}_{rate1} \cdot t = \dot{m}_{nominal} \end{cases} \tag{3.5}$$

The pump transient controller was explained in Eq. 3.6, where $t_{init,pt}$ and $t_{end,pt}$ define the time period of the pump transient. The $\dot{m}_{rate2}$ presents the change rate of the mass flux during the transient, while the $\dot{m}_{new}$ sets the new steady-state flow rate of the pump.

$$\dot{m}(t) = \begin{cases} \dot{m}_{nominal}, & t < t_{init,pt} \\ \dot{m}_{rate2} \cdot (t - t_{init,pt}), & t_{init,pt} \leq t \leq t_{end,pt} \\ \dot{m}_{new}, & t_{end,pt} < t \end{cases} \tag{3.6}$$

The pump failure controller was explained in Eq. 3.7, where $t_{init,ps}$ defines when the pump failure occurs and the time factor $a_t$ controls the speed of the pump shutdown.

$$\dot{m}(t) = \begin{cases} \dot{m}_{nominal}, & t < t_{init,ps} \\ \dot{m}_{nominal} \cdot exp(-a_t(t - t_{init,ps})), & t_{init,ps} \leq t \end{cases} \tag{3.7}$$

**System of the Power Initialization**

Similar to the reason of building the steady-state controller for the pumps, the power initialization controller make the energy deposition increase relative smoothly instead of reaching the nominal power at $t = 0s$. As said, for one thing this approach can help to prevent the calculation from the iteration failure, for another the large power oscillations at the beginning can be avoided.

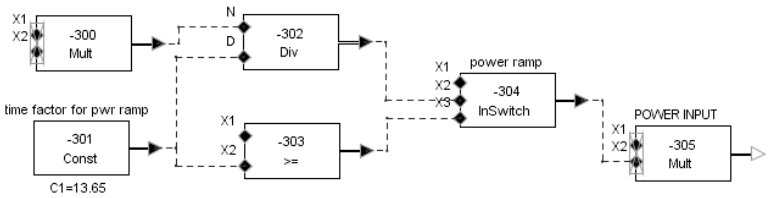


**Figure 3.18**: System for the power initialization

The mathematical interpretation for this system can be found in Eq. 3.8. Principally the selection of the power increasing rate $P_{rate}$ is flexible. A smaller rate can reduce the initial power oscillation, but it takes a longer time to reach the steady state and vice versa.

$$P(t) = \begin{cases} P_{rate} \cdot t, & t > 0 \\ P_{nominal}, & \text{when } P_{rate} \cdot t = P_{nominal} \end{cases} \tag{3.8}$$

**System of the Transient Time Detector**

This system gives the possibility to measure the circulating time of the fuel salt in the reactor core and in the primary loop. The measured circulating times were associated with the point-kinetic model to embed the impact from the flow velocity of the fuel salt. To this end, the component "*Edge Signal*" was introduced to measure the flow velocity across the specific edge of the component, thereby the transient time of the fuel salt in the corresponding component can be determined.

Its mathematical form can be simply expressed as follows (Eq. 3.9):

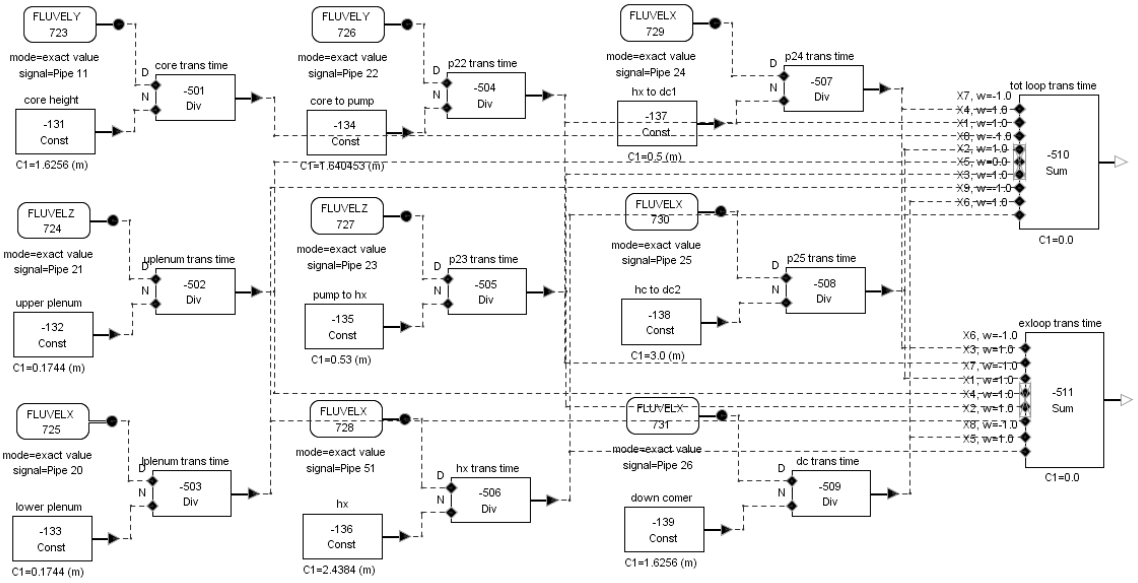


**Figure 3.19**: System for the transient time detector

$$\begin{cases} \dfrac{H_{core}}{u_{f,core}} \longrightarrow \tau_c \\ \displaystyle\sum_{n=1}^{N} \frac{L_n^{ID}}{u_{f,n}^{ID}} \longrightarrow \tau_l \end{cases} \tag{3.9}$$

where $u$ means the flow velocity of the fuel salt, while $H_{core}$ means the height of the reactor core. $L^{ID}$ presents the length or the height of the component in the primary loop except the reactor core with its ID number.

Hereby the system modeling of the MSRE was completed. Furthermore, the comparison of the models between ORNL, TRACE and a recent study[25] was given in Table 3.7. It seems that the ORNL developed two models for the MSRE simulation. The simulation based on the zero-dimensional model "ORNL-2" was performed using the code "MURGATRΦYD"[26]. A more advanced model "ORNL-1" was built afterward considering like the space-dependent parameters, different fuel properties and even the poisonousness of the fission gas. The simulation for "ORNL-1" was done by another code called "ZΦRCH"[27]. Generally, the governing equations for neutron dynamics in both codes "MURGATRΦYD" and "ZΦRCH" were derived

**Table 3.7**: Comparison of the reference models

| | ORNL-1(Fuel B/C) | ORNL-2 | Study[25] | TRACE |
|---|---|---|---|---|
| core regions | 9 | 1 | 10/100 | 10 |
| axial power distribution | yes | no | yes | no |
| radial power distribution | yes | no | no | no |
| axial temp. distribution | yes | no | yes | yes |
| radial temp. distribution | yes | no | no | no |
| fuel heat capacity [J/(kg·K)] | 2082/2146 | 1958 | 1930 | 1884 |
| coolant heat capacity [J/(kg·K)] | 2219 | – | 2390 | 2386 |
| temp. coeff. of fuel [pcm/K] | -8.946/-5.904 | -5.04 | -8.71 | -8.71 |
| temp. coeff. of coolant [pcm/K] | -8.838/-6.624 | -10.8 | -6.66 | -6.66 |
| neutron generation time [$10^{-4}$s] | 3.47/2.4 | 2.9 | 2.4 | 2.4 |
| number of groups | 6 | 6 | 6 | 6 |
| precursor circulating | yes | yes | yes | yes |
| fluid transport lags | yes | yes | yes | yes |
| fluid-to-pipe heat transfer | yes | no | no | no |
| xenon poisonousness | yes | no | no | no |

from the point-kinetic equations. Besides, another recent study[25] on the MSRE system was also taken as a reference case, which did the modeling and simulations with MATLAB® Simulink® basically in 1D.

# Chapter 4

# Simulation Results and Analysis of MSRE System with TRACE

## 4.1 Steady State Simulation

To implement a steady state simulation is a very crucial step to check the TRACE model before doing the transient simulation. For the steady-state simulation following notes were given. As mentioned in the previous chapter, the mass flow rates of the pumps and the reactor power were controlled to be increased smoothly until they reached their nominal values during the initialization. On the other hand, the boundary condition of the entire MSRE system is the inlet temperature and the mass flux of the cooling air at the radiator. As the entrance temperature was fixed, the mass flow rate of the air has been finely tuned, so that the power production in the reactor core can be exactly 10MW. The result of the stationary simulation was presented in Table 4.1, where the TRACE result has generally a good agreement with the MSRE's design parameters.

However, among those data the $\Delta T_{log}$ and the overall heat transfer coefficient at the heat exchanger seem to have relative large errors. This can be mainly explained by the simplification of the radiator model described in Figure 3.12. In particular, the one-dimensional TRACE limits the users to build a heat exchanger with the cross-flow structure, which generally can have more effective heat transfer than the devices with the counter-flow structure. Therefore, with the same inlet boundary condition of the cooling air and the same thermal load of the radiator, the coolant salt can be less cooled resulting in higher operating temperature compared with the real MSRE system. Consequently, the logarithmic mean temperature difference

**Table 4.1**: Comparison of simulation results for the steady state

| | unit | ORNL | TRACE | error(%) |
|---|---|---|---|---|
| thermal power | MW | 10 | 10.000152 | 0.000152 |
| fuel outlet temperature | K | 935 | 933.42 | 0.17 |
| fuel inlet temperature | K | 908 | 907.28 | 0.079 |
| fuel mean temperature | K | 921.48 | 921.66 | 0.019 |
| fuel mass flow rate | kg/s | 203 | 202.75 | 0.12 |
| coolant outlet temperature | K | 867 | 873.92 | 0.80 |
| coolant inlet temperature | K | 825 | 834.84 | 1.19 |
| coolant mass flow rate | kg/s | 107.26 | 107.56 | 0.28 |
| air outlet temperature | K | 423 | 424.78 | 0.42 |
| air inlet temperature | K | 311 | 311 | – |
| air mass flow rate | kg/s | 89.37 | 86.64 | 3.05 |
| $\Delta T_{log}$ at heat exchanger | K | 75.25 | 65.76 | 12.61 |
| overall heat transfer coeff. at heat exchanger | W/(m$^2$·K) | 6246.09 | 7148.00 | 14.44 |
| $\Delta T_{log}$ at radiator | K | 475.4 | 482.46 | 1.49 |
| overall heat transfer coeff. at radiator | W/(m$^2$·K) | 332.18 | 315.63 | 4.98 |

($\Delta T_{log}$) at the heat exchanger decreased, which in turn produced a larger overall heat transfer coefficient with the same thermal output.

Additionally, another interesting phenomenon during the steady-state operation should be mentioned: the "Poppendiek Effect" [30]. This effect means the fuel temperature near the wall of the graphite channel is always higher than the fuel temperature in the center of the channel at the same axial position. The reason for this unconventional situation is that the temperature of the graphite stringer is higher than the adjacent fuel temperature in any axial position, which is originally caused by the power generation inside the graphite by radioactive heating. Although this heat generation from the graphite blocks (around 5% of the total power) was not taken into account for the current study, it is still worth discussing it for the point view of the reactor safety, because empirically the nuclear fuel should be the material with the highest temperature in the MSR instead. To this end a 3D 4-channel model was built and simulated with ANSYS CFX v14.5. The power profile was defined to have a cosine distribution and the graphite power had the same distribution but proportionally reduced to 5% of the total power. As presented in Figure 4.3, with a small amount of power generation the graphite became hotter than the fuel salt thus it heated up the fuel salt near the interface. Moreover, a very similar axial power profile was also obtained by ANSYS simulation (Figure 4.4) compared with the ORNL's result.

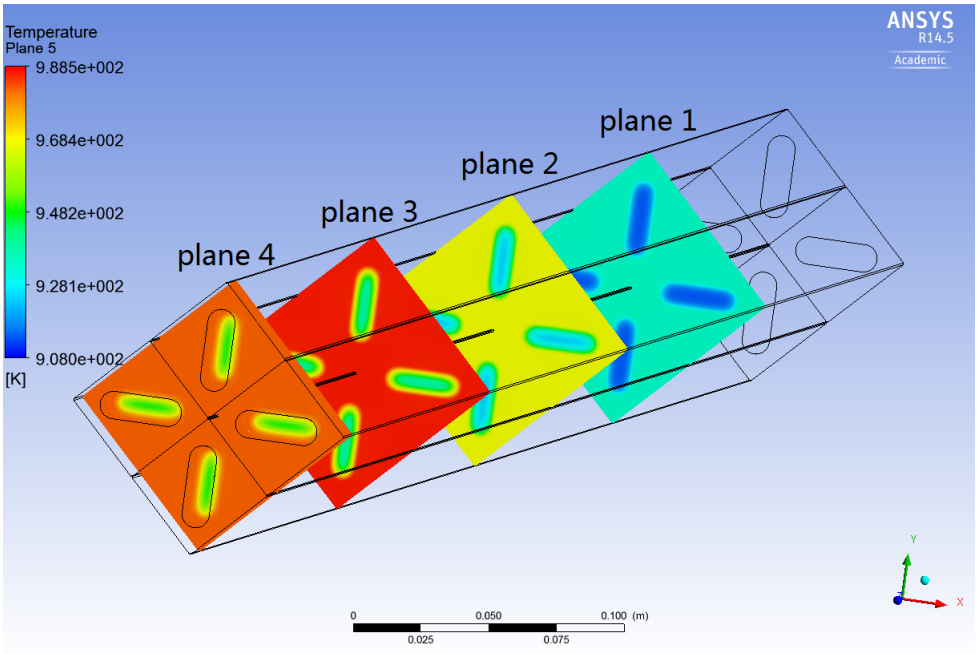


**Figure 4.1**: Temperature distribution in different planes of the fuel channels and graphite blocks

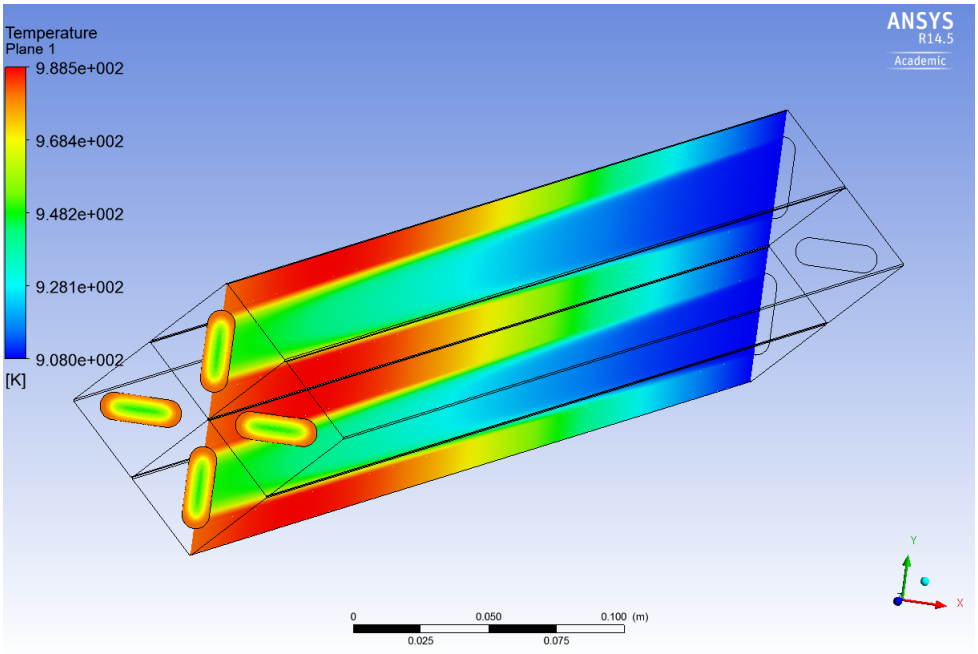


**Figure 4.2**: Temperature distribution in axial direction of the fuel channels

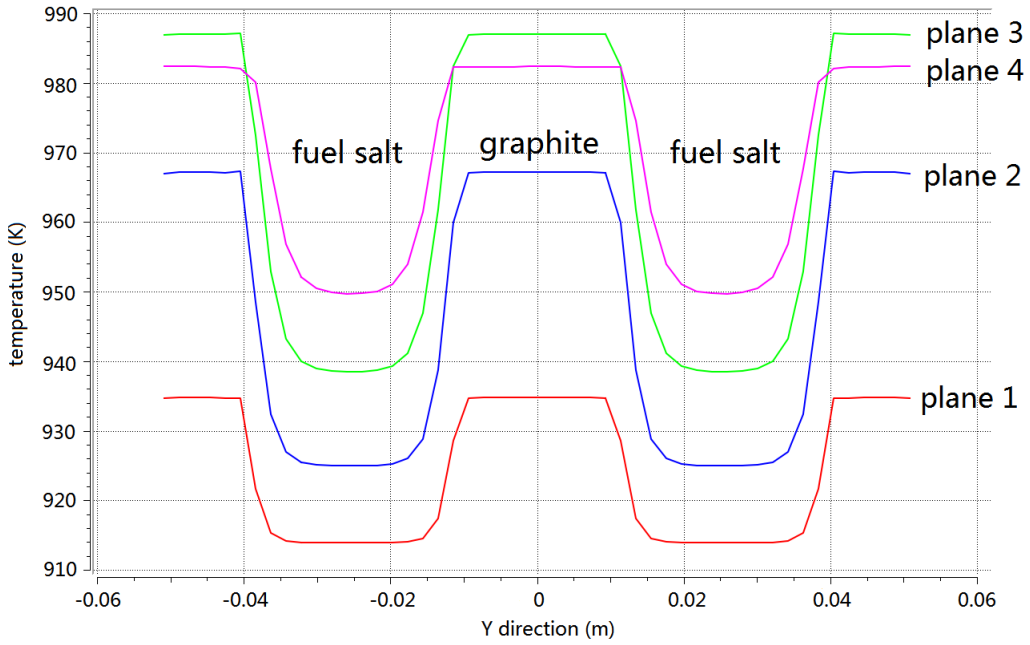


**Figure 4.3**: Temperature profiles in different planes (Figure 4.1) across the fuel channels and graphite stringers

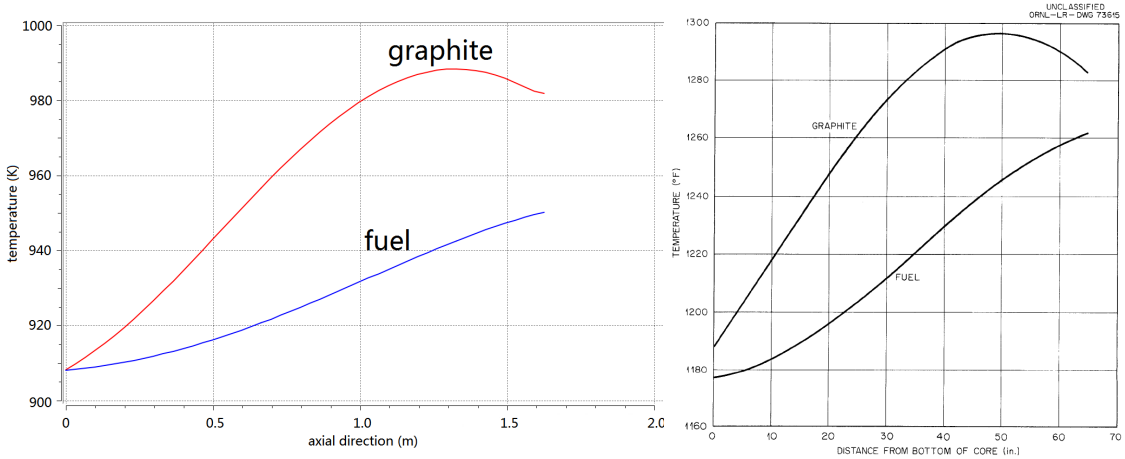


**Figure 4.4**: The axial fuel and graphite temperature profiles based on the simulation results of the ANSYS CFX model (left) and the ORNL model (right)

## 4.2 Transient and Accident Simulations

In this part several types of transient and accidental simulations were performed in order to investigate the dynamic behavior of the MSRE system. In fact these prototypic scenarios were already evaluated in the framework of the MSRE project originally, thus another important goal of this section was to reproduce the simulation results obtained by the ORNL so as to comprehensively demonstrate the MSRE TRACE model.

### 4.2.1 Reactivity Initialized Transients

#### Step Insertion of Reactivity

The first transient simulation to be done here was the 10pcm step insertion of reactivity at the power levels of 1MW and 10MW with $^{235}$U-based fuel respectively. The change of the power was evaluated based on Eq. 4.1. The comparison was carried out among the ORNL, TRACE and the recent study [25]. Figure 4.5 presented that with the step reactivity addition, a power peak appeared at the beginning as predicted and then the power decreased and finally converged to a new equilibrium due to the negative reactivity feedback caused by the temperature increasing. On the other hand, at the lower power level (1MW) the power peak became smaller, but it seems to take longer time for the MSRE system to be re-stabilized. This phenomenon was observed in all other two reference cases.

$$\Delta P(t) = P(t) - P_0 \tag{4.1}$$

Besides, another series of simulations with the step reactivity insertion was implemented. Herein 20pcm step reactivity insertion was added into the fuel circuit for the power level of 1MW, 5MW and 8MW respectively. For this time the reactor was operated with the $^{233}$U-based fuel. As a result, the power responses look similar to the previous one (Figure 4.6), but the power peak was narrowed and the reactor power seems to have a very short-lived equilibrium for the power level of 5MW or even a double-peak response for the power level of 8MW during the transient and finally the reactor power fell down to the former steady-state level approximately. One possible explanation is that the $^{233}$U-based fuel has a stronger reactivity feedback coefficient than the $^{235}$U-based fuel, which can probably increase the frequency and the amplitude of the oscillation. To this end a more convincing evidence was

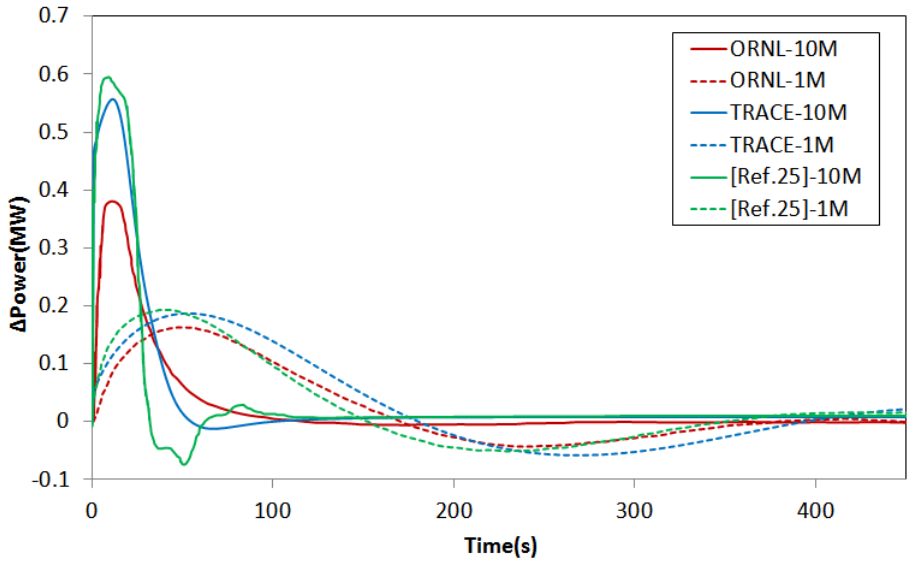


**Figure 4.5**: ΔP responses for 10pcm step reactivity insertion at 1MW and 10MW with the $^{235}$U-based fuel

presented in Figure 4.7, where the simulation was done with different fuel types but with same amount of step reactivity insertion. On the other hand, another comparison was made among the simulation results from the TRACE as well as the ORNL model and the experimental data of the MSRE. This can make some realistic sense to see the suitability of the TRACE code to simulate the MSRE's operation. Herein 19pcm step reactivity was inserted at the power level of 5MW using $^{233}$U-based fuel. Consequently, Figure 4.8 showed that the TRACE model can generally produce a result of a good agreement with the experimental data. If the absolute power was evaluated instead of the power change (ΔP(t)), the error between these two peak powers was around 3.6%, which was quite acceptable for a preliminary study.

Beside the reactivity transients done previously, it is still necessary to figure out the system responses to reactivity accidents, which for the moment means a relative large amount of step insertion. For this purpose the step additions of reactivity with -800pcm and 600pcm were taken into account in order to make comparisons to the reference study [25]. Moreover, the -800pcm step insertion simulates the scenario of the unprotected control rod insertion, while the 600pcm means the uncontrolled rod withdrawal. That is to say the velocity of the rod movement was neglected.

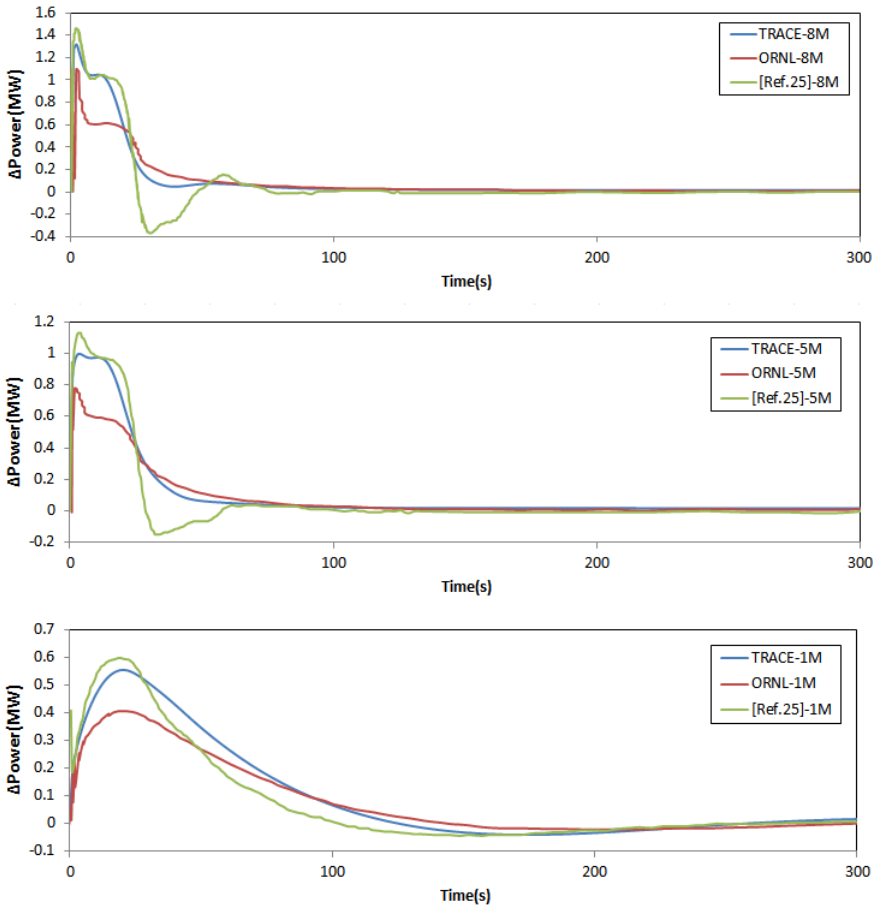


**Figure 4.6**: ΔP responses for 20pcm step reactivity insertion at 1MW, 5MW and 8MW with $^{233}$U-based fuel

During the simulation with the -800pcm step reactivity insertion, the reactor power fell down from 8MW to 0.162MW in minimum within 73s. As a result, the fuel and graphite temperatures decreased thereby storing large amount of positive reactivity inside, which was then counteracting the inserted negative reactivity and finally brought a power recovery starting at the 125s (Figure 4.9). To make it more clear, Figure 4.10 gives an overview about the evolutions of all involved reactivities. It is evident that after the insertion of the reactivity (red line) the positive feedback caused by the temperature sinks of the fuel salt and the moderator (blue and green lines) gradually increased, which then pulled back the global reactivity (black line) to the steady-state value.

On another aspect, a very sharp peak power appeared during the simulation with the 600pcm step reactivity insertion. The maximal power reached up to more than

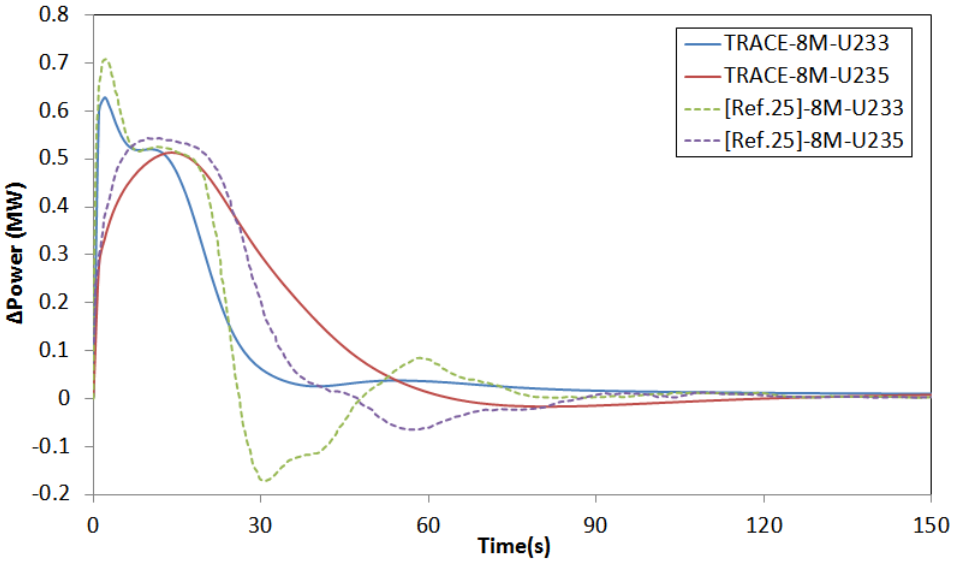


**Figure 4.7**: ΔP responses for 10pcm step reactivity insertion at 8MW for the $^{233}$U- and $^{235}$U-based fuel

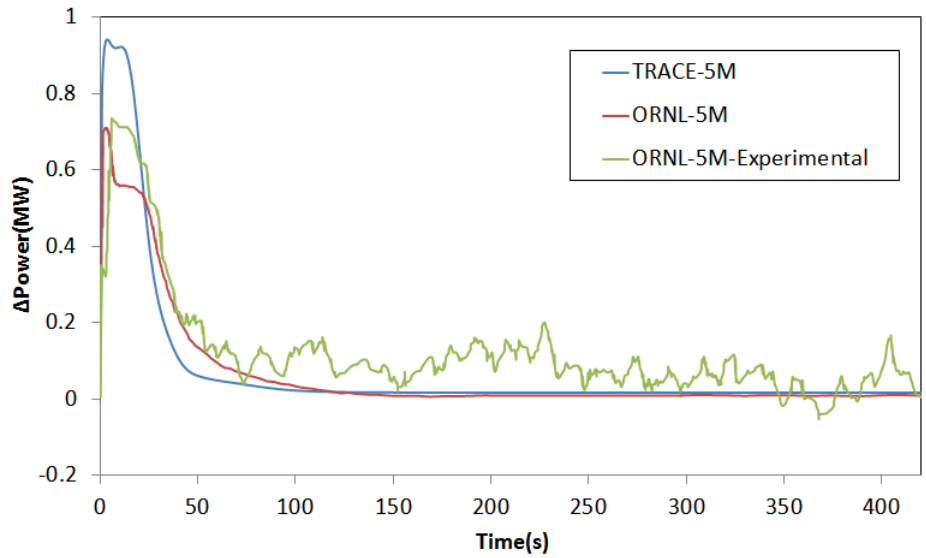


**Figure 4.8**: ΔP responses for 19pcm step reactivity insertion at 5MW for the $^{233}$U-based fuel

40 times of its nominal value, but nevertheless this process can only sustain less than two seconds thanks to the large negative feedback mainly from the rising fuel temperature (Figure 4.11). In like manner the changes of the involved reactivities were described in Figure 4.12, where it showed that the fuel feedback (red line) responded very fast and can immediately counteract the inserted reactivity (blue

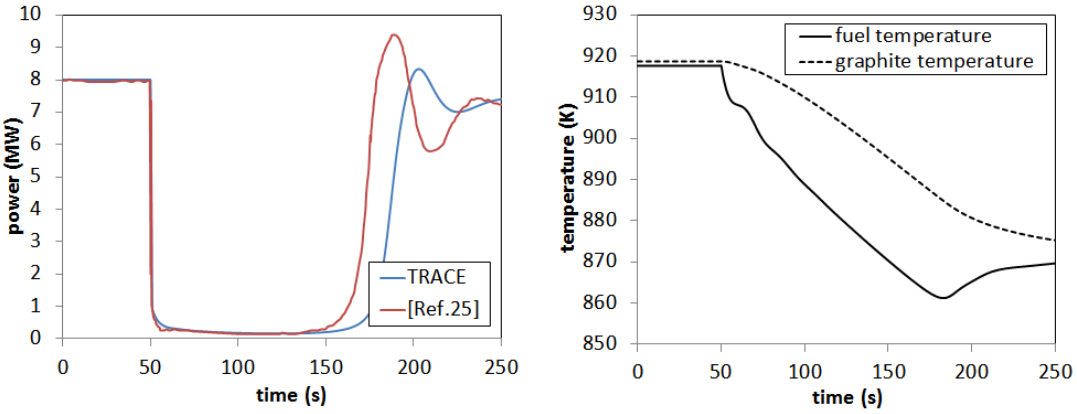


**Figure 4.9**: Power(left) and temperature(right) responses for -800pcm step reactivity insertion

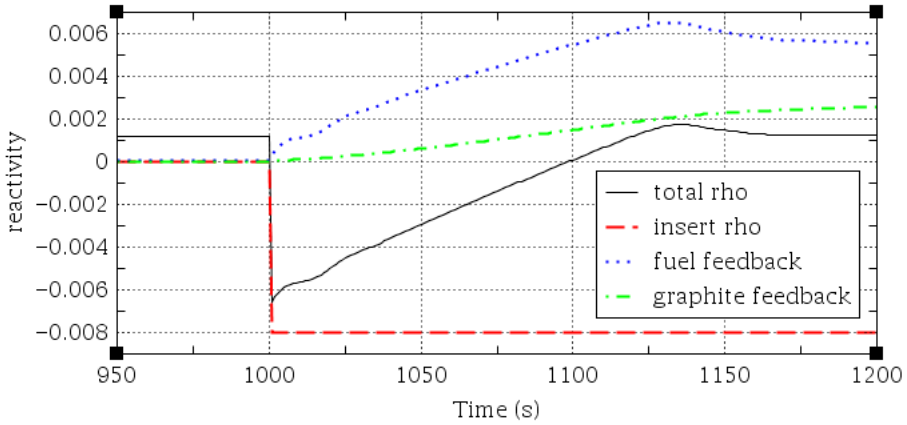


**Figure 4.10**: Reactivity responses for -800pcm step reactivity insertion

line) within two seconds, thus the global reactivity (black line) can return to its steady-state value very soon.

In fact the uncontrolled rod withdrawal accident had also been simulated by the ORNL but with more practical considerations, thus it is still necessary to show that result to make a possible comparison with the TRACE simulation. Particularly, during the normal operating two of the three control rods were fully withdrawn, while the rest one was used for shim action of reactivity. The control rod drops by the gravity with a maximal acceleration of 3.66 $m/s^2$ and it takes totally about 1 second for the whole rod to fall down including 0.1s response time. For the current scenario, the ORNL implemented it after the reactor shutdown by fully inserting all the control rods. Then the system returned to criticality again but with a very low

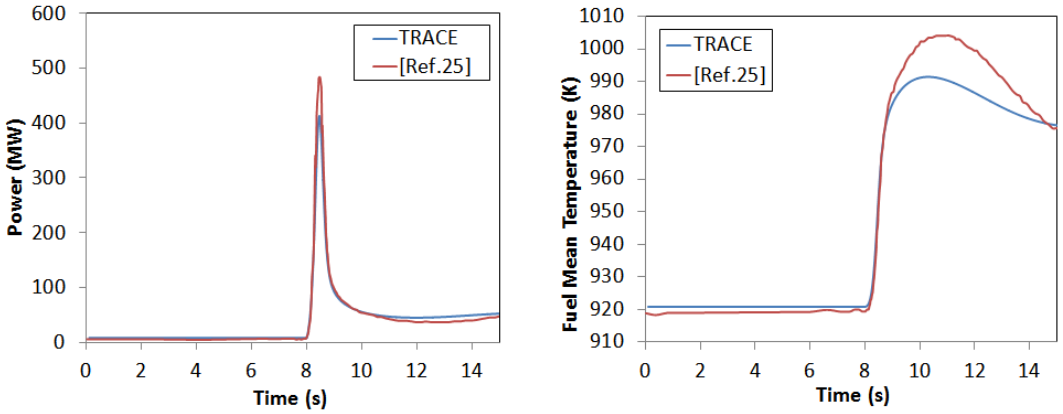


**Figure 4.11**: Power(left) and temperature(right) responses for 600pcm step reactivity insertion

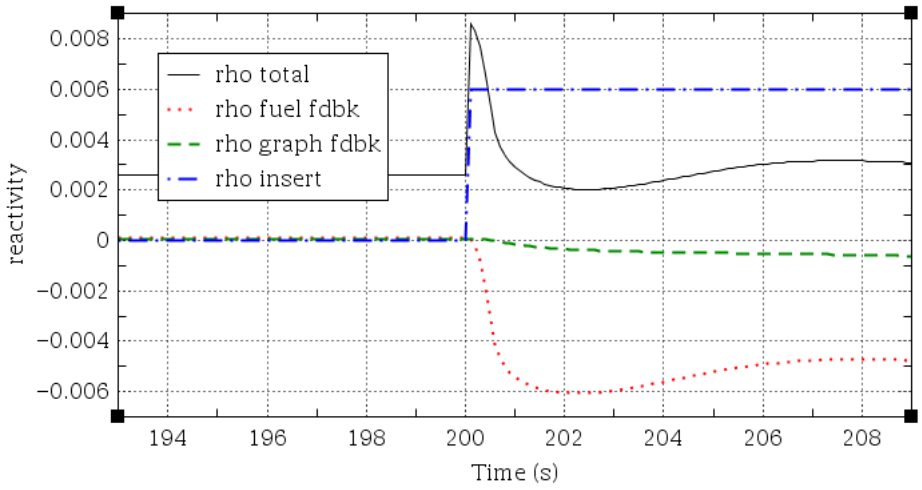


**Figure 4.12**: Reactivity responses for 600pcm step reactivity insertion

power level of only about 0.002W and this was the initial condition of the simulation. Moreover, the rate of the reactivity addition by the rod withdraw was limited under 0.08% $\delta$k/k or 0.1% $\delta$k/k separately regarding different fuel types. Therefore, now it is clear that the main differences of the simulation condition between TRACE and ORNL are: much lower initial power level and fast ramp insertion instead of step insertion. The result was illustrated in Figure 4.13(left). Finally, according to the safety criterion of the MSRE, the three control rods fall down, when the power exceeds 15MW or the outlet temperature of the fuel salt is higher than 1300°F(978K). Based on this, the results of the simulation for the uncontrolled rod withdrawal with corrective action were described in Fig. 4.13(right).

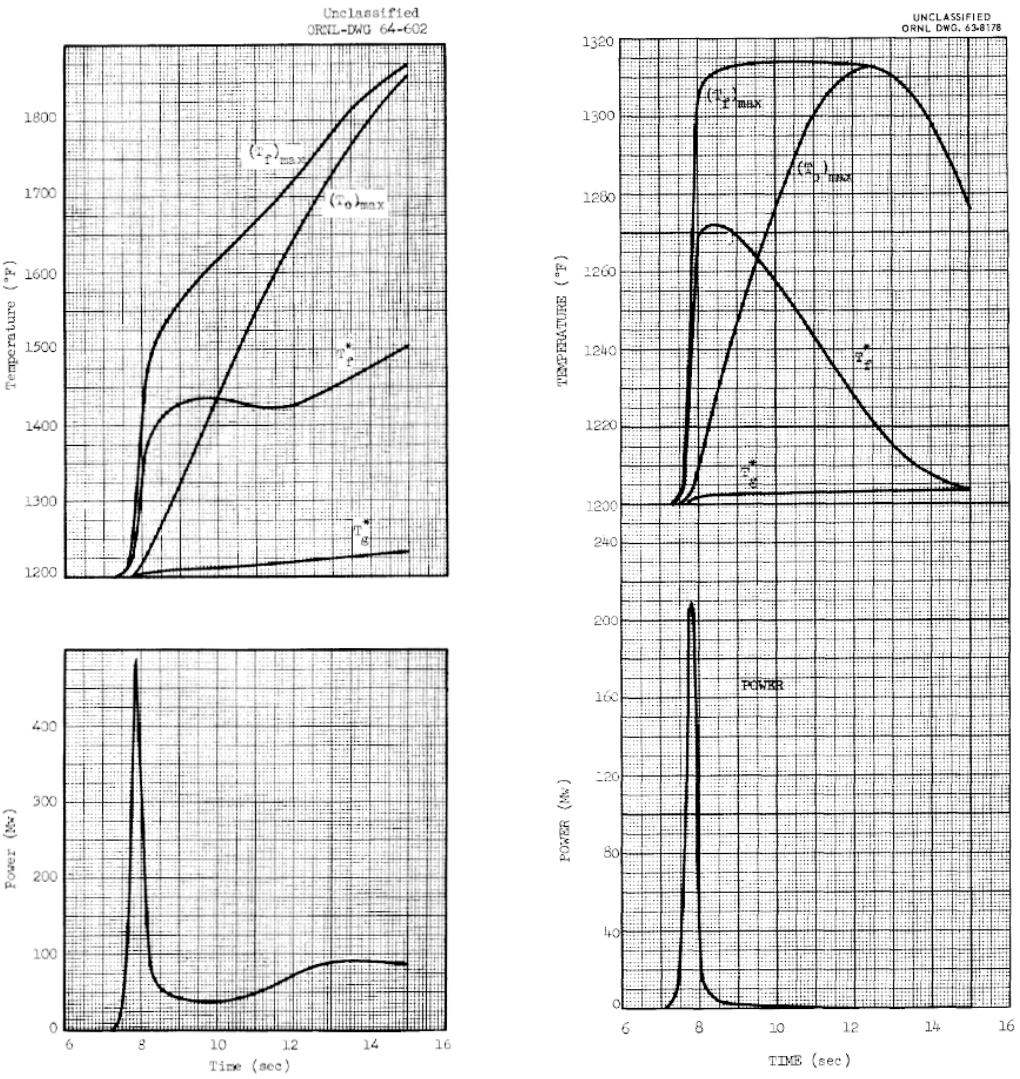


**Figure 4.13**: MSRE system response of uncontrolled rod withdrawal based-on ORNL report[29] (left: without corrective action, right: with corrective action)

### Ramp Insertion of Reactivity

In this part the system responses to the linear ramp insertion of reactivity were studied. According to the ORNL's report [31] about this transient type, it seems that they did the simulations with other specific neutron properties and feedback coefficients both for the fuel and the moderator. Hence, the point-kinetic parameters in TRACE were updated, which means the feedback coefficient was changed to -5.04pcm/K for the fuel salt and -10.8pcm/K for the moderator. Moreover, the previously used neutron generation time was replace by 2.9E-4s. The ramp transients to be evaluated were listed and named in Table 4.2.

**Table 4.2**: Transients with linear ramp insertions of reactivity

| ramp index | total reactivity (pcm) | rate of reactivity insertion (pcm/s) | duration (s) | power level (MW) |
|---|---|---|---|---|
| RAMP1 | 1000 | 33.33 | 30 | 10 |
| RAMP2 | 1000 | 100 | 10 | 10 |
| RAMP3 | 1500 | 150 | 10 | 10 |
| RAMP4 | 2000 | 200 | 10 | 10 |

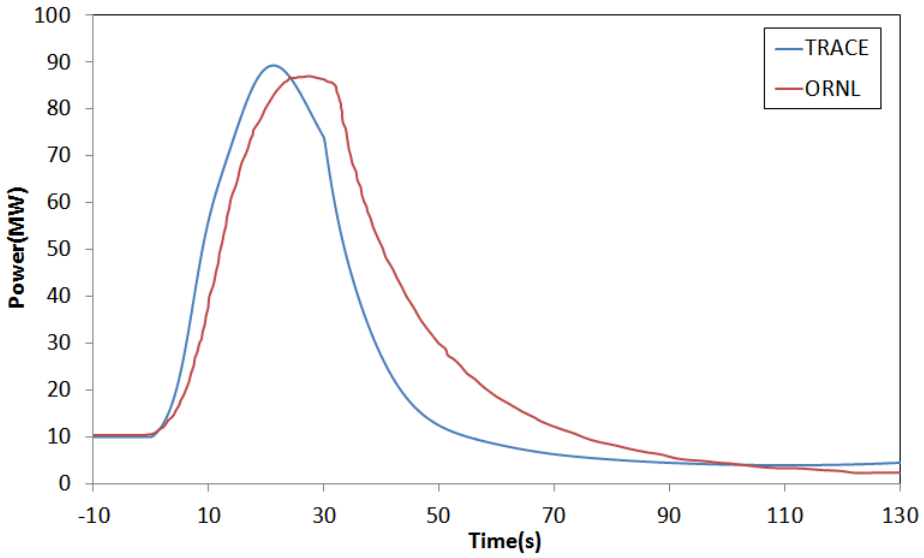


**Figure 4.14**: The power responses to the RAMP1 transient

As presented in Figure 4.14 and Figure 4.15, the reactor power rose quickly after the ramp was inserted, however, the power began to decrease before the ramp ended. This can be partly explained by the fact that the increasing fuel temperature produced a negative feedback on power and gradually counteracted the previously added reactivity until the time point, when the excessive reactivity cannot sustain the reactor at the current power level any more.

On the other hand, the power showed a double-peak responses during the RAMP2, RAMP3 and RAMP4 transients (Figure 4.16). Likewise, through the system reactivity responses this "double-peak" can be partly explained as follows. Looking at Figure 4.18, the first peak came up because of the increasing global reactivity. Then with the growing negative feedbacks from the fuel and the moderator, the global reactivity apparently found a sort of new equilibrium, however, the reactivity excess

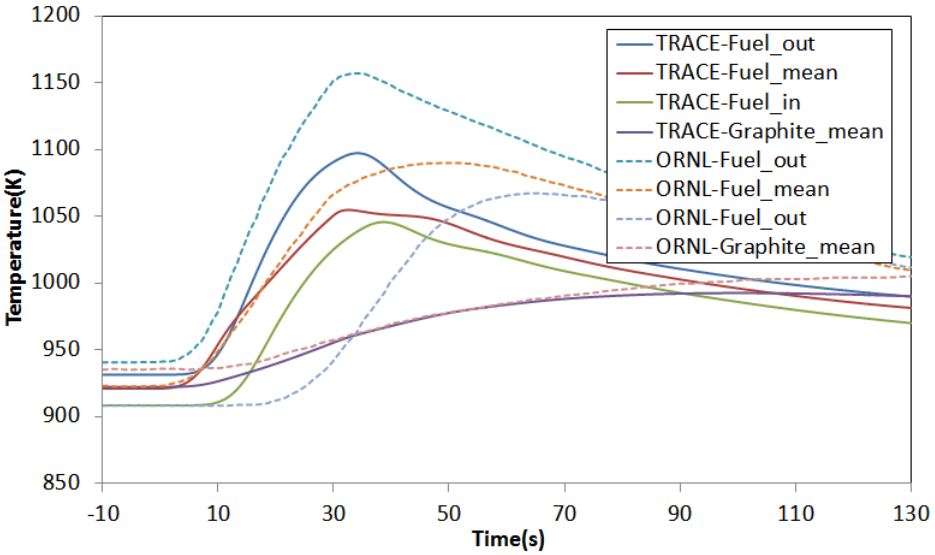


**Figure 4.15**: The temperature responses to the RAMP1 transient

at that moment was still significantly larger than the initial one, which brought about a power rise for a second time. In the end due to the thermal inertia of the working fluid, the negative reactivity from the fuel was still growing and finally was released to the system to pull back the power.

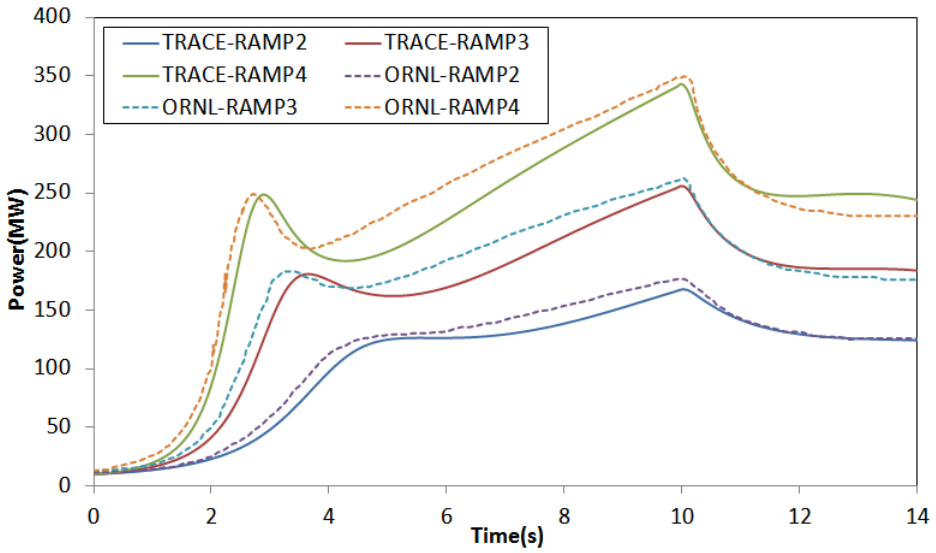


**Figure 4.16**: The power responses to the RAMP2, RAMP3 and RAMP4 transient

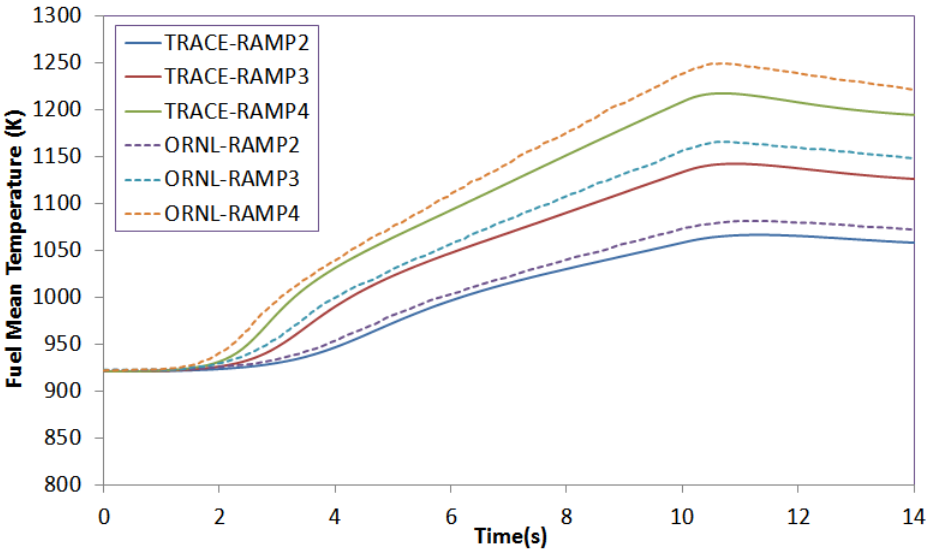


**Figure 4.17**: The fuel mean temperature responses to the RAMP2, RAMP3 and RAMP transient

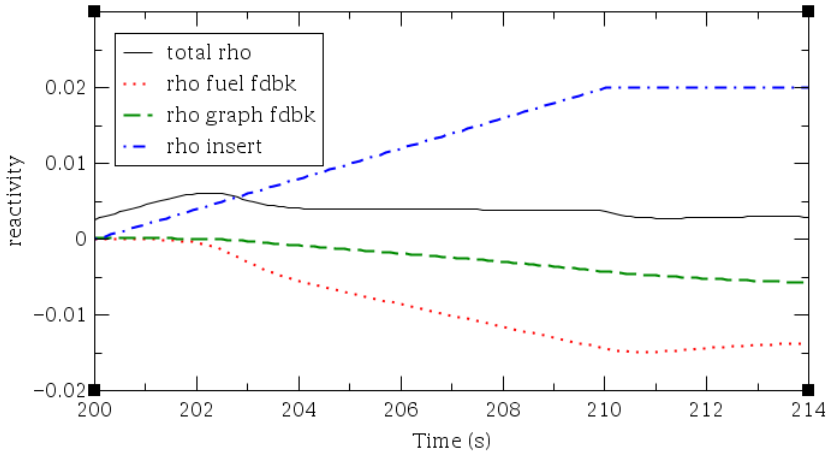


**Figure 4.18**: Reactivity responses for the RAMP4 transient

### 4.2.2 Primary Pump Failure Accident

The simulation of the primary pump failure accident is crucially important for the reactor safety analysis. For this purpose, two types of scenarios were assessed, namely the pump failure without or with the corrective actions. Before performing the simulations, a limitation of the current TRACE model should be announced. As stated in *Chapter 2*, the new ODE-solver was built with the "Control Blocks" and the velocity-dependent rate of the precursor loss and re-entering as well as the velocity-dependent decay were taken into account. Among those blocks the block "Delay"

was used to calculate the item $C_i(t-\tau_l)$ in Eq. 2.3. However, the current TRACE code is only capable to define a constant time-delay for this block, which particularly means due to this limitation the precursors will return to the reactor core within the same time as the normal operation even during the pump failure simulation. Despite this limitation, it is nevertheless still worth performing such simulation, because the consequence of neglecting the velocity-dependent time-delay for the fuel circulating is probably to produce a relative fast power response as predicted. Moreover, during the pump shutdown the core transient time ($\tau_c$) becomes very large in a very short time possibly resulting in the negligible influences from the item $\frac{C_i(t)}{\tau_c}$ (precursor loss rate) and $\frac{C_i(t-\tau_l)}{\tau_c}e^{-\lambda_i\tau_l}$ (precursor re-entering rate) in Eq. 2.3. In order to compare with the results from the ORNL model and another reference study [25], the same derivation of the transient mass flow was introduced in the following equations (Eq. 4.2):

$$\dot{m}(t) = \begin{cases} \dot{m}_{nominal}; & t < t_{init,ps} \\ \dot{m}_{nominal} \cdot exp(-a_t(t - t_{init,ps})); & t \geq t_{init,ps} \end{cases} \tag{4.2}$$

where $a_t$ is the time factor set to be 0.5 for ORNL model or 0.4 for the reference study [25].

According to the simulation results obtained by TRACE, the power fell down to less than 10% of the its nominal value within 100s due to the large negative reactivity feedback from the fuel salt. The fuel mean temperature was increased rapidly at the beginning and reached its peak value at the 57s, which was approximately 80K higher than the nominal value. In general, the TRACE simulation can obtain a comparable result with the ORNL. To the recent study [25] TRACE showed a very good agreement in the power responses, because probably the TRACE model is more similar to this study.

On the other hand, a small peak power appeared after the pump coast-down during the simulation but only with $^{235}$U-based fuel. This phenomenon can be explained by two reasons, which are related to the system layout of the primary loop and the fuel property. First, the fuel pump was located at the highest position of the primary

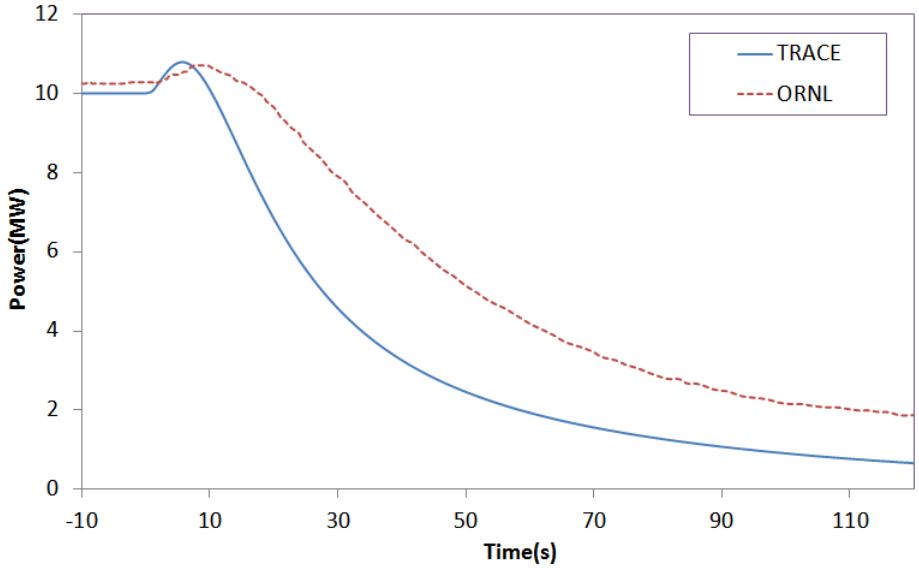


**Figure 4.19**: Power responses to the primary pump failure accident based on the TRACE and ORNL simulation results with $^{235}$U-fuel

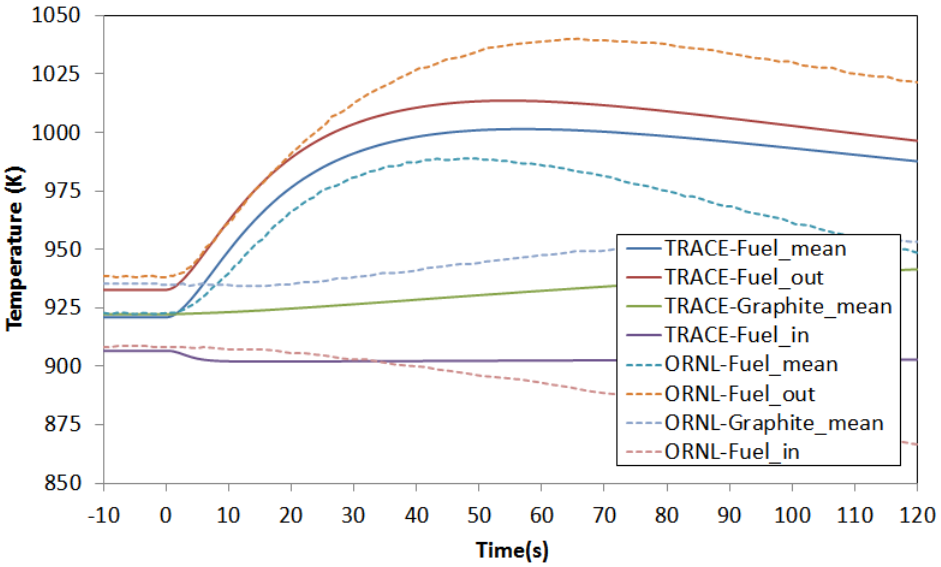


**Figure 4.20**: Temperature responses to the primary pump failure accident based on the TRACE and ORNL simulation results with $^{235}$U-fuel

loop and its inlet was connected to the outlet of the reactor core, while its outlet was connected to the inlet of the heat exchanger. Moreover, the heat exchanger was installed with 3° slope, which means its inlet is higher than its outlet in elevation. Finally, the reactor vessel was installed lower than the fuel pump and the heat exchanger. This system layout led to the result that the fuel salt inside the reactor

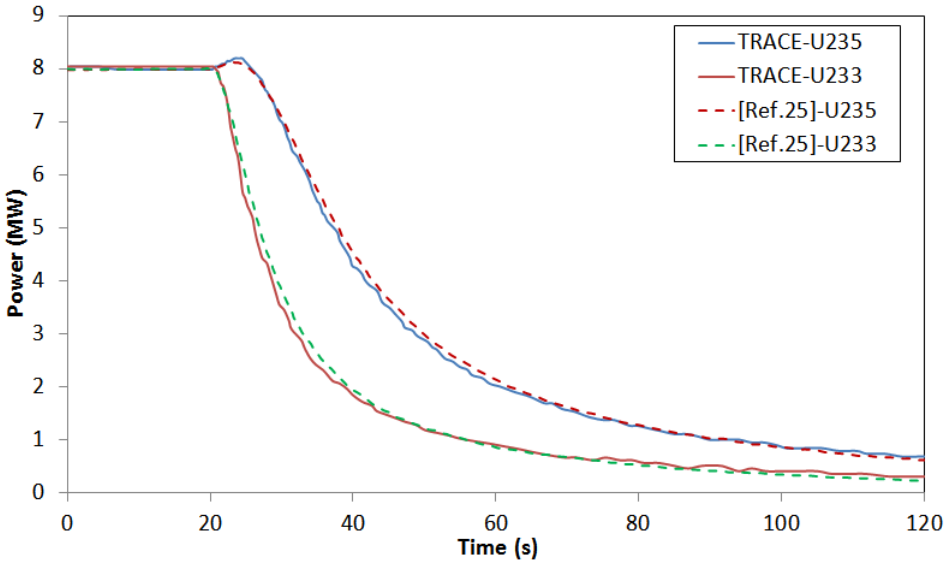


**Figure 4.21**: Power responses to the primary pump failure accident based on the TRACE and reference [25] simulation results with $^{235}$U- and $^{233}$U-fuel

core stopped flowing during the pump shutdown accident, but the fuel salt held in the heat exchanger was still being discharged back to the reactor core by gravity for a short period. Consequently, the amount of the precursors within the reactor core was temporarily increased thus leading to that power rise at the beginning. Table 4.3 listed the time-dependent mass flux of the fuel at the core entrance and exit, which confirmed the previous statement. In addition, Figure 4.22 offered a more intuitive evidence that the precursor concentrations inside the core were all growing up based on this reason after the pump shutdown. Second, as a result of a smaller temperature coefficient, the negative feedback of the $^{235}$U-based fuel was not sufficient to counteract this power increase. That's why this phenomenon was not observed during the simulation with $^{233}$U-based fuel (Figure 4.21).

Furthermore, the very good consistency between the TRACE and the reference study [25] implies that neglecting the velocity-dependent time-delay almost didn't impact the results but only to produce a slightly faster power response. Figure 4.23 was about the rate of the precursor loss and return, which presented sharp decreases for each group. This consequence finally verified the previous prediction.

In addition, two critical parameters were found to reach or even exceed the limits al-

**Table 4.3**: Mass flows at the reactor core inlet and outlet during the initial 15s

| time | mass flow at the core inlet (kg/s) | mass flow at the core outlet (kg/s) | difference between flow-in and flow-out |
|---|---|---|---|
| 0 | 203 | 203 | 0 |
| 1 | 125.2412 | 125.7210 | 0.4798 |
| 2 | 75.7584 | 76.5435 | 0.7851 |
| 3 | 45.8036 | 46.7890 | 0.9854 |
| 4 | 27.6800 | 28.7991 | 1.1191 |
| 5 | 16.7182 | 17.9227 | 1.2045 |
| 6 | 10.0895 | 11.3420 | 1.2526 |
| 7 | 6.0814 | 7.3529 | 1.2715 |
| 8 | 3.6582 | 4.9259 | 1.2677 |
| 9 | 2.1932 | 3.4401 | 1.2469 |
| 10 | 1.3076 | 2.5212 | 1.2136 |
| 11 | 0.7722 | 1.9437 | 1.1715 |
| 12 | 0.4483 | 1.5718 | 1.1235 |
| 13 | 0.2521 | 1.3237 | 1.0716 |
| 14 | 0.1328 | 1.1507 | 1.0179 |
| 15 | 0.0600 | 1.0237 | 0.9637 |

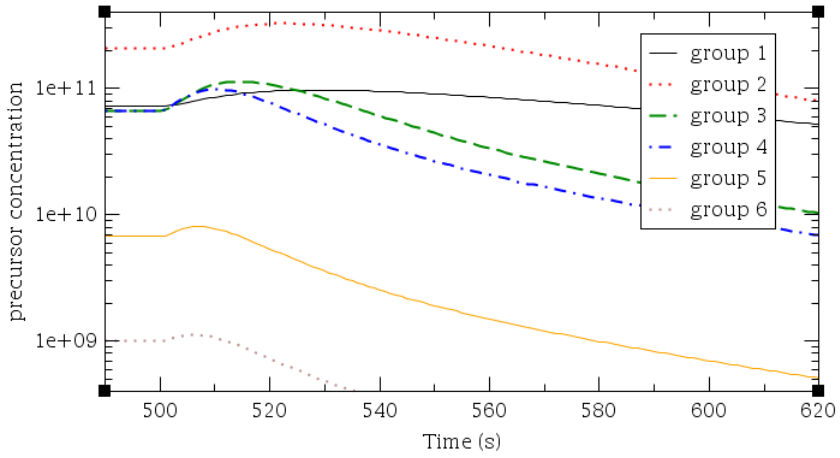


**Figure 4.22**: Change of the precursor concentrations to the primary pump failure accident based on the TRACE simulation results with $^{235}$U-fuel

lowed by the MSRE's safety criteria. One is the coolant temperature, which reached up its melting point (Figure 4.24) due to the air-cooling and another is the fuel outlet temperature, which exceeded its upper limit (978K) during the primary pump shutdown accident. To avoid this, the radiator door should be closed immediately after the pump shutdown and simultaneously the control rods have to be inserted with a speed of 0.01m/s giving a negative ramp reactivity of -75pcm/s on power. The updated results were described in Figure 4.25 and Figure 4.26. Consequently, the reactor was shut down within a shorter time; the fuel outlet temperature re-

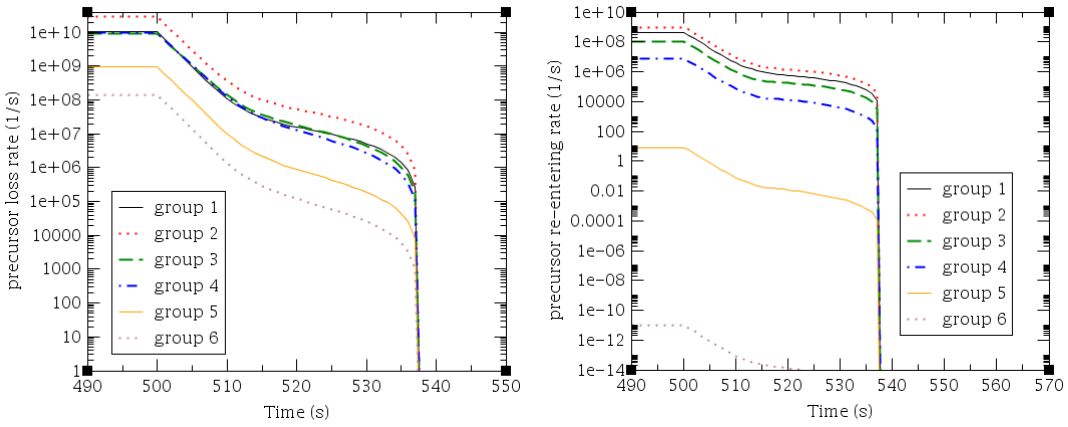


**Figure 4.23**: The rate of the precursor loss(left) and return(right) during the primary pump failure accident based on the TRACE simulation results with $^{235}$U-fuel

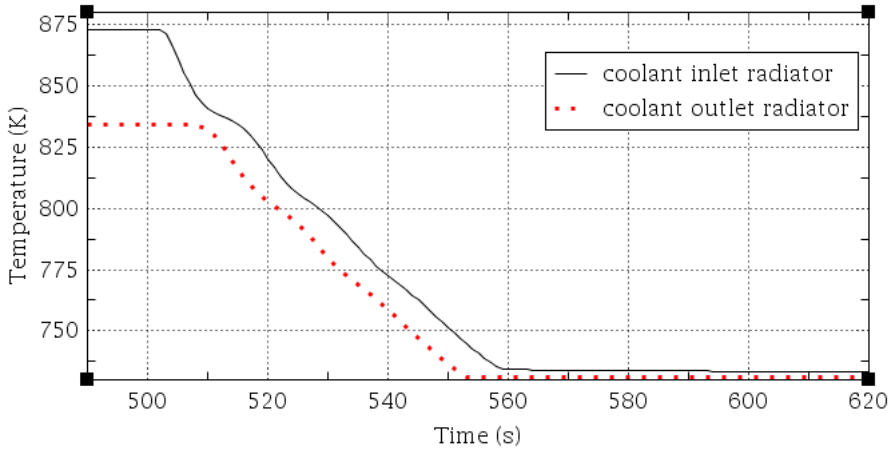


**Figure 4.24**: Coolant salt temperature response to the primary pump failure accident without corrective action based on the TRACE simulation results with $^{235}$U-fuel

mained under the upper limit with a reasonable margin and the coolant salt was not frozen any more.

## 4.3 Result Analysis

This section mainly focuses on the error analysis for the TRACE and ORNL's simulations. Generally, the mismatch occurred between these two simulations were mainly based on four model differences: the dimension effect (reactor core division), the applied numerical solver, physical properties of the working fluids and other neglected factors.

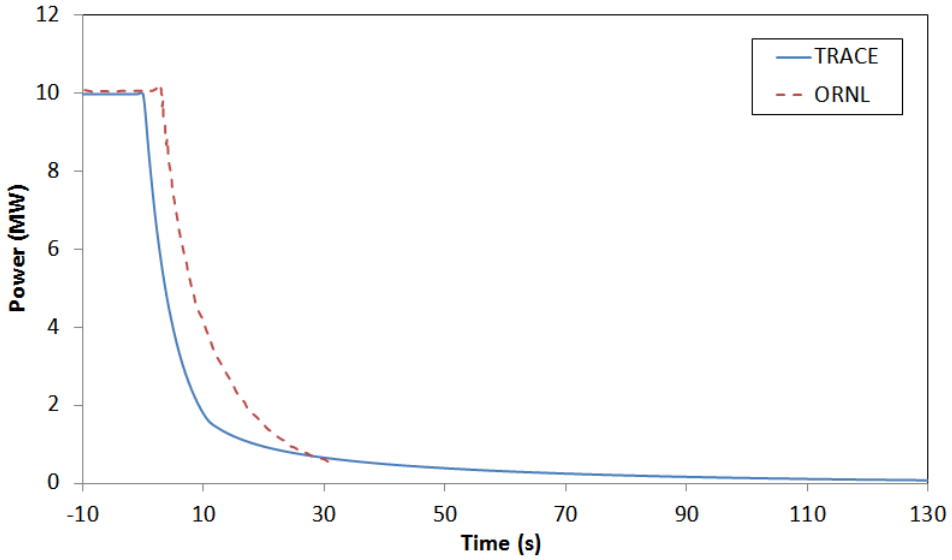


**Figure 4.25**: Power responses to the primary pump failure accident with corrective action with $^{235}$U-fuel

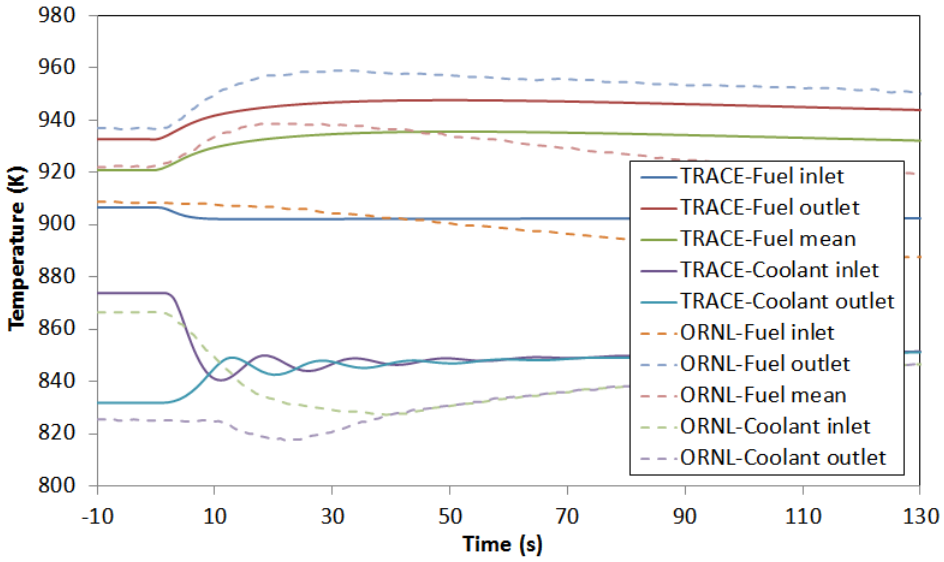


**Figure 4.26**: Temperature responses to the primary pump failure accident with corrective action with $^{235}$U-fuel

### Dimension Effect (Reactor Core Division)

This means that the reactor core models of the TRACE and the ORNL were built with different numbers of dimensions respectively. In particular, the TRACE core model consists of only one region for the neutron calculation and 10 axial nodes for

the evaluation of the temperature distribution, while the ORNL core model contains totally 9 sub-regions both in axial and radial directions to introduce the non-uniform distribution of the neutron flux, fuel and graphite temperatures and the fuel velocity (Figure 4.27). Therefore, it can be summarized like that the TRACE core model is a 0D-neutron and 1D-thermal-hydraulic model, while the ORNL model was a 2D-neutron and 2D-thermal-hydraulic model.

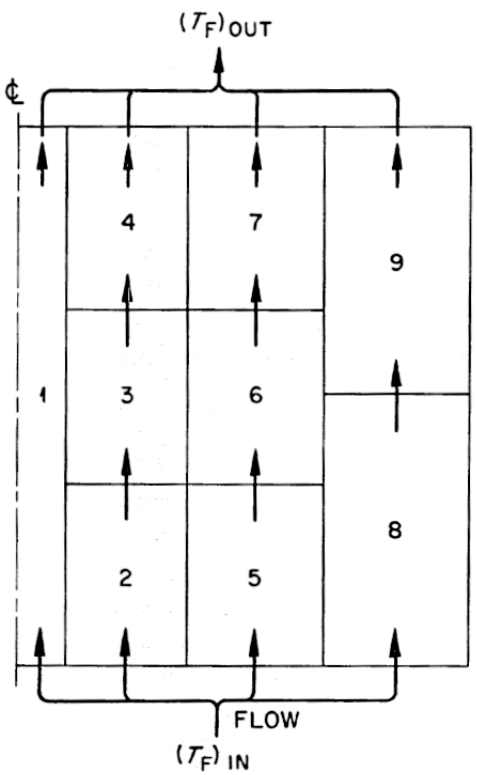


**Figure 4.27**: The reactor core division of the ORNL model

Presently it has been confirmed that the prototypic transient simulations with the step reactivity insertions implemented by the ORNL were based on this 9-region core model. Moreover, it can produce more detailed calculations when considering the position-dependent properties in the reactor core, which furthermore helps to obtain the average properties that are more precise and reasonable in values. For instance, different power levels bring about different power responses with the same amount of a step reactivity addition, which particularly means that the higher the initial power level is, the higher and sooner the peak power appeared as illustrated in Figure 4.28. Spontaneously the same situation can happen to the different locations

within a single reactor core with non-uniform power distribution. Therefore, when adding a reactivity, the averaged power response calculated from the 9 sub-regions can be imaginably distinguishing from the one-region core model. Finally, another observation from the TRACE simulation and the reference study [25] indicates that it seems to have no significant impact on the results whether the point-kinetic model has only one region or is axially divided into multi-regions.

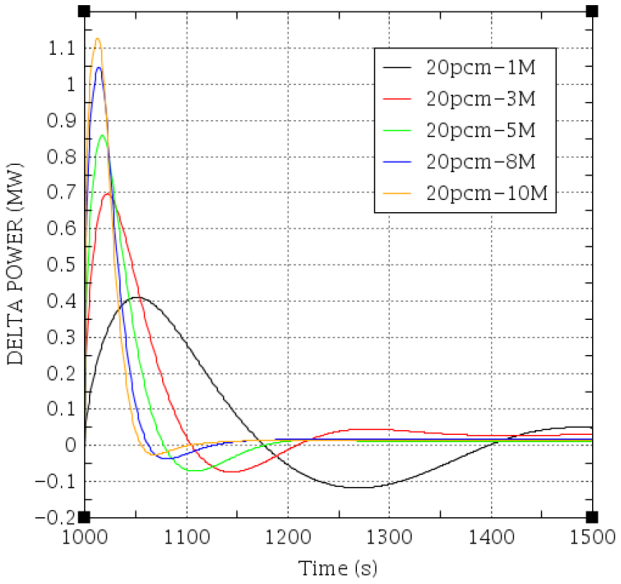


**Figure 4.28**: The power responses to different power levels

### Numerical Solver

The selected numerical solver for the current TRACE model was the forward Euler method (FEU), which is a first-order explicit method with lower computational load. The precision of the FEU method is strongly dependent upon the time step size and it inevitably causes an overestimation to a peak and an underestimation to a valley. However, according to the ORNL's reports about the safety calculation, the simulations done there were based on the 5th-order Runge-Kutta method, which undoubtedly offered a more precise result and has a better numerical stability. For instance, the ORNL implemented the simulations of the ramp reactivity insertion with the code MURGATRΦYD, which was adapted to the one-region point-kinetic model like TRACE. Thus the discrepancies observed, for instance, in Figure 4.14 and Figure 4.16, can be partly explained by the different precision of the applied

numerical solvers.

### Physical Properties of the Working Fluids

It seems that the physical properties of the fuel and coolant salts were often being updated for years during the MSRE project, which means that the reference simulations were performed with several different fluid properties. Among those properties the heat capacity can be a critical parameter for the system dynamics, because it matters to the thermal inertia of the fluid thus it affects the change rate of the temperature and its reactivity feedback. In present work the physical properties of the so-called "fuel type A"[29] was taken as the standard fuel and comparing to other fuel options, the "fuel type A" has a relative small specific heat, which partly caused the different transient responses between the TRACE and the ORNL simulation. For instance, during the primary pump failure, the negative reactivity feedback of the fuel with smaller heat capacity can be stronger than the fuel with the larger one. And this partly induced the faster power reduction for that scenario.

### Other Neglected Factors

Additionally, there are still other ignored factors, which can more or less influence the reactor's behavior. First, the graphite power was not taken into account in TRACE simulation, but in fact the fuel salt was heated up roughly 95% through the internal heat source from the nuclear reactions and 5% through the heat transfer from the hotter graphite stringers. This can probably cause a slight difference such as in the operating temperatures of the fuel salt. Second, the xenon poison was neglected in TRACE model, however, the ORNL counted this either in stationarity or non-stationarity and during the normal operation the xenon poison was compensated by a partly withdrawal of the control rod. This extra negative reactivity somewhat can definitely affect the reactor's dynamic behavior. Besides, except the reactivity feedback from the fuel salt and the moderator, the mass and power feedbacks were also considered in ORNL's calculation, which may cause different system responses from the TRACE model.

# Chapter 5

# Introduction and Methodologies of Study on Dual Fluid Reactor

## 5.1 Introduction of Dual Fluid Reactor

The Dual Fluid Reactor (DFR) concept belongs to the group of the Molten Salt Fast Reactors (MSFR), which are considered to be an option of minimum-waste, highly efficient and inherently safe future nuclear reactors. The Dual Fluid Reactor (DFR) is using an undiluted uranium and plutonium tri-chlorides with purified $^{37}Cl$ as the fuel and pure lead as the coolant. As the name "dual" suggests the DFR has a two-fluid heterogeneous reactor core, which means the fuel salt is flowing in the fuel tubes and thereby heats up the coolant flowing between fuel channels within the reactor core (Figure 5.1). The molten fuel salt is circulated independently of the lead coolant and is treated with a pyro-processing unit (PPU) for the fission products extraction as well as for the fuel re-freshening. The lead coolant is pumped into a heat exchanger, which has a possibility to use helium as the secondary coolant to achieve the highly efficient Brayton cycle without phase change (Figure 5.2).

The reference DFR design has a 3000MW thermal output (DFR-3000) with an efficiency above 50% for the power production. The mean operating temperature of the fuel salt reaches 1225°C and the exit temperature of the coolant is up to 1100°C giving the possibility of the co-generation, for instance, for the purpose of the desalination, hydrogen production or chemical process heat. Since the operating temperature of the DFR exceeds the tolerance of most of the currently used metal materials in reactor construction, silicon carbide (SiC) is planned as the main structural material for the reactor core. The fuel tubes are arrayed hexagonally with a

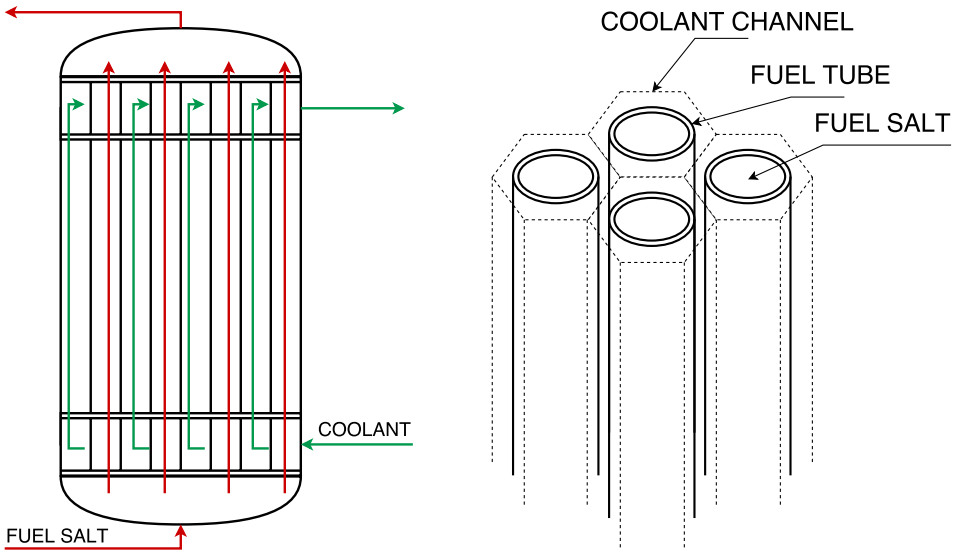


**Figure 5.1**: DFR reactor vessel and the fuel channels

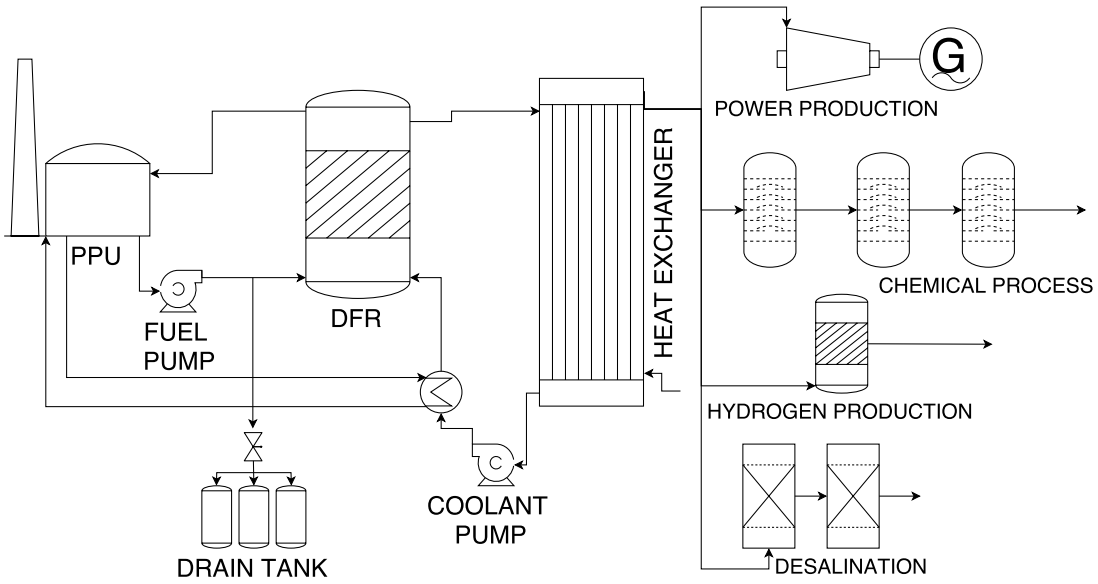


**Figure 5.2**: DFR system layout

small pitch ratio, which gives a compact structure and enhances the heat transfer efficiency within the reactor core.

In addition, three sub-critical drain tanks offering sufficient extra volume for the fuel parking during the severe accidents are connected to the reactor vessel through

a melting fuse plug. Another storage volume for the short-lived fission products is linked to the PPU, meanwhile this device is also located along the coolant circuit short away from the core entrance. In this way the residual heat from the decay of the fission products can be used for the pre-heating of the coolant.

## 5.2 Methodology

Rather than the DFR-3000 this thesis focuses on the scaled-down DFR-500 (500MW thermal output) for the purpose of demonstrating the main safety features of the DFR design. The reason for this simplification is to reduce the number of the fuel channels of the reactor but leaving the inner diameter and the thickness of the fuel tubes unchanged. Two prototype models were built in this section: first one is the 2D entire core model of the reactor for the steady-state simulation; the second one is the 1D single fuel channel model for the transient and accidental simulations. The relationship between these two models is that the steady-state simulation of the 2D entire core model provides the 1D single fuel channel model with the reasonable initial conditions for the dynamic investigations. Specifically, the steady-state simulation was performed based on the coupled-physical calculation done by the 3D Monte Carlo Code SERPENT and the quasi-2D thermal-hydraulic analysis tool developed by MATLAB. Furthermore, the study on a series of 1D single fuel channels of the DFR-500 was conducted in order to approximate the dynamic behavior of the reactor core. Each single fuel channel was considered to have only axially dependent properties, because the channel has a large length-diameter ratio (L/D=100), which means property divergence along the radial as well as the circumferential direction of the fuel tube was considered to be insignificant for the current study.

### 5.2.1 Geometry Optimization and Criticality Calculation

#### Geometry Determination

To determine the basic geometric data for the DFR-500 the following investigation was done. First, part of the geometric data and the initial conditions were taken from the DFR-3000 such as the geometry of the fuel tubes, inlet and outlet temperatures of the fuel salt and of the coolant (Table 5.1). Second, some design data was initially

assumed like the thermal output, the reactor height and the reactor core radius. Then iteration was carried out through following procedures:

**Table 5.1**: Design data for DFR-500

| parameter | value | unit |
|---|---|---|
| design data taken from DFR-3000 | | |
| fuel tube inner radius | 8.0 | mm |
| fuel tube outer radius | 10.0 | mm |
| fuel inlet temperature | 1500 | K |
| fuel outlet temperature | 1550 | K |
| coolant inlet temperature | 1173 | K |
| coolant outlet temperature | 1373 | K |
| assumed design data for DFR-500 | | |
| thermal output | 500 | MW |
| reactor core height | 2.0 | m |
| reactor core radius | 1.0 | m |
| changeable design data for iteration | | |
| pitch ratio of the fuel tube array | 1.2 | - |
| initial flow velocity of the fuel salt | 4.059 | m/s |
| calculated design data for DFR-500 | | |
| number of the fuel tubes | 6298 | - |
| overall heat transfer coefficient | 3180 | $W/(m^2 \cdot K)$ |
| initial flow velocity of the coolant | 1.592 | m/s |
| fuel inventory in the core | 4400 | kg |
| coolant inventory in the core | 22820 | kg |

**Table 5.2**: Physical properties of the fuel salt (at 1525K) and the coolant lead (at 1273K)

| name | value or behavior | unit |
|---|---|---|
| Fuel salt density | 1539 | $kg/m^3$ |
| Fuel salt specific heat | 365 | $J/(kg \cdot K)$ |
| Fuel salt thermal conductivity | 0.865 | $W/(m \cdot K)$ |
| Fuel salt viscosity | 1.319E-3 | $Pa \cdot s$ |
| Coolant density | 9812 | $kg/m^3$ |
| Coolant specific heat | 137.611 | $J/(kg \cdot K)$ |
| Coolant thermal conductivity | 23.203 | $W/(m \cdot K)$ |
| Coolant viscosity | 1.054E-3 | $Pa \cdot s$ |
| SiC thermal conductivity | 30 | $W/(m \cdot K)$ |

1. Assume a conventional pitch ratio (e.g. pitch=1.2). Basically the reasonable range for a pitch was set to be at [1.1, 1.3];

2. Calculate the physical properties of the working fluids. The temperature-dependent properties for the liquid lead were described in the reference study [74] in detail and its property data in Table 5.2 was determined by the mean value of the inlet and outlet temperatures. However, the specific data for the fuel salt ($UCl_3$-$PuCl_3$) seems hardly available yet. Therefore, in following calculations the properties of the pure $UCl_3$ replaced the properties of the salt mixture and the data was estimated and shown in Table 5.2 [75] [67].

3. The heat transfer-related parameters were determined including the number of the fuel tubes, hydraulic diameter for the coolant channel, heat transfer area and the flow velocity of the coolant (Table 5.1). The coolant velocity ($u_2$) was simply calculated by the balance between the energy input and the enthalpy change (Eq. 5.1);

$$u_2 = \frac{Q_{out}}{c_{p,2}\rho_2 A_2(T_{2,1} - T_{2,0})} \tag{5.1}$$

4. Calculate the overall heat transfer coefficient ($U_1$) through the energy conservation along the reactor core using Eq. 5.2:

$$U_1 = \frac{Q_{out}}{A \cdot \Delta T_{log}} \tag{5.2}$$

5. Calculate the velocity-dependent overall heat transfer coefficient ($U_2(u_1, u_2)$) through Eq. 5.3[56]. The coolant velocity $u_2$ was fixed previously in step 3), thus this heat transfer coefficient is actually only fuel velocity-dependent at the moment. The adapted derivations of the Nusselt number were selected for the molten salt and the liquid lead by comparing their Prandtl numbers to the corresponding applicable ranges (Eq. 5.6 and Eq. 5.8) [56] [61];

$$U_2(u_1, u_2) = \left(\frac{r_o}{r_i \alpha_1(u_1)} + \frac{r_o ln(\frac{r_o}{r_i})}{\kappa} + \frac{1}{\alpha_2(u_2)}\right)^{-1} \tag{5.3}$$

$$\alpha_1(u_1) = \frac{Nu_1(u_1)\kappa_1}{r_i} \tag{5.4}$$

$$\alpha_2(u_2) = \frac{Nu_2(u_2)\kappa_2}{D_h} \tag{5.5}$$

$$Nu_1(u_1) = \frac{\frac{\xi}{8}(Re_1(u_1) - 1000)Pr_1}{1 + 12.7\sqrt{\frac{\xi}{8}}(Pr_1^{\frac{2}{3}} - 1)} K_L \tag{5.6}$$

$$\xi = (0.79ln(Re_1(u_1)) - 1.64)^{-2} \tag{5.7}$$

$$Nu_2(u_2) = 5 + 0.025(Re_2(u_2)Pr_2)^{0.8} \tag{5.8}$$

6. Change fuel velocity to make $U_1$ and $U_2$ converge with the tolerance of $10^{-4}$. The lower limit of the fuel velocity is the critical velocity to reach the turbulent flow regime. Additionally, there is principally no upper limit for the fuel velocity, but just according to some empirical data, the fuel velocity was preliminarily confined under 5m/s. Thus if the fuel velocity has to be out of this range to get the convergence between $U_1$ and $U_2$, the pitch ratio needs to be reset and the iteration will be redone.

It makes sense to do this iteration, because once the error between the two heat transfer coefficients converge, it means that the design requirements were satisfied by the corresponding assumed design data. Specifically, $U_1$ was determined by the first law of thermodynamics. This step can be seen as a macroscopic evaluation of the entire system and propose the basic design requirement, which nevertheless has nothing to do with the specific reactor structures. Instead, $U_2$ was strongly structure-dependent, thus achieving the same value as $U_1$ means the reactor design with the corresponding structure is practically feasible at least from the point of view of the thermodynamics and heat transfer.

Additionally, the design data confirmed in Table 5.1 is of course not the exclusive solution for the DFR-500. For instance, it can happen that the error between $U_1$ and $U_2$ converge with other reasonable pitch ratio and fuel velocity, which will bring another interesting topic about the design optimization of the DFR concept. However, this evaluation needs to be coupled with the criticality calculation with various fuel compositions, which can be one of the critical works in the future. Generally speaking, the goal of the iteration done above was to create at least a reasonable

reactor structure data serving as the input data for the following investigations. The iteration approach is described in Figure 5.3.

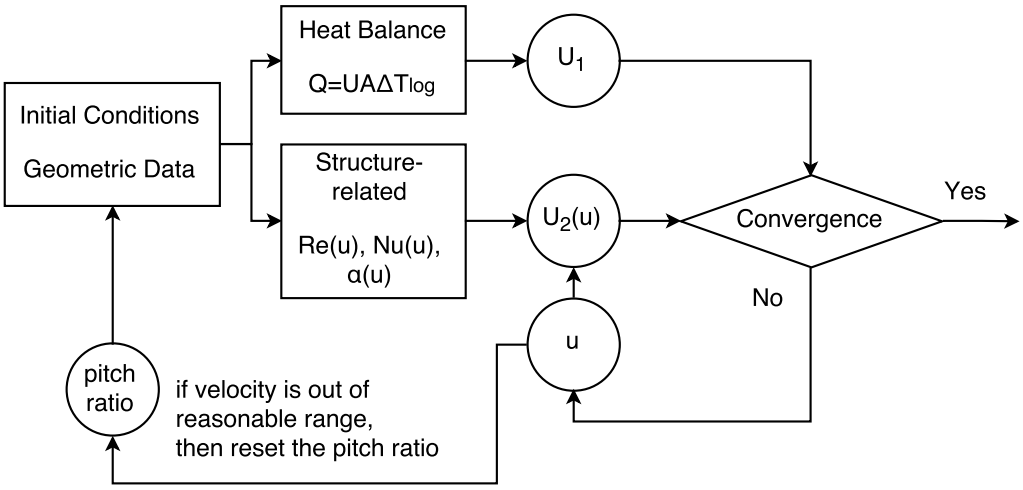


**Figure 5.3**: Iteration approach for the determination of the geometric data

### Coupled Criticality Calculation

The criticality calculation focuses mainly on the optimization of the fuel composition. To have a more practical result, a steady-state and coupled-physical model was developed by using the Monte Carlo code SERPENT and MATLAB. The reactor core model built by SERPENT was divided into 10 nodes uniformly in the axial direction and 10 subregions in the radial direction, which means the core model consists of 100 nodes. Each subregion in the radial direction has the same flow area for the fuel tubes and the coolant channels giving the same volume of each material in each region. In periphery the reactor core was wrapped by the coolant lead serving as the reflector (Figure 5.5). The MATLAB model has the same nodalization as the SERPENT model (Figure 5.4) and the heat source for each node was coupled to the power distribution converted from SERPENT. The temperature distributions of the fuel salt and the coolant were calculated with an in-house MATLAB module based on the stationary form of the volume-averaged energy conservation (Eq. 5.9), which means the $\frac{dT}{dt} = 0$:

$$\begin{cases} 0 = -\dfrac{UA_{1,reg}}{\rho_1 c_{p1} V_{1,reg}}(T_1^{i,j} - T_2^{i,j}) + \dfrac{P^{i,j}}{\rho_1 c_{p1}} + u_1 \dfrac{T_1^{i,j-1/2} - T_1^{i,j+1/2}}{\Delta x} \\ 0 = \dfrac{UA_{2,reg}}{\rho_2 c_{p2} V_{2,reg}}(T_1^{i,j} - T_2^{i,j}) + u_2 \dfrac{T_2^{i,j-1/2} - T_2^{i,j+1/2}}{\Delta x} \end{cases} \tag{5.9}$$

where $V_{reg}$ and $A_{reg}$ present the node volume and the node heat transfer area of each fluid. $P^{i,j}$ is the 2D power distribution and $T^{i,j}$ is the 2D temperature distribution to be solved. $T^{i,j-1/2}$ and $T^{i,j+1/2}$ are the edge temperatures of each node. $T^{i,j-1/2}$ is the inlet edge temperature, which can be determined by the previous node or the boundary condition, while $T^{i,j+1/2}$ is the outlet edge temperature, which can be calculated by the node temperature $T^{i,j}$ simply through Eq. 5.10:

$$T^{i,j} = \frac{T^{i,j-1/2} + T^{i,j+1/2}}{2} \tag{5.10}$$

Therefore, for each iteration step 100 set of the equations (Eq. 5.9) have to be solved. Specifically, the coupled criticality calculation was implemented with following procedures:

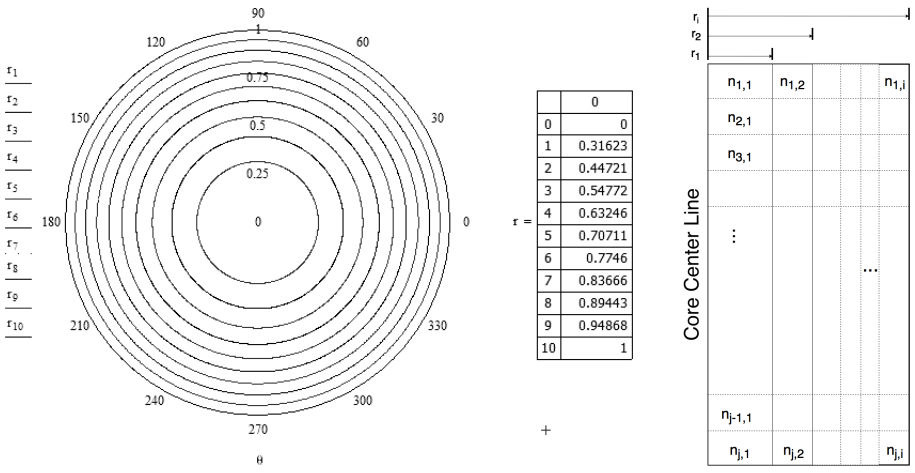


**Figure 5.4**: Radial and axial nodalization of the reactor core

1. The SERPENT code calculated the fission rate for each node with the initial temperatures and densities of the fuel salt and coolant respectively;

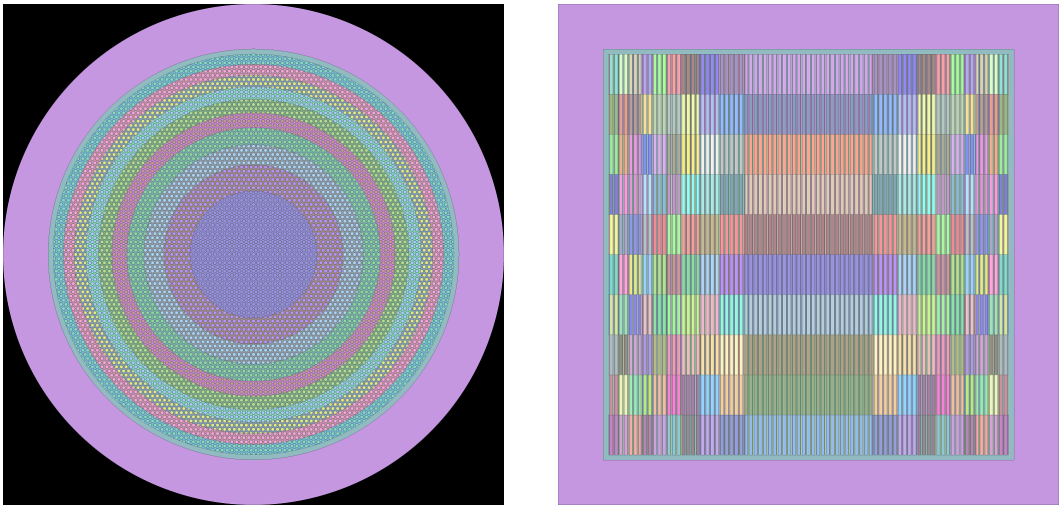

**Figure 5.5**: The nodalization in SERPENT model

2. The fission rate for each node was then converted to the node power;

3. The new temperatures and densities of the fuel salt and coolant were determined based on the energy conservation of each node through the MATLAB module (Eq. 5.9);

4. Compare each new node temperature with the corresponding initial node temperature for both the working fluids respectively. If the maximal error is still larger than the tolerance ($10^{-4}$), all the new node temperatures and densities are used to rewrite the input file of the SERPENT code and the calculation will be redone. Besides, once the temperatures converge, the MATLAB module will output the current power and temperature distributions as the final result.

The approach of this iteration is illustrated in Figure 5.6.

The temperature-dependent densities of the molten $UCl_3$ salt and of liquid lead were used to take into account the fuel density and coolant density reactivity feedback. The formula (Eq. 5.11) evaluating the fuel salt density was experimentally determined through pycnometric methods in 1969 within the temperature range from 1220K to 1300K, thus using this formula inevitably causes some uncertainties in the calculations. From a practical point of view this emphasizes the need to update the material properties for the specific fuel salt considered before any serious

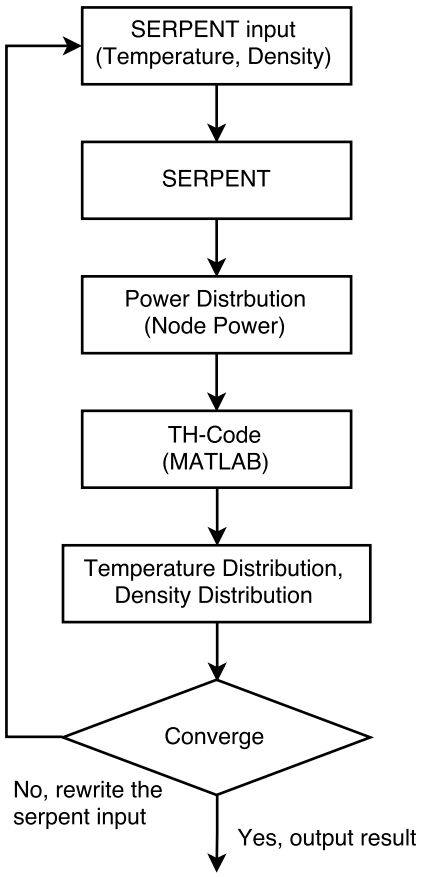


**Figure 5.6**: The coupling approach of the SERPENT and MATLAB code

design planning can start. From an academic point of view a sensitive analysis can be conducted in order to show the impact of this uncertainty on reactor safety parameters.

$$\rho_{fuel}(T) = 13.652[\frac{g}{cm^3}] - 7.943 \cdot 10^{-3}[\frac{g}{cm^3 \cdot K}] \cdot T \tag{5.11}$$

$$\rho_{coolant}(T) = 11.441[\frac{g}{cm^3}] - 1.2795 \cdot 10^{-3}[\frac{g}{cm^3 \cdot K}] \cdot T \tag{5.12}$$

The SERPENT calculation was implemented with 50000 neutrons and 50 active cycles using the cross-section library ENDF/B7. The uranium vector was set to have natural abundance of U-235, while the plutonium vector was taken from a typical

**Table 5.3**: Mass fraction of the isotopes in heavy metals

| Isotopes | Mass fraction (%) |
|---|---|
| Uranium | In uranium isotopes |
| U-238 | 99.28 |
| U-235 | 0.72 |
| Plutonium | In plutonium isotopes |
| Pu-238 | 1.44 |
| Pu-239 | 61.68 |
| Pu-240 | 24.19 |
| Pu-241 | 8.02 |
| Pu-242 | 4.67 |

MOX fuel type used for the commercial LWRs (Table 5.3).

According to the reference design of the DFR-3000 system, a PPU is connected to the fuel circuit, which means the fission products, the fertile material and the fresh fuel can be continuously removed, extracted and reloaded. Since the design data of the PPU is not finally completed yet, parallel burnup calculations were performed by SERPENT to see the superimposed effect of the fuel depletion and breeding as well as the poisonousness of the fission products, so as to roughly find out the minimal excess reactivity required to sustain the reactor critical for a certain time. In particular, the burnup calculations were started with the fuel vector, which can keep the $k_{eff}$ approximately at 1. Then SERPENT outputs the $k_{eff}$ after one-day to five-day operation without any fission products removal or fertile material extraction. Consequently, as listed in Table 5.4, the $k_{eff}$ was reduced to 0.999418, which means the reactor went sub-critical after a 2-day operation. Afterward, the fuel vector was tuned to produce a slight super-criticality value. The excessive part of the reactivity should compensate the $k_{eff}$ reduction in the 2-day burnup calculation, which means the $k_{eff}$ shouldn't be less than 1.001 even considering the uncertainty. Therefore, the fuel "F2" shown in Table 5.4 was chosen as the standard fuel for the following studies.

Additionally, those criticality values were determined by means of the implicit estimation of the SERPENT code. Particularly, SERPENT provides the users with three $k_{eff}$ estimations: analog, collision and implicit estimation. The analog estimation produces the $k_{eff}$ by calculating the ratio of the neutron sources of two

**Table 5.4**: Criticality and burnup calculation with different fuel vector

| calculation type | burnup (MWd/kgU) | fuel ID | fuel composition (mol%) $UCl_3$-$PuCl_3$ | $k_{eff}$ |
|---|---|---|---|---|
| criticality | – | F1 | 57.4-42.6 | 1.00063±0.00049 |
| burnup, day=1 | 0.2093 | – | – | 1.00039±0.00036 |
| burnup, day=2 | 0.4185 | – | – | 0.999418±0.00044 |
| burnup, day=3 | 0.6278 | – | – | 0.999278±0.00041 |
| burnup, day=4 | 0.8371 | – | – | 0.997686±0.00046 |
| burnup, day=5 | 1.0464 | – | – | 0.998720±0.00047 |
| criticality | – | F2 | 57.2-42.8 | 1.00188±0.00044 |

subsequent cycles (Eq. 5.13)

$$k_{eff,analog} = \frac{N_{n+1}}{N_n} \tag{5.13}$$

The collision estimation is obtained through calculating the ratio of the emitted neutrons and the initial neutron source (Eq. 5.14):

$$k_{eff,collision} = \frac{\overline{\nu} R_{fission}}{N_0} \tag{5.14}$$

where $\overline{\nu}$ is the average number of neutrons born per fission and $R_{fission}$ is the total fission rate. The criticality calculation based on the implicit estimation considers the capture rate, inelastic scattering production rate and leakage rate of neutrons. Its derivation is presented in Eq. 5.15:

$$k_{eff,implicit} = \frac{\overline{\nu} R_{fission}}{\overline{\nu} R_{fission} + R_{capture} - R_{inelastic} + R_{leakage}} \tag{5.15}$$

Among those estimations, the implicit estimation may offer a more practical result, because in this way the neutrons, which truly have interacted with the target materials, are taken into account.

Finally, the coupled-physical steady-state simulation was completed and the results were presented in Figure 5.7. The power distribution has a cosine-like profile as a typical power shape of a nuclear reactor and the fuel temperature distribution

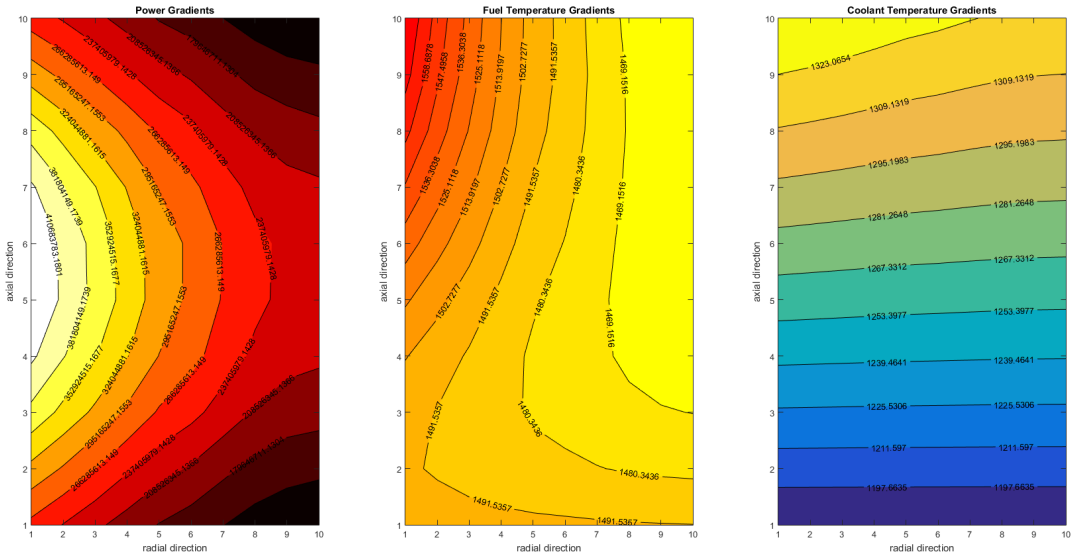


**Figure 5.7**: 2D core power distribution and the fuel salt and coolant temperature gradients for steady-state coupled calculation

looks comparative with the results from MSFR [64]. Therefore, the simulation was successfully done and its results can be used as a reasonable initial conditions for the following transient simulations.

### 5.2.2 Neutron Physics Model

The time-dependent behavior of the neutron population was modeled with the one-dimensional and multi-group point-kinetic equations considering the precursor loss (Eq. 5.16). Not like the MSRE, due to the relatively long circulation time of the fuel salt in the DFR concept, the re-entering rate of the delayed neutron precursors has been neglected.

$$\begin{cases} \dfrac{\partial P(t)}{\partial t} = \dfrac{R(t)-\beta}{\Lambda} P(t) + \displaystyle\sum_{i=1}^{n} \lambda_i C_i(t) \\ \dfrac{\partial C_i(t)}{\partial t} + \dfrac{\partial (u C_i(t))}{\partial x} = -\lambda_i C_i(t) + \dfrac{\beta_i}{\Lambda} P(t) \end{cases} \tag{5.16}$$

The group constants were derived by the SERPENT calculation. Also the temper-

ature coefficients for the fuel salt and the coolant were determined with the help of SERPENT considering both the Doppler and the density reactivity feedback effect. The corresponding reactivities were evaluated by Eq. 5.17.

$$R(\rho, T) = \frac{k_{eff}(\rho, T) - 1}{k_{eff}(\rho, T)} \tag{5.17}$$

As presented in Figure 5.8 and Table 5.5 comparatively large temperature coefficients of reactivity of about -180pcm/K were observed at the operating temperature range. This is a very large negative feedback coefficient compared to around -40pcm/K for another study on the DFR [65] and -50pcm/K for a typical PWR. This can be mainly explained by the increasing thermal expansion with increasing operating temperature. Table 5.6 shows evidently that the thermal expansion at 1500K is almost twice as large as the value at 1300K and Table 5.7 indicates that at lower operating temperature range (e.g. at 1200K to 1300K) the reactivity feedback coefficient of the fuel salt has a general agreement with the reference study [65]. Based on this observation it seems that the DFR can have such a large reactivity feedback coefficient due to its high operating temperature.

**Table 5.5**: Temperature coefficients of reactivity of the fuel salt at different operating temperatures (combination of Doppler and density effect, coolant lead temperature = 1173K)

| temperature [K] | density [g/cm$^3$] | $k_{eff}$ | $\Delta k_{eff}$ | R | $\Delta$R | $\alpha_F$ |
|---|---|---|---|---|---|---|
| 1550 | 1.3404 | 0.9408 | -0.0095 | -0.0629 | -0.0106 | -0.0021 |
| 1545 | 1.3801 | 0.9503 | -0.0086 | -0.0523 | -0.0094 | -0.0019 |
| 1540 | 1.4198 | 0.9589 | -0.0096 | -0.0428 | -0.0103 | -0.0021 |
| 1535 | 1.4595 | 0.9685 | -0.0089 | -0.0325 | -0.0094 | -0.0019 |
| 1530 | 1.4992 | 0.9774 | -0.0089 | -0.0231 | -0.0092 | -0.0018 |
| 1525 | 1.5389 | 0.9862 | -0.0098 | -0.0140 | -0.0100 | -0.0020 |
| 1520 | 1.5786 | 0.9961 | -0.0079 | -0.0039 | -0.0079 | -0.0016 |
| 1515 | 1.6184 | 1.0040 | -0.0080 | 0.0040 | -0.0078 | -0.0016 |
| 1510 | 1.6581 | 1.0120 | -0.0094 | 0.0118 | -0.0091 | -0.0018 |
| 1505 | 1.6978 | 1.0214 | -0.0080 | 0.0209 | -0.0076 | -0.0015 |
| 1500 | 1.7375 | 1.0294 | - | 0.0286 | - | - |

On the other hand, the investigation of the fuel salt reactivity feedback caused only by the Doppler effect was also concerned. For this purpose, parallel criticality calculations were carried out with a temperature interval of 200K and with the fuel

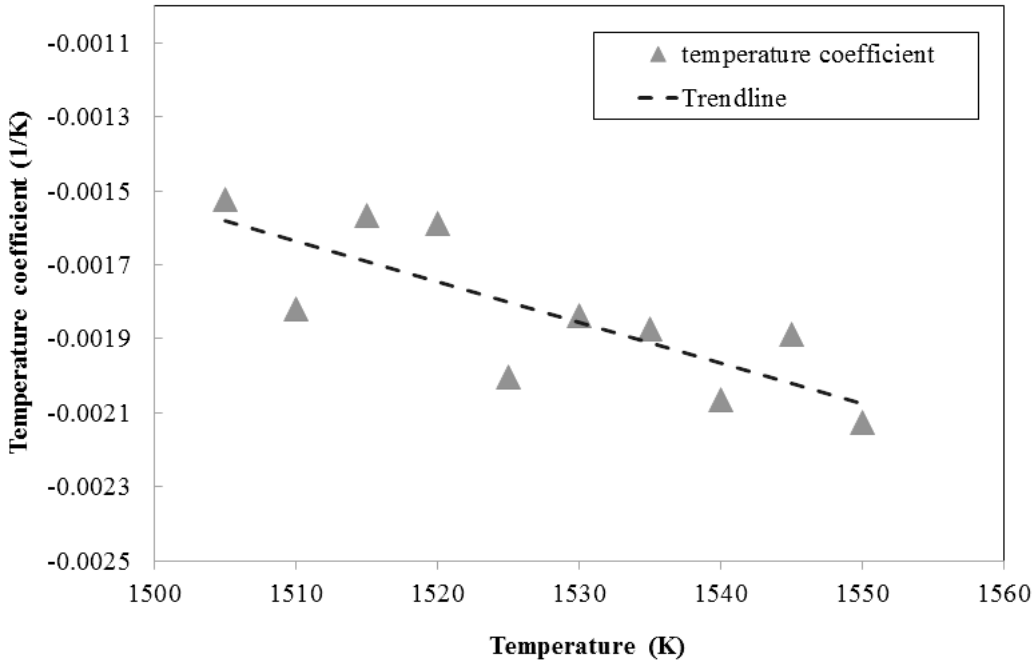


**Figure 5.8**: The temperature coefficient of reactivity of the fuel salt at different operating temperatures (combination of Doppler and density effect, coolant lead = 1273K)

**Table 5.6**: Temperature-dependent thermal expansion for the fuel salt

| Temperature (K) | Density (g/cm$^3$) | Thermal expansion (1/K) |
|---|---|---|
| 1000 | 5.7090 | – |
| 1050 | 5.3119 | 0.001495 |
| 1100 | 4.9147 | 0.001616 |
| 1150 | 4.5176 | 0.001758 |
| 1200 | 4.1204 | 0.001928 |
| 1250 | 3.7233 | 0.002133 |
| 1300 | 3.3261 | 0.002388 |
| 1350 | 2.9290 | 0.002712 |
| 1400 | 2.5318 | 0.003137 |
| 1450 | 2.1347 | 0.003721 |
| 1500 | 1.7375 | 0.004572 |
| 1550 | 1.3404 | 0.005926 |
| 1600 | 0.9432 | 0.008421 |

salt density unchanged. The results were given in Table 5.8 which shows that the negative reactivity feedback from the Doppler effect is trivial. Furthermore, the evaluation for the reactivity feedback of the liquid lead was also done. Table 5.9 indicates that the temperature coefficient of the liquid lead is much smaller than the fuel salt mainly due to its much smaller thermal expansion. Finally, the averaged

**Table 5.7**: Comparison of the temperature coefficients of reactivity feedback between operating temperature and lower reference temperatures considering both Doppler and density effect

| Temperature (K) | Density (g/cm$^3$) | Temperature coefficient (1/K) |
|---|---|---|
| 1600 | 0.9432 | – |
| 1550 | 1.3400 | -0.002447615 |
| 1500 | 1.7370 | -0.001960047 |
| 1450 | 2.1350 | -0.001240762 |
| 1400 | 2.5320 | -0.001205644 |
| 1300 | 3.3260 | -0.000741532 |
| 1200 | 4.1200 | -0.000535189 |

**Table 5.8**: Temperature coefficients of reactivity of the fuel salt at different operating temperatures (considering only Doppler effect, $\rho_{fuel}$=1.737[g/cm$^3$], coolant lead temperature = 1173K)

| temperature [K] | $k_{eff}$ | $\Delta k_{eff}$ | R | $\Delta$R | $\alpha_F$ |
|---|---|---|---|---|---|
| 2000 | 1.02697 | -0.00089 | 0.02626 | -0.00084 | -4.22E-06 |
| 1800 | 1.02786 | -0.00075 | 0.02710 | -0.00071 | -3.55E-06 |
| 1600 | 1.02861 | -0.00090 | 0.02781 | -0.00085 | -4.25E-06 |
| 1400 | 1.02951 | -0.00105 | 0.02866 | -0.00099 | -4.95E-06 |
| 1200 | 1.03056 | – | 0.02965 | – | – |

**Table 5.9**: Temperature coefficients of reactivity of the coolant at different operating temperatures (combination of Doppler and density effect, fuel salt temperature = 1500K)

| temperature [K] | density [g/cm$^3$] | $k_{eff}$ | $\Delta k_{eff}$ | R | $\Delta$R | $\alpha_C$ |
|---|---|---|---|---|---|---|
| 1373 | 9.684 | 1.02323 | – | 0.0227 | – | – |
| 1323 | 9.748 | 1.02776 | 0.00453 | 0.0270 | 0.004308 | -8.62E-05 |
| 1273 | 9.812 | 1.02807 | 0.00031 | 0.0273 | 0.0002934 | -5.87E-06 |
| 1223 | 9.876 | 1.02878 | 0.00071 | 0.0278 | 0.0006713 | -1.34E-05 |

temperature coefficients of the both working fluids as well as the necessary point-kinetic parameters are listed in Table 5.10.

**Table 5.10**: Point-kinetic parameters and average temperature coefficients

| | group1 | group2 | group3 | group4 | group5 | group6 | $\Lambda$ | $\alpha_F$ | $\alpha_C$ |
|---|---|---|---|---|---|---|---|---|---|
| $\beta$ | 8.94E-5 | 6.85E-4 | 5.10E-4 | 1.15E-3 | 4.96E-4 | 1.22E-5 | 2.45E-6 | -1.83E-3 | -2.3E-5 |
| $\lambda$ | 0.0128 | 0.0300 | 0.1106 | 0.3171 | 1.1437 | 5.8915 | – | – | – |

Instead of the entire reactor core, the study of the reactor dynamics was reduced to

the channel scale. Herein an axially discretized fuel channel model with $n$ nodes was built (Figure 5.9). Therefore, the divergence of the delayed neutron precursors along the axial direction at the $j$th node can be written in the differentiation form, hence the partial differential equations (Eq. 5.16) above became the ordinary differential equations (ODEs) (Eq. 5.18). Again the initial power of each node was converted from the fission rate of each "detector" in the SERPENT result file. The initial precursor concentrations of each group can be determined by Eq. 5.19, which was derived by assuming $\frac{dC_i^j}{dt} = 0$.

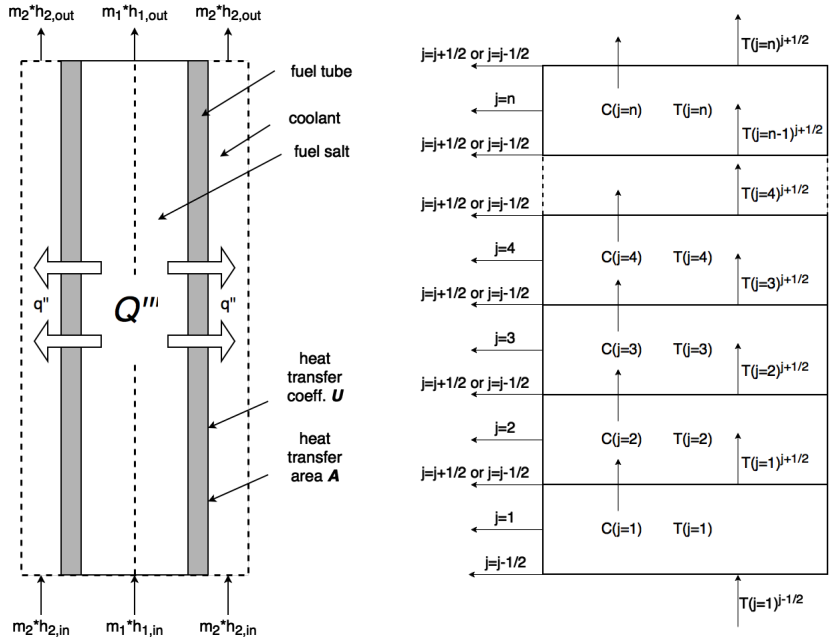


**Figure 5.9**: Single fuel channel and its axial discretization

$$\begin{cases} \dfrac{dP^j(t)}{dt} = \dfrac{R(t)-\beta}{\Lambda}P^j(t) + \displaystyle\sum_{i=1}^{n}\lambda_i C_i^j(t) \\ \dfrac{dC_i^j(t)}{dt} = -\lambda_i C_i^j(t) + \dfrac{\beta_i}{\Lambda}P^j(t) + \dfrac{u}{\Delta x}(C_i^{j-1}(t) - C_i^j(t)) \end{cases} \tag{5.18}$$

$$C_i^j(t=0) = \frac{\dfrac{\beta_i}{\Lambda}P^j(t=0) + \dfrac{u}{\Delta x}C_i^{j-1}(j=1)}{\lambda_i + \dfrac{u}{\Delta x}} \tag{5.19}$$

### 5.2.3 Thermal-hydraulic Model

The following three fundamental conservation equations (continuity, momentum and energy) in one dimension were used as below (Eq. 5.20):

$$\begin{cases} \dfrac{\partial \rho}{\partial t} + \dfrac{\partial (\rho u)}{\partial x} = 0 \\ \rho \dfrac{\partial u}{\partial t} = -\dfrac{\partial p}{\partial x} + \mu \dfrac{\partial^2 u}{\partial x^2} + \rho g \\ (\rho c_p V) \dfrac{\partial T}{\partial t} + \dfrac{\partial (u \rho c_p V T)}{\partial x} = UA(T - T') + VP \end{cases} \tag{5.20}$$

Assuming an incompressible flow and neglecting the divergence of the pressure and the impact of the gravity, only the energy conservation remains to be solved. Again the temperature distribution along the axial direction is divided into n nodes and the volumetric averaged energy conservation at the $j$th node for the fuel salt and coolant was built as follows (Eq. 21):

$$\begin{cases} \dfrac{dT_1^j}{dt} = -\dfrac{UA^j}{\rho_1 c_{p1} V_1^j}(T_1^j - T_2^j) + \dfrac{P^j}{\rho_1 c_{p1}} + u_1 \dfrac{T_1^{j-1/2} - T_1^{j+1/2}}{\Delta x} \\ \dfrac{dT_2^j}{dt} = \dfrac{UA^j}{\rho_2 c_{p2} V_2^j}(T_1^j - T_2^j) + u_2 \dfrac{T_2^{j-1/2} - T_2^{j+1/2}}{\Delta x} \end{cases} \tag{5.21}$$

And the temperature for each node is the arithmetic mean value of the two edge temperatures of the current node (Eq. 5.22):

$$T_{j=1} = \frac{T_{j=1}^{j-1/2} + T_{j=1}^{j+1/2}}{2} \tag{5.22}$$

Again the total heat transfer coefficient U was built as a function of the flow velocities of the two working fluids (Eq. 5.3). The relevant Nusselt numbers were determined

both for laminar and turbulent flow regimes by comparing the current Reynolds numbers to their critical values. In addition, the time-dependent reactivity $R(t)$ in Eq. 5.23 actually consists of several parts: the initial compensative reactivity , the temperature feedback reactivity (combining the Doppler feedback and the feedback due to the density changes of the fuel salt or the coolant lead) and the externally inserted reactivities.

$$R(t) = R_0 + \alpha_{T,1}(T_1(t) - T_{1,0}) + \alpha_{T,2}(T_2(t) - T_{2,0}) + R_{insert}(t) \tag{5.23}$$

The final one-dimensional neutron-physical and thermal-hydraulic coupled model to be solved are as follows (Eq. 5.24). The temperature differentiation along the axial direction was rewritten as a relation between the current and the previous node. The heat transfer coefficient was considered to have the velocity-dependent form. Additionally, the densities of the working fluids were set to be constant during the simulation, since the reactivity feedback coefficients were already averaged for the operating temperature range, which means the reactivity feedback coefficients were not density-dependent for the dynamic simulations.

$$\begin{cases} \dfrac{dP^j}{dt} = \dfrac{R(t) - \beta_{tot}}{\Lambda} P^j + \displaystyle\sum_{i=1}^{n} \lambda_i C_i^j \\ \dfrac{dC_i^j}{dt} = -\lambda_i C_i^j + \dfrac{\beta_i}{\Lambda} P^j + \dfrac{u}{\Delta x}(C_i^{j-1} - C_i^j) \\ \dfrac{dT_1^j}{dt} = -\dfrac{U(u_1,u_2)A^j}{\rho_1 c_{p1} V_1^j}(T_1^j - T_2^j) + \dfrac{P^j}{\rho_1 c_{p1}} + 2u_1 \dfrac{T_1^j - (2T_1^{j-1} - T_1^{j-3/2})}{\Delta x} \\ \dfrac{dT_2^j}{dt} = \dfrac{U(u_1,u_2)A^j}{\rho_2 c_{p2} V_2^j}(T_1^j - T_2^j) + 2u_2 \dfrac{T_2^j - (2T_2^{j-1} - T_2^{j-3/2})}{\Delta x} \end{cases} \tag{5.24}$$

### 5.2.4 Selection of the Proper Numerical Solver

For fast reactors the prompt neutron generation time usually has the magnitude of about $10^{-6}$s, which may make the point-kinetic equations a very stiff problem.

Based on this assumption, only the implicit methods were thought to be suitable for solving the coupled equations above (Eq. 5.19). Therefore, the numerical solvers to be employed here include the Radau-IIA (RAD), Backward Differentiation Formula (BDF), Bulirsch-Stöer (BUL) and Rosenbrock (ROS) methods [70] [71]. These methods were parallel assessed using the mathematic tools such as the MATLAB and MATHCAD, where the mentioned methods were already built in for users.

Among these ODE solvers, the RAD method was previously taken as the conservative choice for the current work, because the RAD method is a 3-stage and 5th order fully implicit Runge-Kutta method, which was proven as a stable numerical solver for the stiff point-kinetic equations [72] and comparing to the BDF method it needs fewer steps to obtain the solution thus relatively lowering the computational cost. The ROS method is more time-efficient than RAD because of its lower stage and order but giving worse accuracy than the RAD method. The BUL method is based on the approach of Richardson's extrapolation, which is predicted to be more suitable for smooth functions, thus it might not be suitable for the large transients. In following the solving procedures of these numerical methods were briefly discussed.

Considering a basic form of an ordinary differential equations to be like (Eq. 5.25):

$$y' = f(t, y) \tag{5.25}$$

Then the derivation of the RAD method was given as (Eq. 5.26):

$$y_{n+1} = y_n + h \sum_{i=1}^{s} b_i k_i, \qquad i = 1, 2..., s \tag{5.26}$$

where $k_i$ is determined by the equation below (Eq. 5.27):

$$k_i = f(t_n + c_i h, y_n + h \sum_{j=1}^{s} a_{ij} k_j) \tag{5.27}$$

The coefficients for the RAD method, namely $a_{ij}$, $b_i$ and $c_i$ were selected from the so-called Butcher's tableau given in Table 5.11.

**Table 5.11**: Butcher's tableau for RAD method

| $c_i,\ b_i$ | $\frac{4}{9}-\frac{\sqrt{6}}{36}$ | $\frac{4}{9}+\frac{\sqrt{6}}{36}$ | $\frac{1}{9}$ |
|---|---|---|---|
| $\frac{2}{5}-\frac{\sqrt{6}}{10}$ | $\frac{11}{45}-\frac{7\sqrt{6}}{360}$ | $\frac{37}{225}-\frac{169\sqrt{6}}{1800}$ | $-\frac{2}{225}+\frac{\sqrt{6}}{75}$ |
| $\frac{2}{5}+\frac{\sqrt{6}}{10}$ | $\frac{37}{225}+\frac{169\sqrt{6}}{1800}$ | $\frac{11}{45}+\frac{7\sqrt{6}}{360}$ | $-\frac{2}{225}-\frac{\sqrt{6}}{75}$ |
| 1 | $\frac{4}{9}-\frac{\sqrt{6}}{36}$ | $\frac{4}{9}+\frac{\sqrt{6}}{36}$ | $\frac{1}{9}$ |

Similarly based on the implicit Runge-Kutta method, the ROS method has the same derivation to determine $y_{n+1}$ (Eq. 5.26), the difference is how ROS method calculates the $k$ factor (Eq. 5.28):

$$k_i^n = h \cdot f(y^n + \sum_{j=1}^{i-1} a_{ij} k_j^n) + h \cdot J \sum_{j}^{i} \gamma_{ij} k_j^n \tag{5.28}$$

where the $J$ is called Jacobian Matrix, whose general form looks like (E. 5.29):

$$J = \begin{pmatrix} \frac{\partial f_1}{\partial y_1} & \frac{\partial f_1}{\partial y_2} & \cdots & \frac{\partial f_1}{\partial y_n} \\ \frac{\partial f_2}{\partial y_1} & \cdots & \cdots & \frac{\partial f_2}{\partial y_n} \\ \cdots & \cdots & \cdots & \cdots \\ \frac{\partial f_n}{\partial y_1} & \cdots & \cdots & \frac{\partial f_n}{\partial y_n} \end{pmatrix} \tag{5.29}$$

Other than the numerical integration the BDF method is based on the approach of the numerical differentiation, whose implicit formulas is presented in Eq. 5.30.

$$\sum_{j=1}^{k} \frac{1}{j} \nabla^j y_{n+1} = h f_{n+1} \tag{5.30}$$

As the BDF method is unstable when $k > 6$, thus it is usually implemented from 1

to 5 steps like the built-in function *"ode15s"* in MATLAB. The derivations of each step were listed below (Eq. 5.31):

$$\begin{cases} k=1: & y_{n+1}-y_n = hf_{n+1}, \\ k=2: & \frac{3}{2}y_{n+1}-2y_n+\frac{1}{2}y_{n-1} = hf_{n+1}, \\ k=3: & \frac{11}{6}y_{n+1}-3y_n+\frac{3}{2}y_{n-1}-\frac{1}{3}y_{n-2} = hf_{n+1}, \\ k=4: & \frac{25}{12}y_{n+1}-4y_n+3y_{n-1}-\frac{4}{3}y_{n-2}+\frac{1}{4}y_{n-3} = hf_{n+1}, \\ k=5: & \frac{137}{60}y_{n+1}-5y_n+5y_{n-1}-\frac{10}{3}y_{n-2}+\frac{5}{4}y_{n-3}-\frac{1}{5}y_{n-4} = hf_{n+1} \end{cases} \tag{5.31}$$

The BUL method is also called Gragg-Bulirsch-Stöer (GBS) method, whose goal is to compute the $y(t_0+H)$, where $H$ is a big time step divided by a step-number sequence ($n_i$, Eq. 5.32) thus obtaining a step-size sequence ($h_i$, Eq. 5.33).

$$n_1 < n_2 < n_3 < \dots \tag{5.32}$$

$$h_1 > h_2 > h_3 > \dots \tag{5.33}$$

And the approximation of the $y(t_0+H)$, named $u(t_0+H)$, was calculated with the help of the Aitken-Neville algorithm (Eq. 5.34):

$$u(t_0+H) = F_{j,k+1} = F_{j,k} + \frac{F_{j,k}-F_{j-1,k}}{\frac{n_j}{n_{j-k}}-1} \tag{5.34}$$

To preliminarily investigate the relative local errors of the BDF, BUL and ROS method compared with the RAD method in condition of the transient simulations, the coupled model was temporarily reduced to 1-node and 1-group. The transients introduced here are the 100pcm step insertion of reactivity and the 75% step reduction of the initial fuel salt flow velocity. The power evolution was chosen for the

**Table 5.12**: Indexes of the different time step sizes for the evaluation of the relative local error

| index | 1 | 2 | 3 | 4 | 5 | 6 | 7 | 8 |
|---|---|---|---|---|---|---|---|---|
| h | 0.04 | 0.025 | 0.02 | 0.0125 | 0.01 | 0.00625 | 0.005 | 0.004 |
| index | 9 | 10 | 11 | 12 | 13 | 14 | 15 | |
| h | 0.00325 | 0.0025 | 0.002 | 0.00125 | 0.001 | 0.0005 | 0.0001 | |

error analysis.

Figure 5.10 and Figure 5.11 present the local errors of each method (BDF, BUL or ROS) compared with the RAD method at series of the same time points but with various step sizes separately. In particular, the errors were evaluated from the time point of the transient initiation ($t_0$) to the time point ($t_0 + 0.5s$) with an interval of 0.05s, which means 10 data points after the transient initiation were extracted for the error analysis. Among these 10 data points obtained from each method the maximal and the minimal errors were determined and the average error was calculated. The index "-max", "-min" or "-avg" in the legend box in Figure 5.10 or Figure 5.11 correspond to these errors. The indexes on the x-axis in Figure 5.10 and Figure 5.11 present the different step sizes, which are explained in Table 5.12.

The results show that with reducing step size, the relative local errors are decreasing for all the numerical solvers. The BDF method seems to have a better agreement with the RAD method. The BUL and ROS methods give a better time efficiency but with a relative lower accuracy and moreover, the Jacobian Matrix is required to be determined for these methods which also causes extra computational load. Generally, the aim of this section is to find a numerical solver, which can have a good balance among the accuracy, time-efficiency and the computational load, but the accuracy was taken as the priority at the moment. Therefore, based on the results above and the reference studies [73], which advised to use the method of a higher order to solve the stiff point-kinetic equations for the MSFR, the RAD method was finally chosen as the optimized numerical solver.

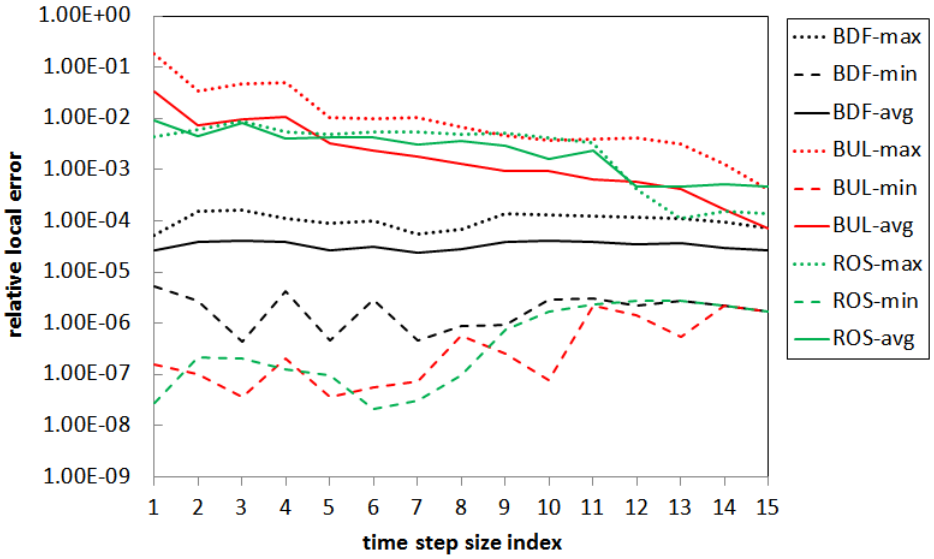


**Figure 5.10**: Average local error to the RAD method at different time step sizes for the transient of 100pcm step insertion of reactivity

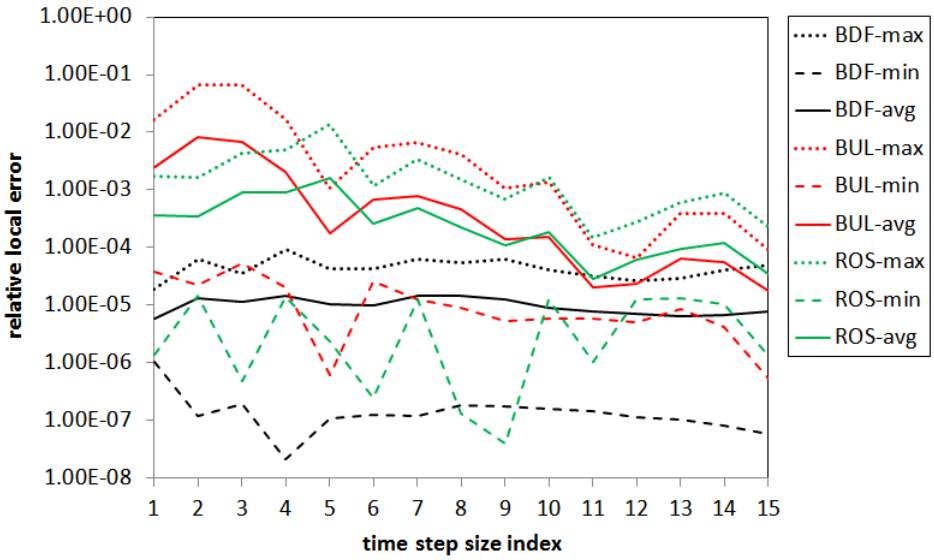


**Figure 5.11**: Average local error to the RAD method at different time step sizes for the transient of 75% step reduction of the initial flow velocity of the fuel salt

### 5.2.5 Impact of Applying Different Number of Delay Neutron Groups

In this section the impact of choosing different number of delay neutron groups was assessed. Again the 100pcm step reactivity insertion was taken as the reference scenario and the reactor core model was simplified to have only one node. The time

step size was 0.001s. Figure 5.12 describes it evidently that when considering more groups, the system damping became larger, which means the transient peak was reduced and the system converged much more quickly. Furthermore, Figure 5.13 is about the responses of the relative precursor concentrations, which were calculated by the ratio between the current precursor concentration and its initial value. This figure also shows that considering only one group (dash line) the system took longer time to be re-stabilized than simulation with 6 groups. Therefore, it seems that the averaged one-group parameters are not suitable for the transient simulations of the DFR concept.

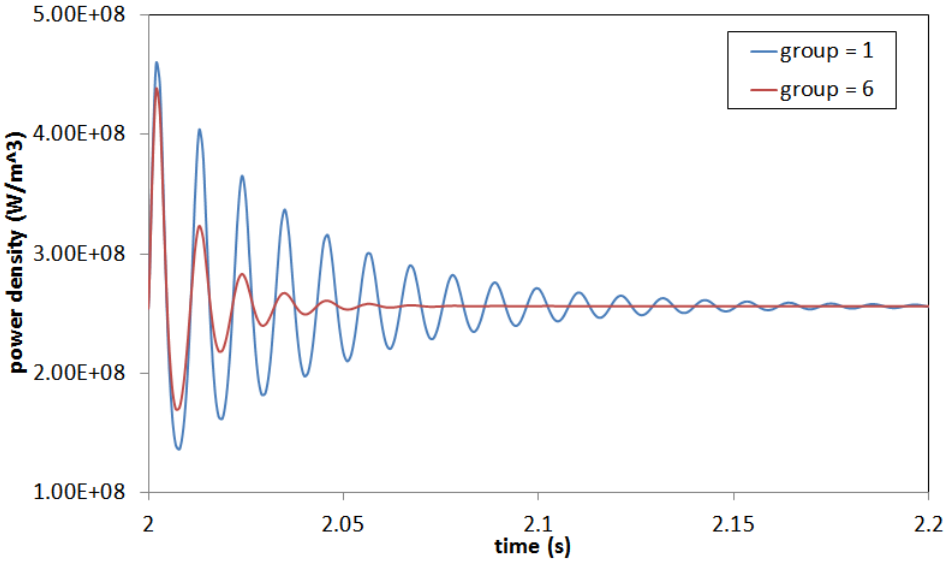


**Figure 5.12**: Responses of the average channel power density to 100pcm step reactivity insertion considering with one or six groups

### 5.2.6 Impact of Different Nodalizations

The axial nodalization of the fuel channel brings about the changes on temperature profile along the axial direction, which furthermore changes the average initial temperatures for both working fluids. With different initial conditions the solution of the coupled-physical equations should be different, which is called the initial value problem (IVP). Table 5.13 lists the steady-state average channel temperatures calculated from the different nodalizations for the working fluids. Moreover, Figure 5.14 illustrates the axial fuel temperature distributions with different node numbers.

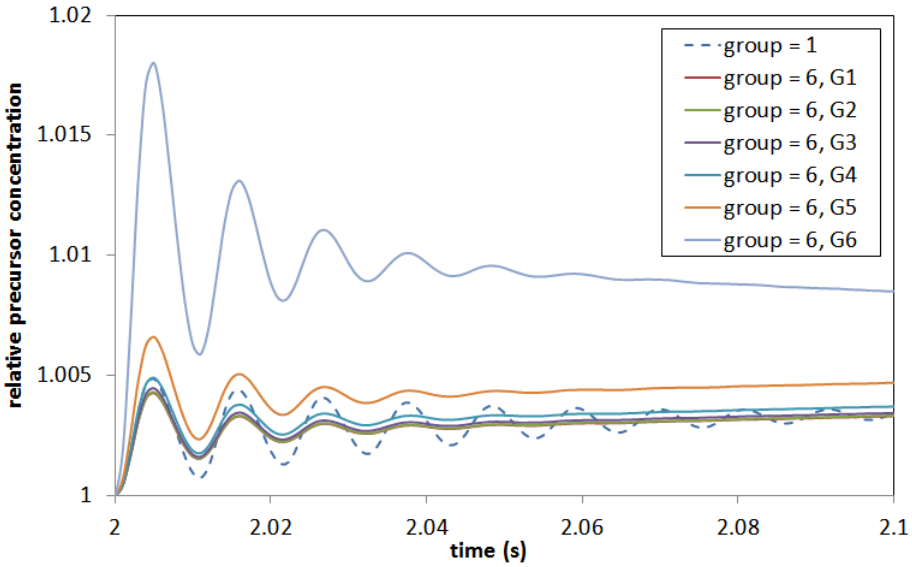


**Figure 5.13**: Responses of relative precursor concentrations of 100pcm step reactivity insertion considering with one or six groups

Looking at Figure 5.14 a temperature sink of the fuel salt appeared near the core entrance, which means the fuel salt was eventually cooled by the liquid lead instead of being heated up by the fission power. This can be partly explained by two facts: first, the entrance temperature of the liquid lead has a temperature gradient of more than 300K, which can cause a strong heat transfer between the fuel and coolant; second, the power level near the core entrance is relative low thus not sufficient to increase the fuel temperature at this region.

**Table 5.13**: Steady-state average channel temperature calculated by different nodalizations

| nodes | fuel temperature (K) | coolant temperature (K) |
|---|---|---|
| 1 | 1510.1100 | 1290.2100 |
| 5 | 1504.8003 | 1296.3395 |
| 10 | 1504.8419 | 1296.2914 |
| 50 | 1504.8556 | 1296.2756 |
| 100 | 1504.8560 | 1296.2751 |
| 500 | 1504.8561 | 1296.2750 |
| 1000 | 1504.8562 | 1296.2750 |

Here additional remark is that the corresponding power used to calculate the node temperatures was assumed to have a perfect cosine distribution along the axial direction. Then the smooth power profile was discretized depending on the number of

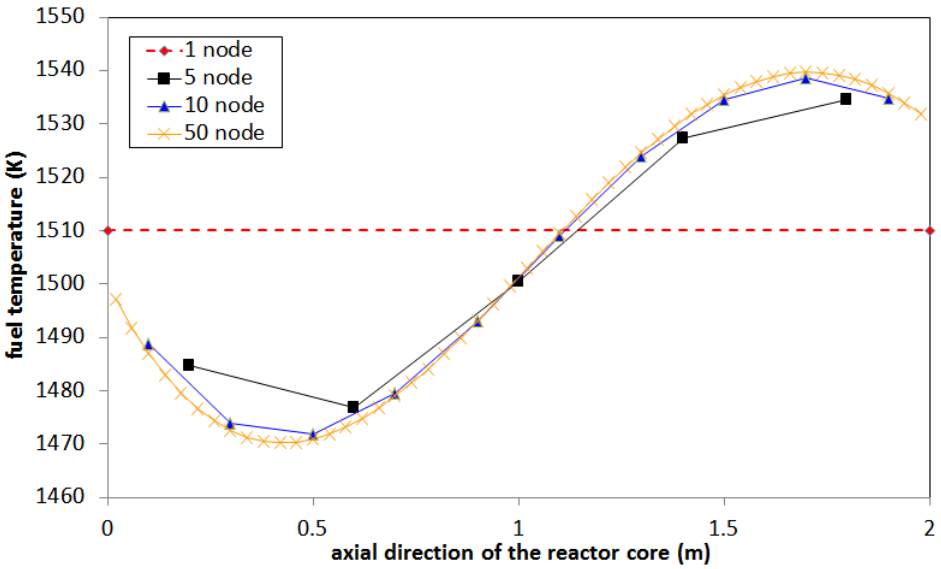


**Figure 5.14**: Axial fuel temperature distribution with 1/5/10/50 nodes

nodes (Figure 5.15) and the node power was determined by Eq. 5.35. Consequently, it shows that large discrepancy only happened between the 1-node and 5-node model and with the increasing node number the average initial temperature converged (Table 5.13). This observation helps to figure out the balance between the necessity of the system complexity and the requirement of the computational accuracy.

$$P^j = P_{peak} \frac{\int_{-0.5\pi+\frac{\pi}{n}(j-1)}^{-0.5\pi+\frac{\pi}{n}j} \cos x dx}{\pi/n}, \quad j = 1, 2, ..., n \tag{5.35}$$

Figure 5.16 presents the power and fuel temperature responses to the 100pcm step reactivity insertion implementing different number of nodes with 6 groups. From the result, it is noticeable that the 1-node model built its equilibrium temperature at another level due to the initial value problem. The power responses had no significant discrepancy, but it seems that the power oscillation of the 1-node model were slightly expanded. This can be partly explained by the dimensional effect, which is similar to the statement in *section 4.3*.

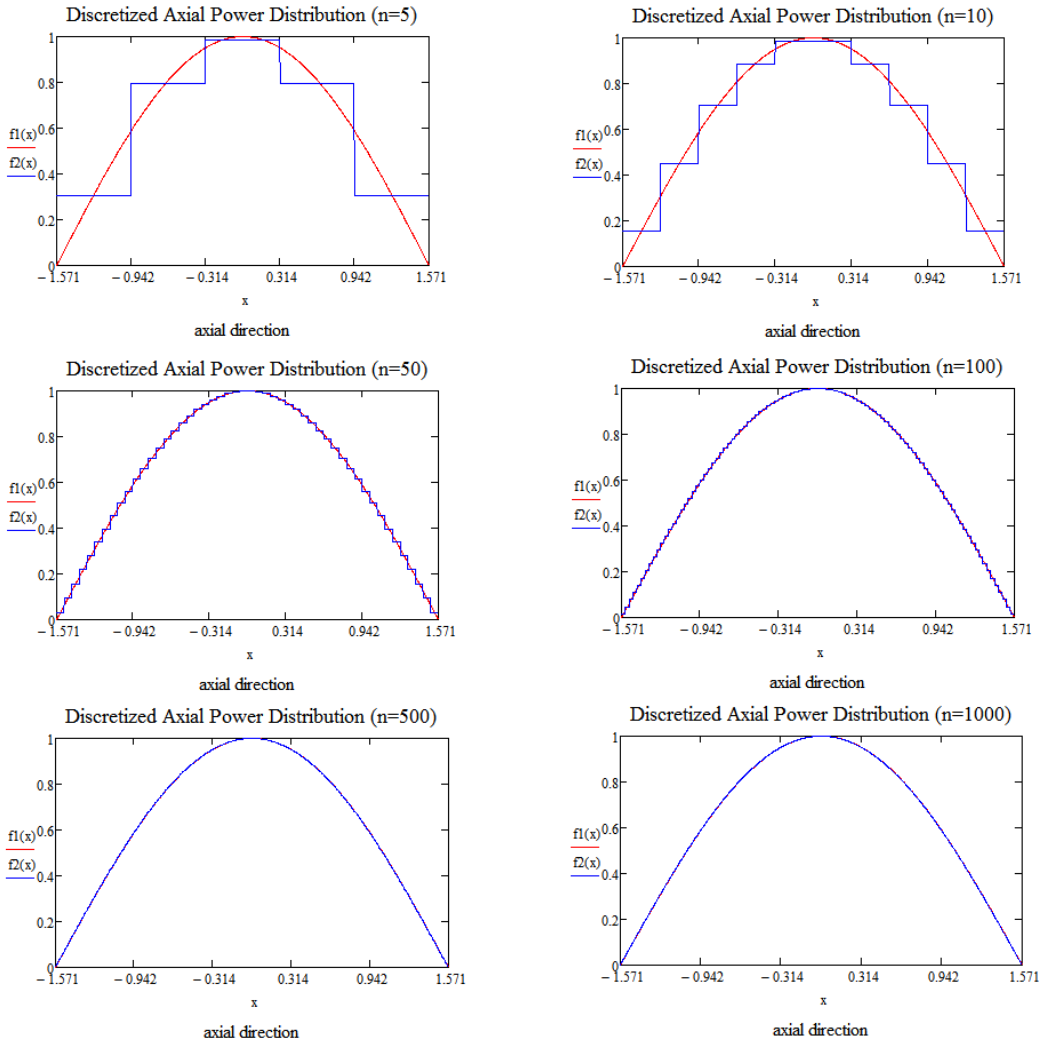


**Figure 5.15**: Discretized axial power distribution with different node number

### 5.2.7 Impact of Different Feedback Coefficient of Reactivity

Till now the single fuel channel model has already considered the impact of the group number and the channel nodalization, however, the system still has a relatively long-term oscillation, which is empirically not expected for a safe reactor operation. This problem is currently thought to be connected to the large reactivity feedback coefficient of the fuel salt. Based on this, in following some simulations were done to investigate the impact of different feedback coefficients. For this time the scenario with 100pcm step reactivity insertion was still taken as the reference case and the calculation was performed with the time step size of 0.001s. Figure 5.17 and Figure 5.18 present that with different feedback coefficients the power and the temperature

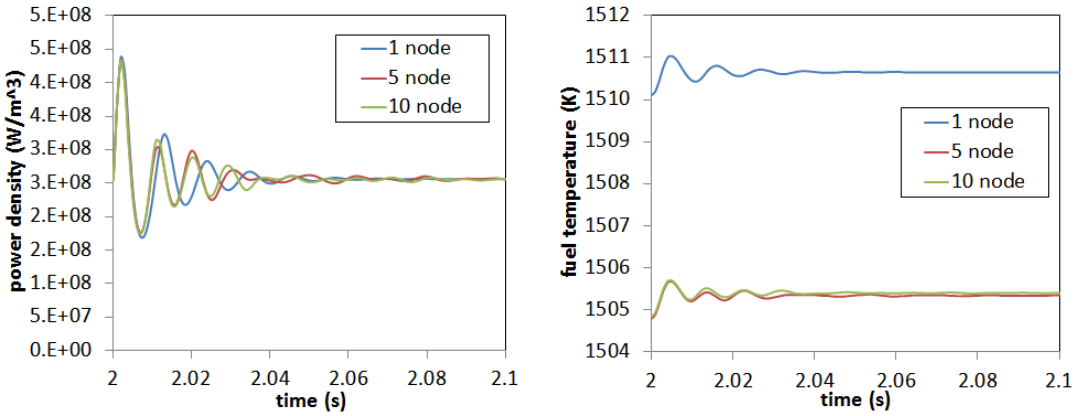


**Figure 5.16**: Responses of the average channel power density (left) and fuel salt temperature (right) to 100pcm step insertion of reactivity with 1/5/10 nodalized channel with 6 groups

revolutions look significantly different from each other. In particular, the smaller the reactivity feedback coefficient was, the higher the peak power appeared but the less cycles the oscillation occurred. Therefore, once again it seems that a deeper study on the temperature-dependent density of the fuel salt is crucially important to obtain a more reliable and practical result. In the following chapter, however, we still used the reactivity feedback coefficient of the fuel salt shown in Table 5.10 due to lack of reference studies at the comparable temperature range for the DFR concept.

Based on all the calculations done above, the decision was made, that is to build the fuel channel model with 6-group point-kinetic equations and with 10 axial nodes. Hence, there are 90 equations to be solved for each channel. Moreover, 10 independent single fuel channels were selected from the 10 subregions respectively in order to representatively describe the dynamic behavior of the corresponding regions. The RAD method was confirmed as the default numerical solver and was executed with the maximal allowed time step size of $10^{-4}$. The initial conditions including the powers and temperatures for each node were obtained from the coupled simulation by the SERPENT-MATLAB code.

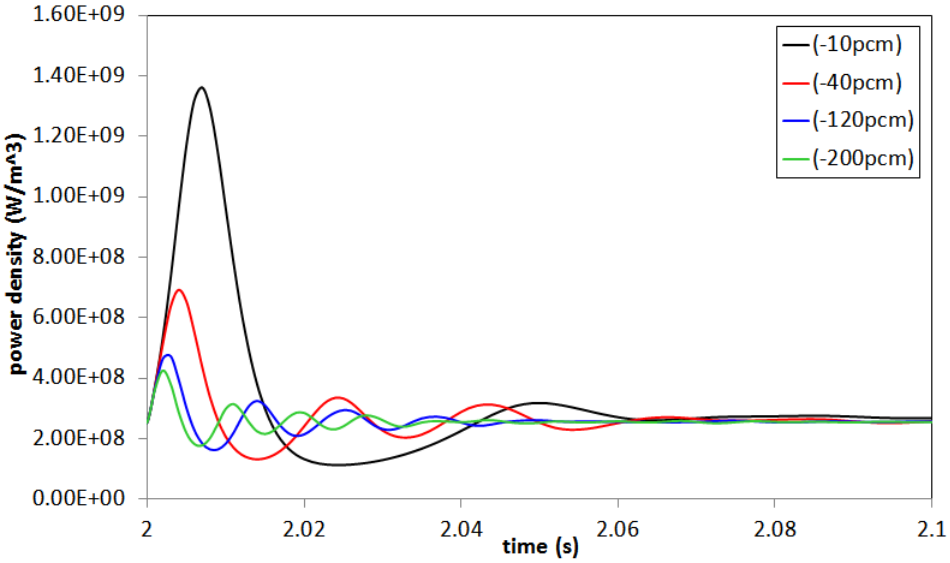


**Figure 5.17**: Responses of the average channel power density to 100pcm step reactivity insertion with different fuel temperature coefficients of reactivity feedback

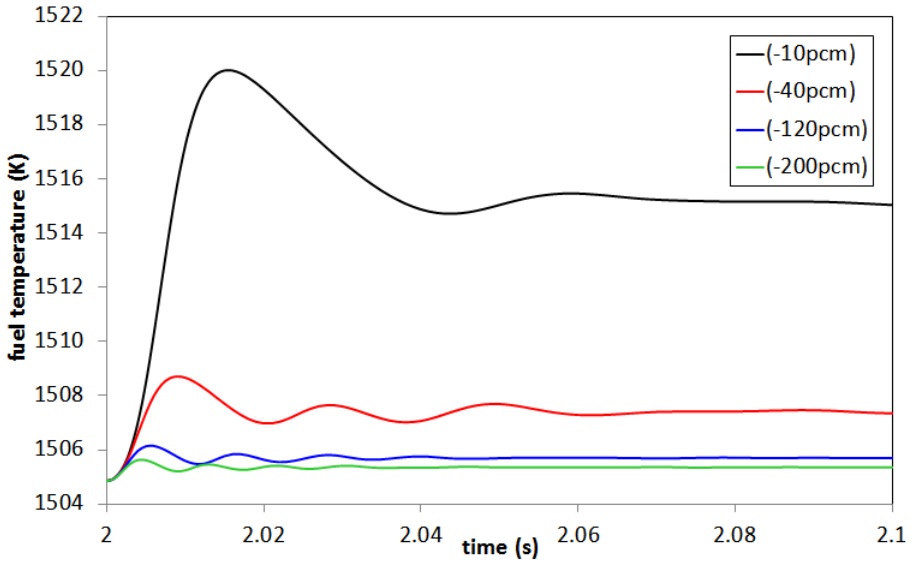


**Figure 5.18**: Power density responses to 100pcm step reactivity insertion with different fuel temperature coefficients of reactivity feedback

# Chapter 6

# Simulation Results and Analysis for DFR

In this chapter the previously built model was used to simulate several prototypic transients or accidents that may occur during the DFR's operation. Hereby the scenarios such as the step reactivity insertion, the pump transients and accidents and the boundary temperature transients were concerned. Among those situations the pump transients and accidents appear to be more interesting, for one thing because of the unique feature for the liquid-fueled reactor, namely the possible velocity-dependent power distribution, for another also because of the unique structure of the DFR concept, namely the dual-fluid exchanger-type reactor core, which means the power output is strongly velocity-dependent as well. Thus the main spaces of the current chapter were about the system responses to the abnormal operation in pumps. As said before, the simulations were parallel done on 10 single channels; each of those can represent the dynamic behavior of the subregions where they were located respectively.

## 6.1 Step Reactivity Insertion

In this section the system responses to a certain level of a step-wise insertions of reactivity were investigated. Here 200pcm reactivity step insertion was initialized after the system reached its equilibrium. This 200pcm reactivity is just a reference value [73] and specifically for the DFR system the step-wise reactivity insertion sometimes can be caused by the excess injection of the plutonium at the PPU, which is called the plutonium injection transient (PIT).

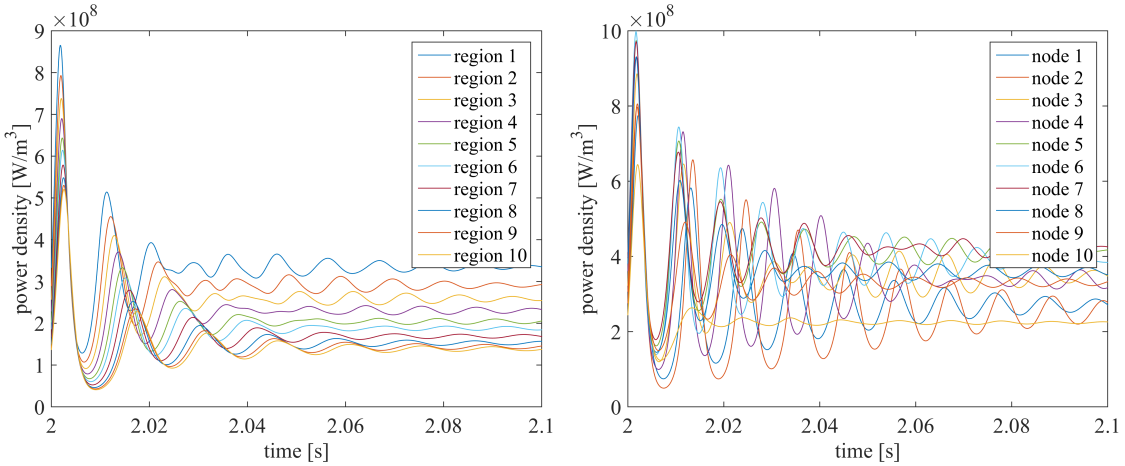


**Figure 6.1**: left: Average channel power density responses for 200pcm step insertion of reactivity from different core regions; right: Responses of the node power densities for 200pcm step insertion of reactivity for the channel located in the reactor core center (Region 1)

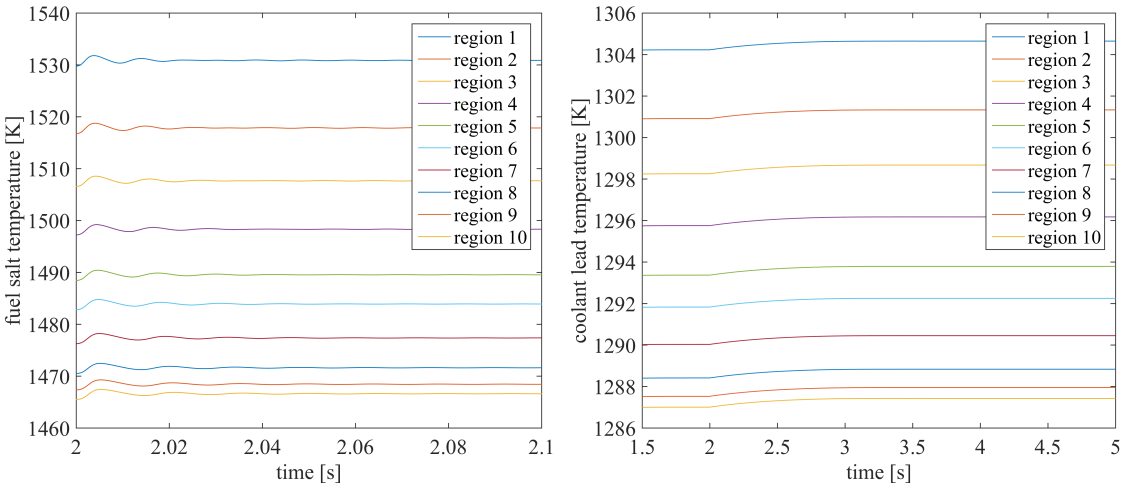


**Figure 6.2**: Average fuel salt temperature responses of channels for 200pcm step insertion of reactivity for different core regions (left); Average coolant temperature responses of channels for 200pcm step insertions of reactivity for different core regions (right)

Consequently, looking at Figure 6.1 and Figure 6.2, due to the short neutron generation time and the large temperature coefficient, the DFR showed a very sharp but short-lasting oscillation (Figure 6.1). The largest peak power, which was several times higher than the nominal power, appeared at the first cycle of the oscillation. However, this large peak power only sustained less than 0.01s and afterwards the

system rebuilt the new balance within 0.2s. Due to this very fast power transient combined with the thermal inertia of the working fluids, the fuel salt as well as the coolant lead had only a very smooth oscillation in temperature (Figure 6.2). Additionally, the "region 1" in the legend box in Figure 6.1(left) means the average power density for the whole single fuel channel, which is located in "region 1" (in the center). The "node 1" in the legend box in Figure 6.1(right) presents the power density of the single node at the bottom of the single fuel channel, which is located in "region 1". Therefore, the curve named "region 1" in Figure 6.1(left) is the average of all curves in Figure 6.1(right).

## 6.2 Pump Transients and Accidents

For the liquid-fueled reactor it can be the exclusive feature that the power production and distribution is also fuel-velocity-dependent. Specifically, assuming that the continuous flowing of the fuel salt is discretized into finite "batches" along the fuel salt circuit, then each "batch" has a hold-up time in the reactor core. This hold-up time can be neglected compared to the ultra-short time of the fission reactions, nevertheless, on another aspect it should be taken into account for the concentration of the delayed neutron groups. For instance, when the hold-up time is longer than the mean lifetime of a certain delayed neutron group, both the fission reaction and the decay will occur within the reactor vessel. In contrary, if the flow velocity of the fuel salt is fast enough to transport the precursors out of the reactor vessel before they decay, then the fission reactions take place inside the reactor vessel, but the decay power is delivered into the loop outside of the reactor core. With regard to the DFR it is difficult to find out the pure effect of the fuel velocity on the power production and distribution connected to the precursor drift. This is because the heat transfer between the fuel salt and coolant lead is likewise strongly dependent on the flow velocity of the fuel salt, which in turn also affects the reactor power.

Figure 6.3 and Figure 6.4 present the steady state power production and distribution influenced by the flow velocity of the fuel salt for the channel in the central region (Region 1). The "red25%" means the fuel salt velocity was reduced by 25% of the nominal value, while the "inc25%" means it was increased by 25% of the

nominal value. Figure 6.3 shows the absolute value of the power, while Figure 6.4 gives the relative power production referring to its mean value along the channel. As a result, the power production grew with increasing velocity due to the enhanced cooling thus giving positive reactivity feedback on power. On the other hand, the power went down with decreasing fuel velocity and the location where the peak power appeared was moved toward the exit of the core. This phenomenon can be explained probably in following aspects: first, with a very low velocity (e.g. 1% of the nominal value) the precursors are moving very slowly and the reactor runs roughly like a conventional PWR with static fuel rods, thus the power production in each node becomes only reactivity-dependent approximately; second, the power level with the low velocity is not sufficient to heat up the fuel, instead the fuel is being cooled by the liquid lead, so the fuel salt near the core exit has lower temperature, which finally gives larger positive reactivity feedback on power in those nodes.

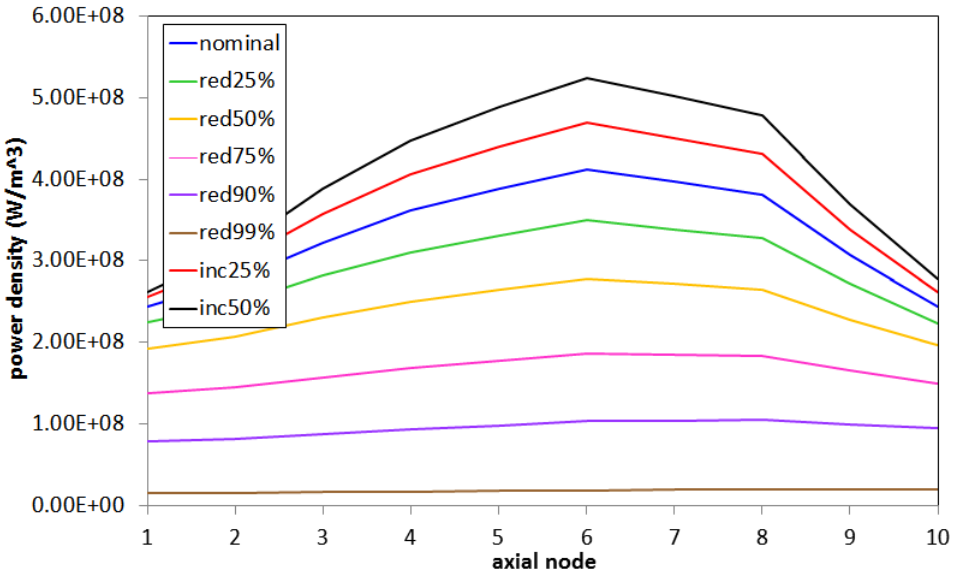


**Figure 6.3**: Power production and distribution at different fuel salt velocity

In the following parts several prototype pump transients and accidents were simulated. Herein relevant scenarios were considered, such as the pump shutdown accidents and the step change in flow velocity of the pumps, which usually can be induced by the fluctuation of the operating voltage.

As illustrated in Figure 6.5(left), Figure 6.6(left) and Figure 6.7(left), when the fuel

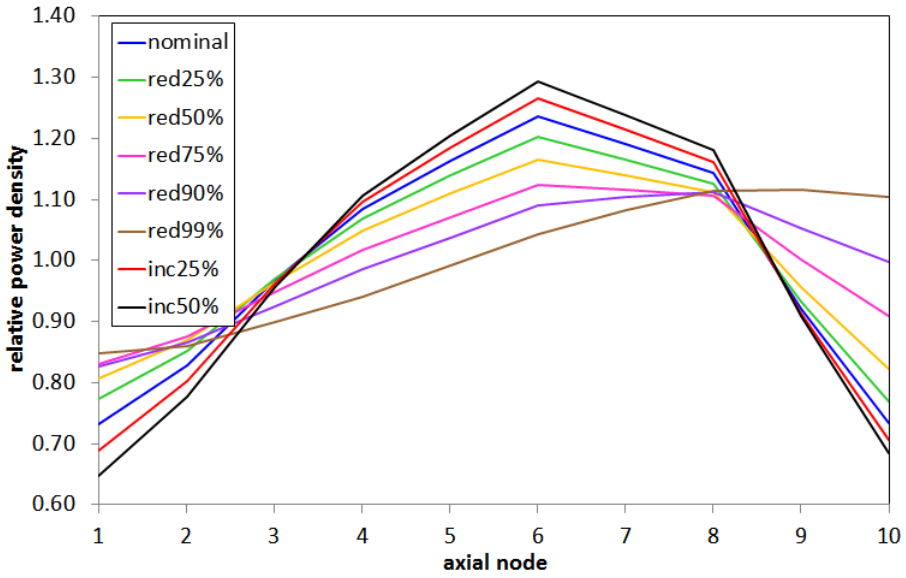


**Figure 6.4**: Relative power production and distribution at different fuel salt velocity

salt velocity decreased by 10% of its nominal value, the energy output including the enthalpy stream and the heat transfer decreased for the fuel salt system (Eq. 5.24(3)). As a result, the fuel salt temperature jumped up at the beginning (see the sub-plot in Figure 6.6) giving a negative feedback on power. Then the subsequent reduction of the reactor power reduced the energy input into the fuel salt system. Due to this counteraction, the change of the fuel temperature was almost insignificant during this transient. Besides, the coolant temperature declined, as the heat gained from the fuel salt was reduced but the enthalpy stream as the energy output remained roughly at the same rate for the coolant system (Eq. 5.24(4)).

A similar transient can also occur for the coolant pump. To this end the simulation of a 10% step reduction of the flow velocity for the coolant pump was performed. Consequently, the coolant temperature grew up with the decreasing enthalpy outstream (Figure 6.7(right)) and the fuel salt presented a temperature rise due to the less effective heat transfer (Figure 6.6(right)), which again gave a negative feedback on power (Figure 6.5(right)). Likewise, the effect of the weakened heat transfer was compensated by the power reduction leading to a negligible change in fuel temperature.

Additionally, the scenarios of 20% step increase of the flow velocity for both pumps

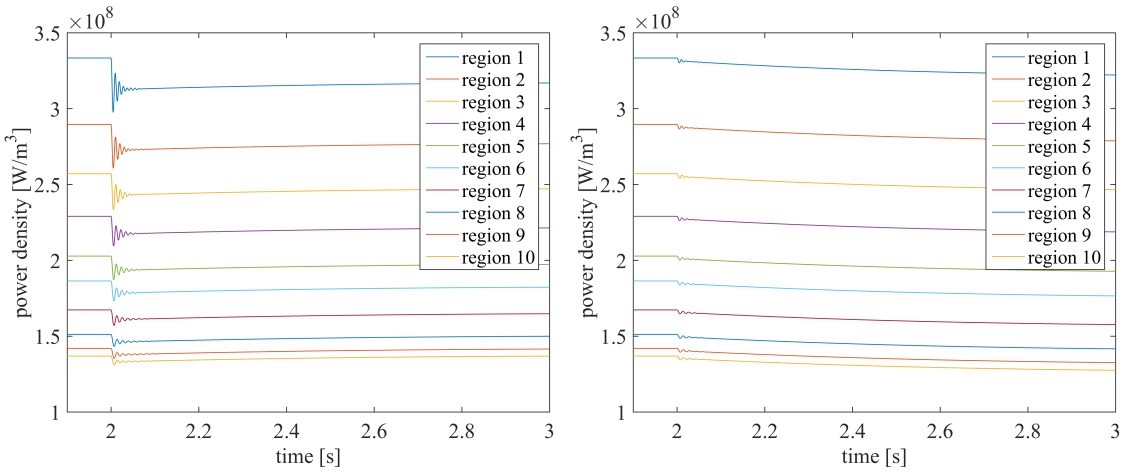


**Figure 6.5**: Average channel power density responses from different core regions for the 10% step reduction of the nominal flow velocity of the fuel salt (left) and of the coolant lead (right)

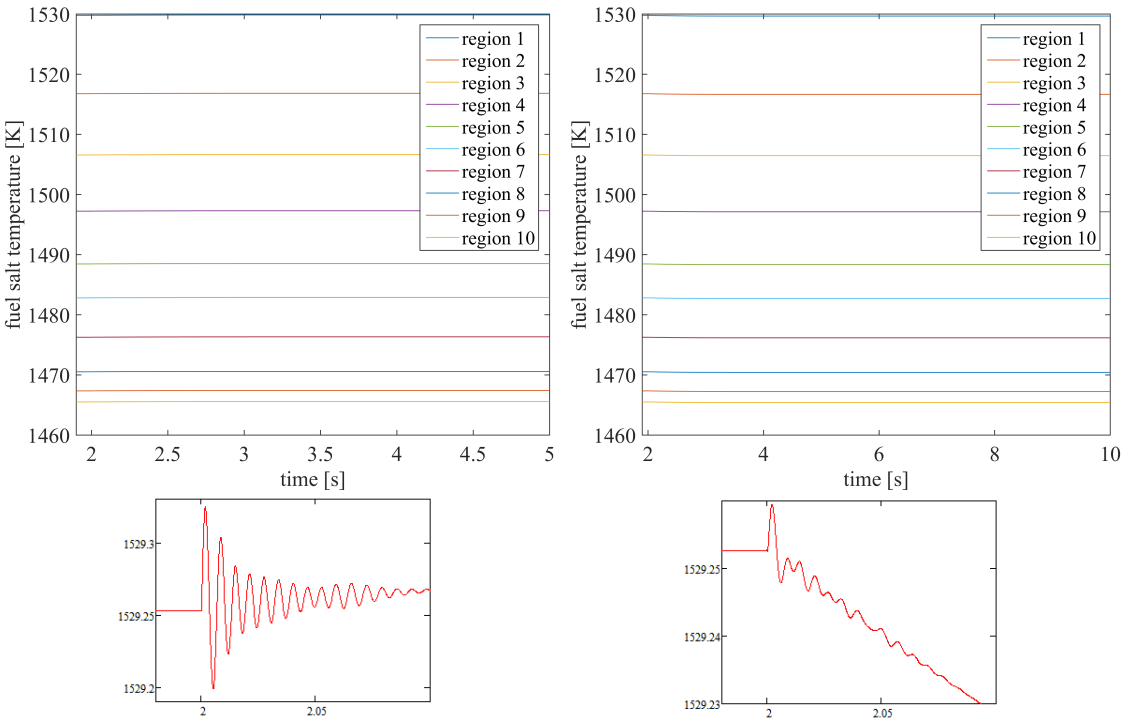


**Figure 6.6**: Fuel salt temperature responses from different core regions for the 10% step reduction of the nominal flow velocity of the fuel salt (left) and of the coolant lead (right)

were also concerned. These can be seen as over-cooling transients. Specifically, with growing fuel velocity, a temperature sink appeared in the fuel salt due to the enhanced heat transfer and the increasing enthalpy out-stream. Then the enhanced

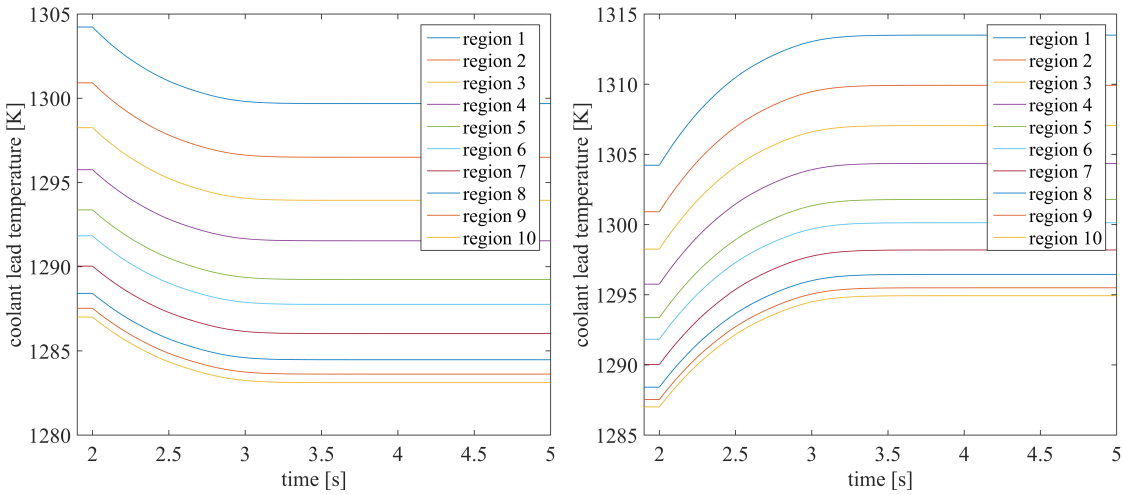


**Figure 6.7**: Coolant temperature responses from different core regions for the 10% step reduction of the nominal flow velocity of the fuel salt (left) and of the coolant lead (right)

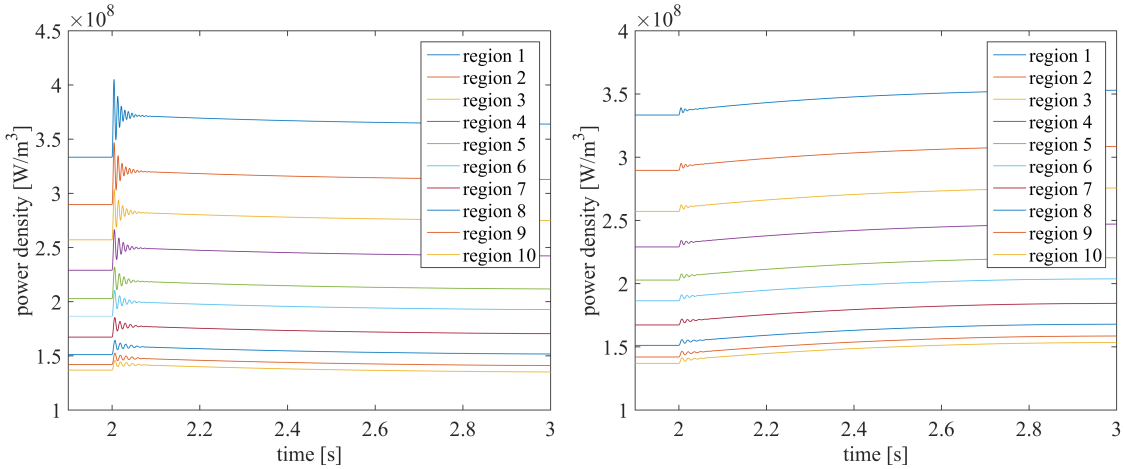


**Figure 6.8**: Average channel power density responses from different core regions for the 20% step increase of the nominal flow velocity of the fuel salt (left) and of the coolant lead (right)

heat exchange brought about a temperature rise in the coolant and the fuel temperature sink gave a positive feedback on power, which in turn counteracted the temperature drop of the fuel salt. For another aspect, the system responses to the transient with growing coolant velocity can be explained in like manner. The results were described in Figure 6.8, Figure 6.9 and Figure 6.10.

Furthermore, the simulation of the pump shutdown accident is of great importance for the reactor safety analysis. Regarding the DFR concept, it is more significant to

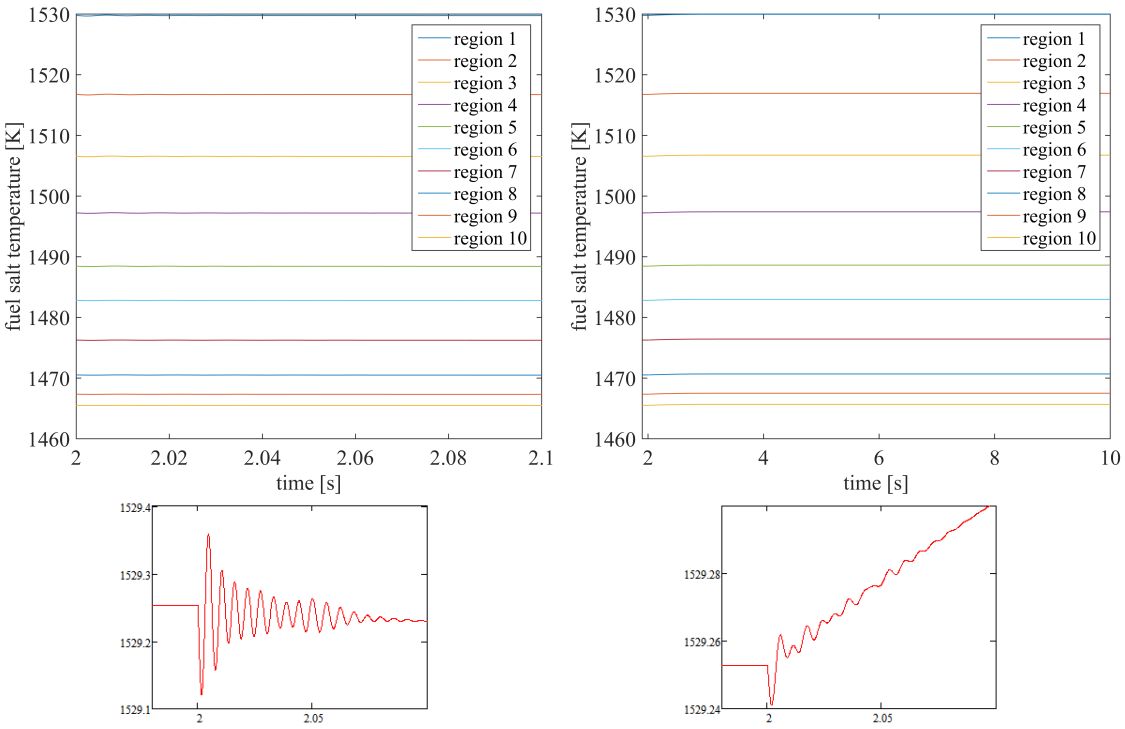


**Figure 6.9**: Fuel salt temperature responses from different core regions for the 20% step increase of the nominal flow velocity of the fuel salt (left) and of the coolant lead (right)

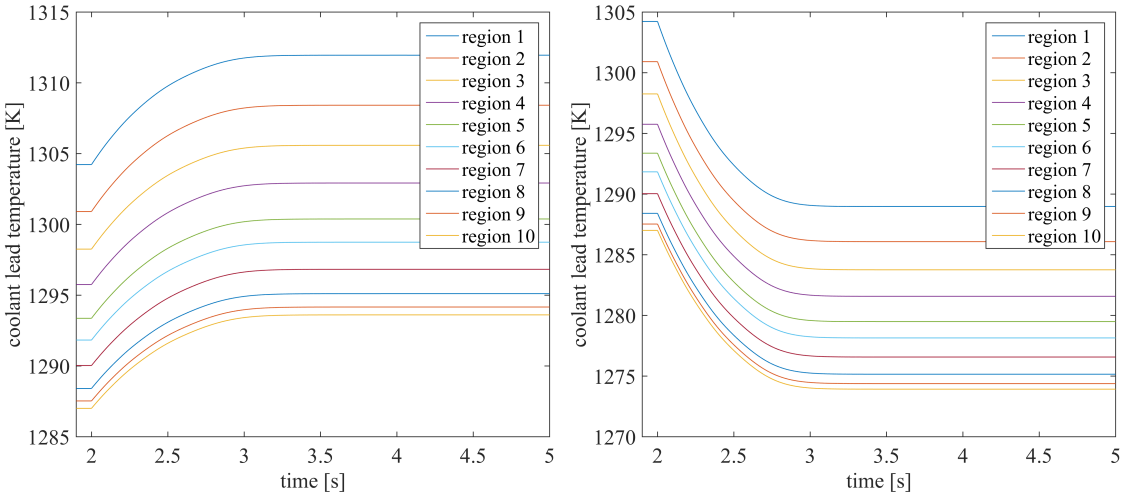


**Figure 6.10**: Coolant temperature responses from different core regions for the 20% step increase of the nominal flow velocity of the fuel salt (left) and of the coolant lead (right)

demonstrate its self-shutdown feature, since the DFR is potentially a reactor without control rod as foreseen in its reference design. For this purpose, three types

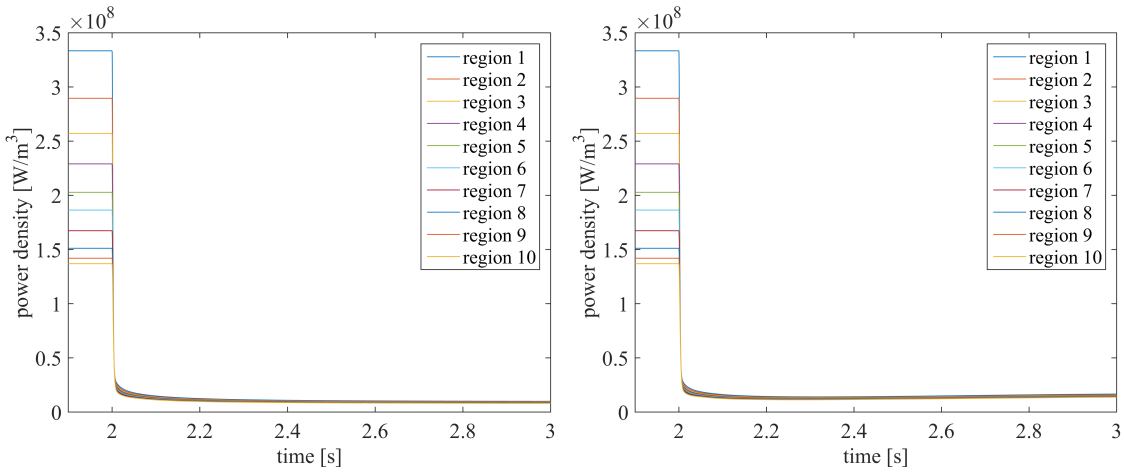


**Figure 6.11**: Average channel power density responses from different core regions for the TPS(left) and FPS(right) accident

of pump shutdown accidents were implemented including the two-pump shutdown (TPS), the fuel-pump shutdown (FPS) and the coolant-pump shutdown (CPS) accidents.

First, Figure 6.11(left), Figure 6.12(left) and Figure 6.13(left) described the results of the TPS accident. The reactor shuts down by itself and the power, for instance, in the central region (Region 1) fell down to less than 3% of the nominal power within just one second. Only a very smooth peak (less than 5K higher than the nominal value) appeared in fuel temperature, while the coolant was being heated up through the fuel tube wall and its temperature growth will end until the fuel and coolant reach their thermal equilibrium. Second, the evolutions of the power and the fuel temperature for the FPS accident look similar to the TPS accident, but the coolant temperature declined quickly and rebuilt its equilibrium at around 1181K. This is because during the FPS accident the energy output, namely the enthalpy out-stream for the coolant system (Eq. 5.24(4)), was still working.

The system responses during the CPS accident look different from others. The temperatures of the coolant lead went up quickly after the shutdown of the coolant pump (Figure 6.15), which indicates the reduction of the energy output of the coolant system from the thermodynamic point of view. Specifically, zero coolant velocity means that no heat can be removed from the coolant system. On the other hand, the responses of the fuel salt temperature vary from different reactor core regions. It

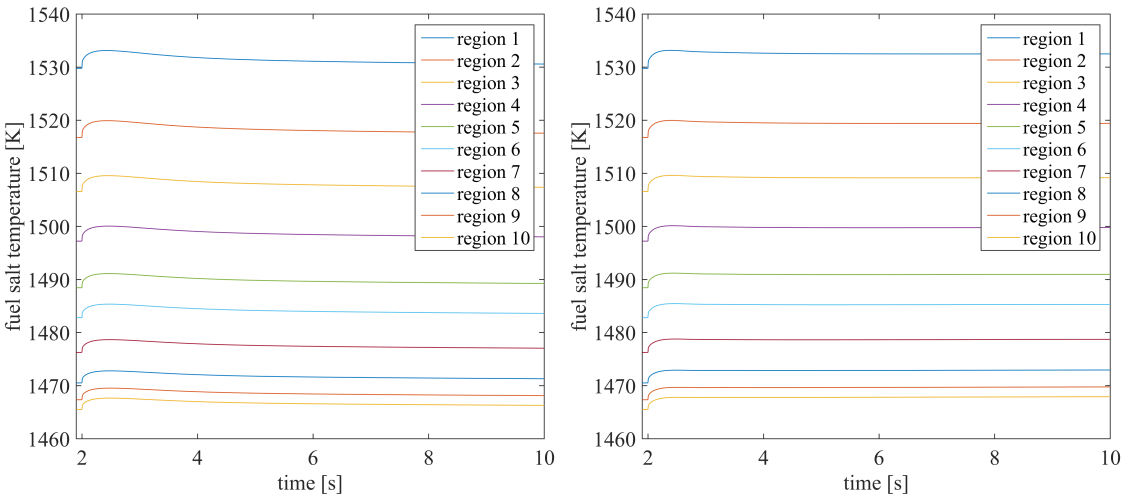


**Figure 6.12**: Fuel salt temperature responses from different core regions for the TPS(left) and FPS(right) accident

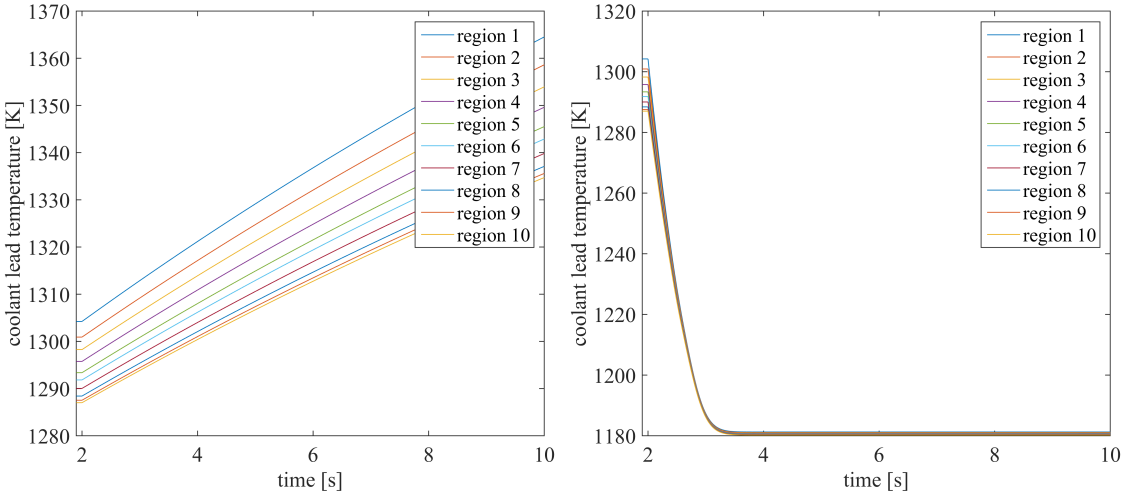


**Figure 6.13**: Coolant temperature responses from different core regions for the TPS(left) and FPS(right) accident

seems that the fuel temperatures of the region 5 to the region 10 increased relative rapidly and they converged to a certain temperature level, while the temperatures of the region 1 to the region 4 ended up at relative small rises. This phenomenon was caused by these reasons: first, the channel model is a open system with constant boundary conditions, which in this case means the constant inlet temperature of the fuel salt (1500K). As seen in Figure 6.14(right), the average steady-state temperatures of the fuel salt from the region 4 to the region 10 are actually lower than the fuel entrance temperature. Those regions are called "cold zones", where the fuel salt is being cooled by the coolant lead instead of being heated up by the

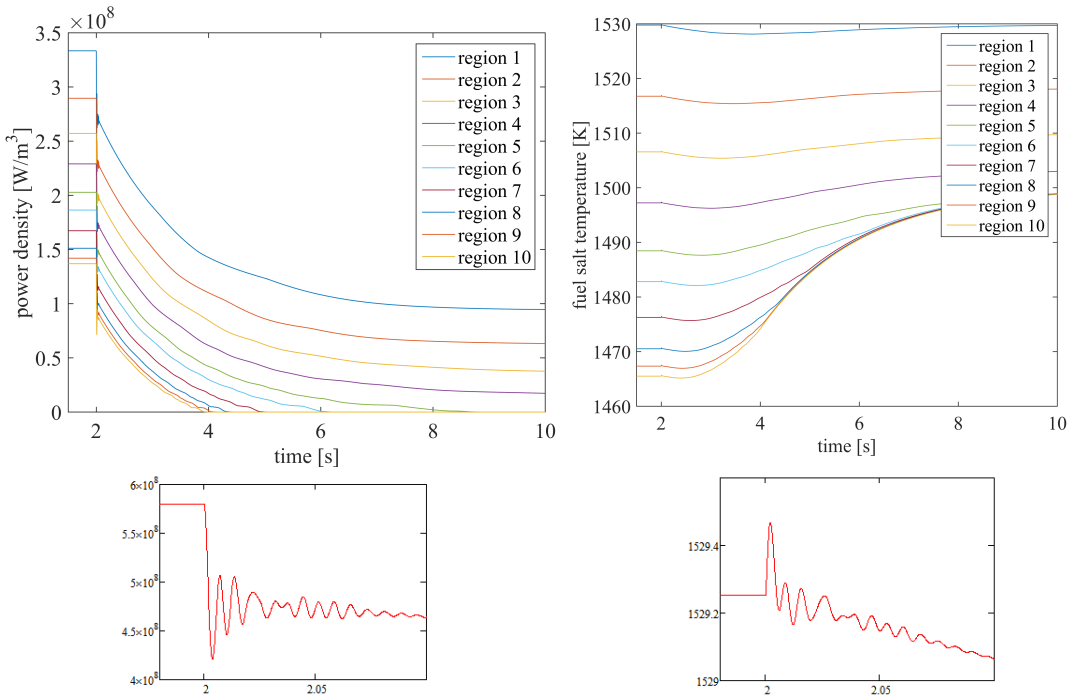


**Figure 6.14**: Average channel power density responses from different core regions for the CPS accident (left): Fuel salt temperature responses from different core regions for the CPS accident (right)

fission power. This is the consequence of the attenuated neutron flux along both the radial and axial directions, which induces that the fission powers in certain zones are not sufficient to increase the fuel temperature comparing to the strong cooling by the liquid lead due to the large temperature gradient (>300K) at the reactor core entrance. Therefore, during the CPS accident the cooling effect of the liquid lead was enormously reduced and as a result, the average fuel temperatures in these regions were increased obviously. In addition, the power in the cold zone fell down to nearly zero (Figure 6.14(left)), which was clearly caused by the extremely large negative temperature feedbacks in those zones. Finally, it seems that in the center regions of the reactor core (region 1 to region 3) there was no significant shutdown behavior, which was a result of the relative small negative temperature feedbacks in these regions. Generally, the simulation result of the CPS accident may remind us something in the aspect of the reactor safe shutdown for instance to take extra corrective actions such as the poison injection.

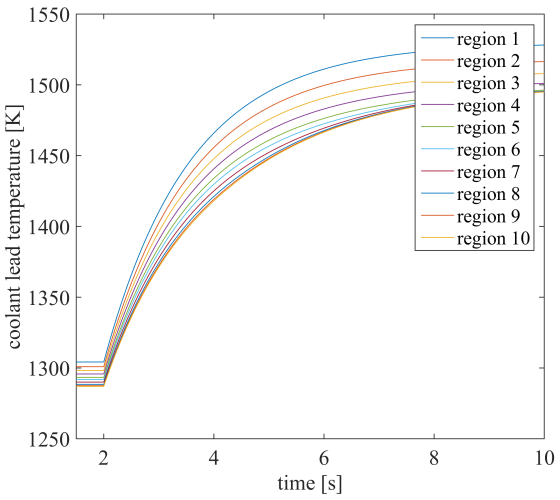


**Figure 6.15**: Coolant temperature responses from different core regions for the CPS accident

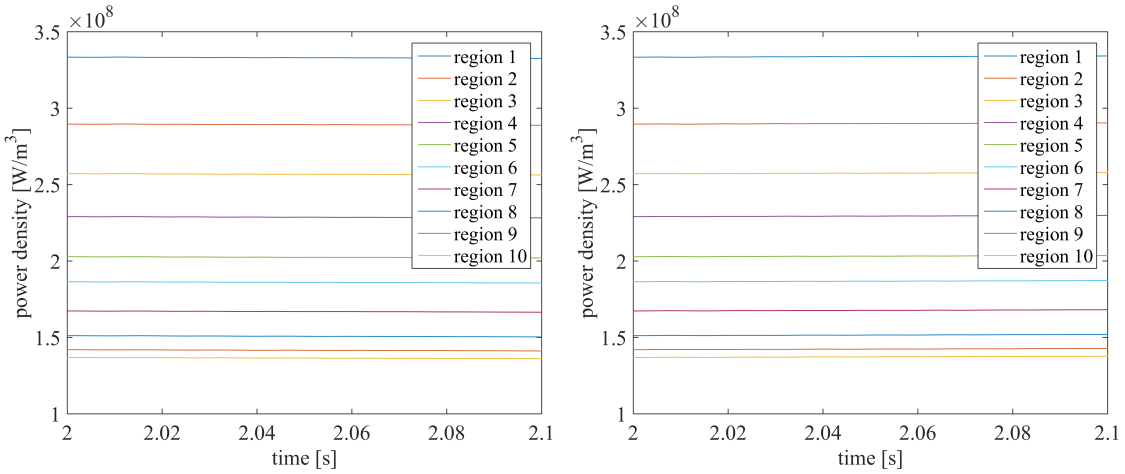


**Figure 6.16**: Average channel power density responses for the transient of an increasing (left) and a decreasing (right) inlet temperature of the coolant lead with a rate of 5K/s

## 6.3 Coolant Inlet Temperature Transients

Another type of the transient simulation of interest is the coolant inlet temperature variation transient, which means that the coolant inlet temperature can be a function of time. This simulation also makes sense from the point of view of the reactor operation, because it can be seen as a demonstration for the load-following feature of the DFR. For this purpose, a constant rate with ±5K/s was added to the coolant inlet temperature. This transient started at 2s and lasted for about 5s in total. Afterwards, the coolant temperature remained at the current value instead of falling

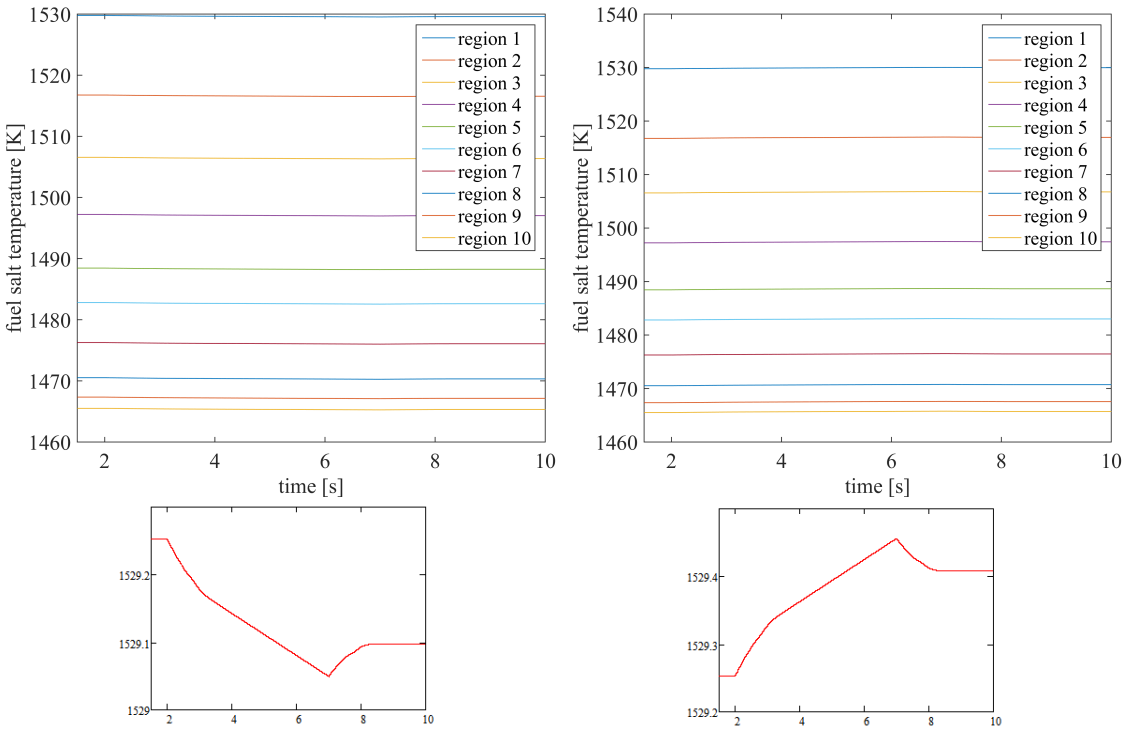


**Figure 6.17**: Fuel temperature responses for the transient of an increasing (left) and a decreasing (right) inlet temperature of the coolant lead with a rate of 5K/s

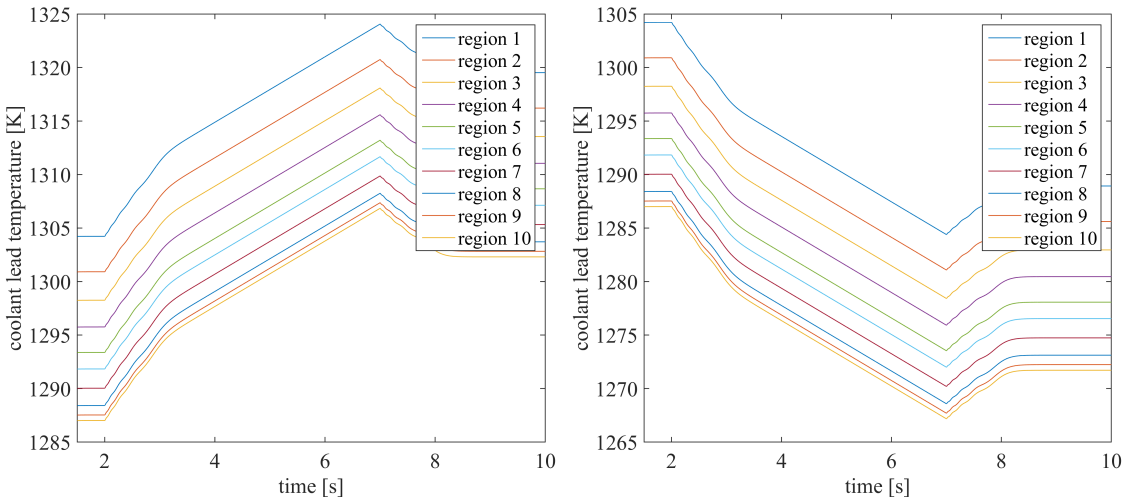


**Figure 6.18**: Coolant temperature responses for the transient of an increasing (left) and a decreasing (right) inlet temperature of the coolant lead with a rate of 5K/s

back to the nominal operating temperature. Consequently, the increasing coolant inlet temperature produced a negative feedback on power, which was going down during the whole transient (Figure 6.16). After the ramp increase of the coolant temperature ended, a power recovery was observed and the system rebalanced it-

self within less than two seconds. This power recovery happened, because the fuel temperature slightly decreased during the transient (sub-plot in Figure 6.17), leading to the generation of positive reactivity at the same time. In contrary, with the decreasing coolant inlet temperature, the system responses look just symmetric as the previous ones, which were considered as a predictable and reasonable result.

# Chapter 7

# Other Researches about MSR

Except the main works stated in the previous chapters (*Chapter 2* to *Chapter 6*), some extended demonstrations have been done to find out the possibilities of applying the current methodologies for the simulations of the MSRs. These demonstrations include:

1. Further simulations of the reactivity initialized transients for the MSRE using the TRACE model built in *Chapter 2* and *Chapter 3*;
2. Steady-state coupled-physical simulation for a graphite-moderated MSR using TRACE and SERPENT;
3. Preliminary study on the TRACE's suitability for the simulation of the DFR concept.

## 7.1 Further Simulations of the Reactivity Initialized Transients for the MSRE

These simulations were done with the exactly same TRACE model for the MSRE using $^{233}$U-based fuel. Although these scenarios were not considered in the ORNL's work, it still makes sense to perform these simulations in order to find out more features of this reactor type.

For instance, Figure 7.1 presents the relative power responses, when the ramp reactivity was added with the same amount but with different rates. The results shows that with higher rates of the ramp insertion double-peak or even triple-peak appeared in the power responses. On the other hand, Figure 7.2 proves the long-term

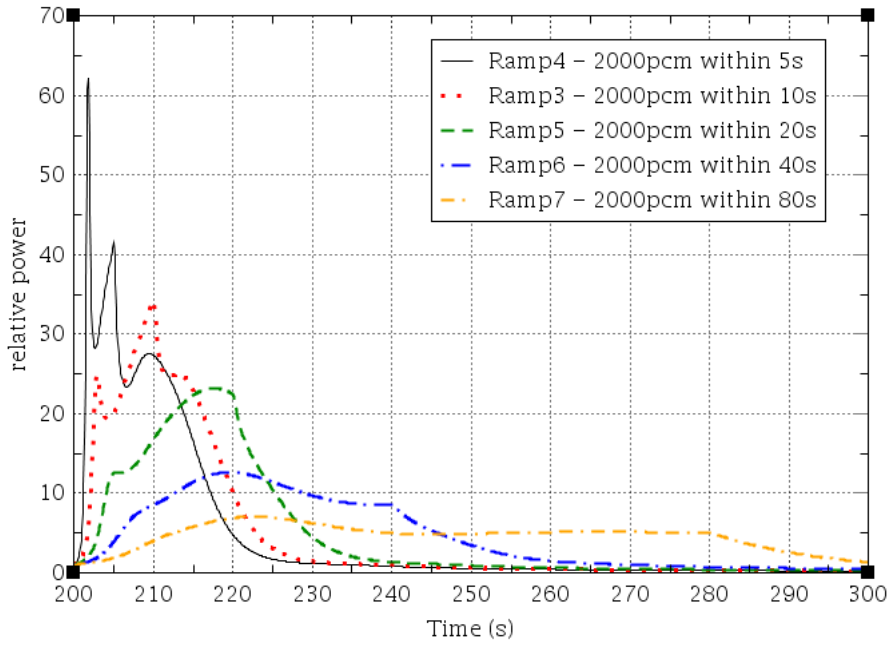


**Figure 7.1**: Relative power responses to the ramp reactivity insertions of different rates at 10M

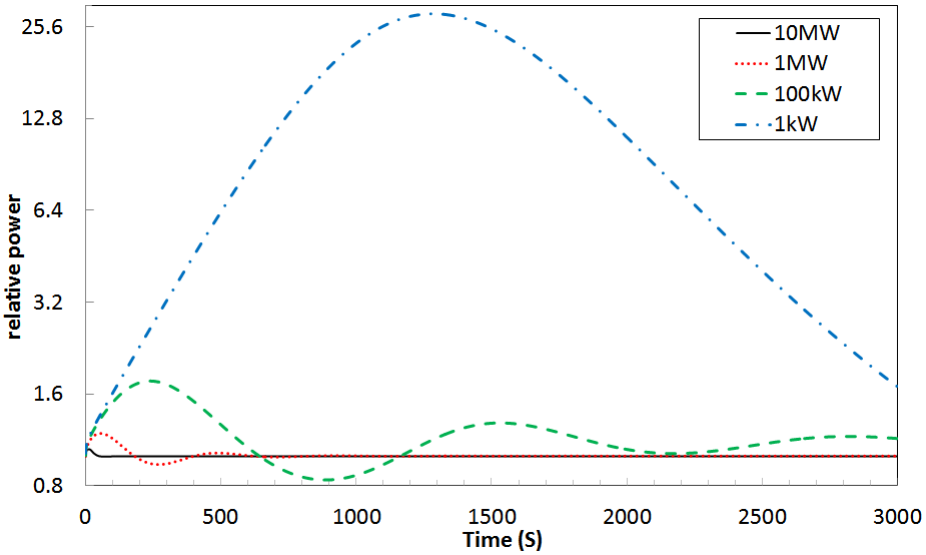


**Figure 7.2**: Relative power responses to the 10pcm step-wise reactivity insertions at different power levels

perturbation at low power level for the MSRE, which was already stated in the ORNL's reports. It is clear that at lower power level it took obviously a longer time for the system to be re-stabilized and moreover, the power transient became much more larger than its initial value. These two simulations can provide the future

studies on similar reactor concepts with a reliable benchmark and from the point of view of the reactor operation safety it is also important to consider the corresponding safety actions against those unexpected situations.

## 7.2 Steady-state Coupled-physical Simulation for a Graphite-moderated MSR

In this section a collaborative work was presented that is to use TRACE coupled with an external Monte Carlo code SERPENT to implement a steady-state simulation for the MSR. Herein a small graphite-moderated MSR (GMSR) prototype was developed. It has a similar design to the MSRE, which means the reactor core is filled by the hexagonal graphite prisms with a fuel channel in the center for each prism (Figure 7.3). GMSR is also using the same salt mixture as the MSRE, namely the $^{7}$LiF-$BeF_2$-$ZrF_4$-$UF_4$ salt. The design data is given in Table 7.1. Similar to the approach of doing the coupled criticality calculation for the DFR in *Chapter 5*, the thermal-hydraulic model of the GMSR core was built by TRACE with 6 independent subregions, each of these has the thickness of 0.5m, 0.5m, 0.25m, 0.15m, 0.05m and 0.025m respectively from the center to the periphery and each subregion was further split into 15 nodes in the axial direction (Figure 7.4). Furthermore, the flow distributor was developed to guarantee each subregion with different flow area to have the same fuel flow velocity. This can be realized by splitting the total mass flux according to the fractional flow area of each subregion. On the other hand, the graphite prisms were equivalently built by the "*Heat Structure*" of the TRACE code with the same total volume as designed. The SERPENT model has the same nodalization as the TRACE model, which means 90 "detectors" were built in the SERPENT model and each "detector" holds the same fuel-moderator ratio as the TRACE model.

The iteration was performed with following procedures:

1. SERPENT produced the fission rates for each node with the initial node temperatures and densities and the fission rates were converted into node powers;
2. A data communication code (DCC) was developed to read the node powers and to rewrite the "*Fluid Power*" in the TRACE input file;

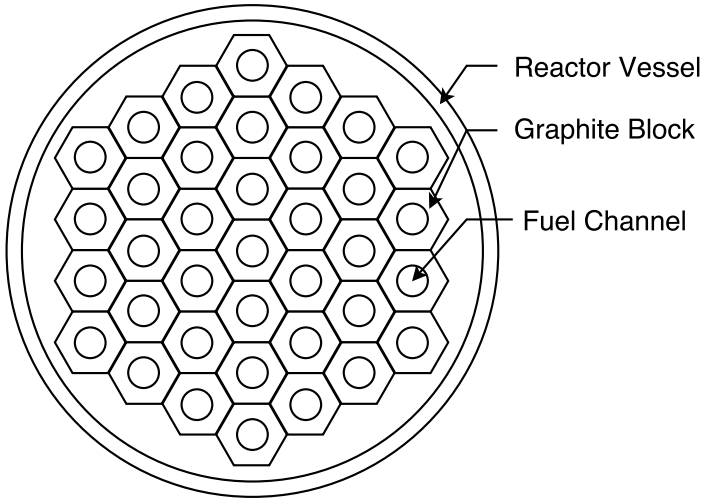


**Figure 7.3**: Scheme of the GMSR concept

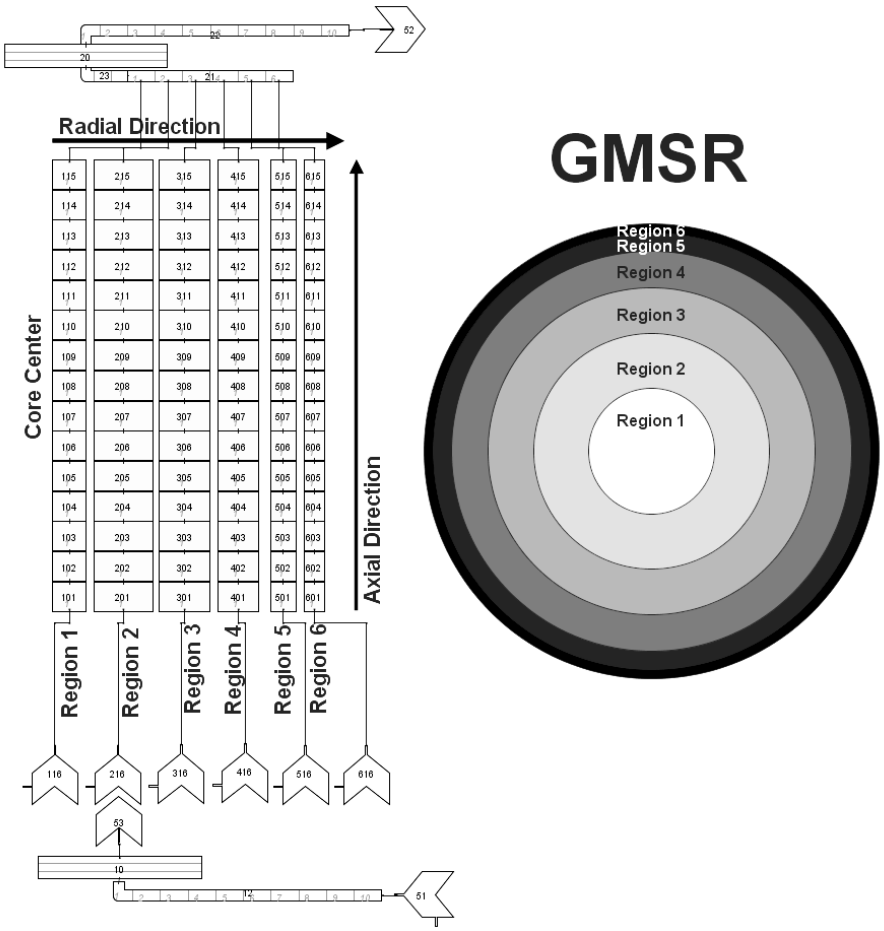


**Figure 7.4**: Nodalization of the GMSR core model with TRACE

**Table 7.1**: Design data of the GMSR

| item | value | unit |
|---|---|---|
| reactor core radius | 1.5 | m |
| reactor core height | 3 | m |
| graphite reflector thickness | 0.5 | m |
| fuel channel radius | 0.017 | m |
| hexagonal inner radius | 0.07 | m |
| number of full-size channels | 401 | – |
| reactor thermal power | 35 | MW |
| fuel inlet temperature | 900 | K |
| fuel outlet temperature | 950 | K |
| total mass flux of the fuel salt | 300 | kg/s |

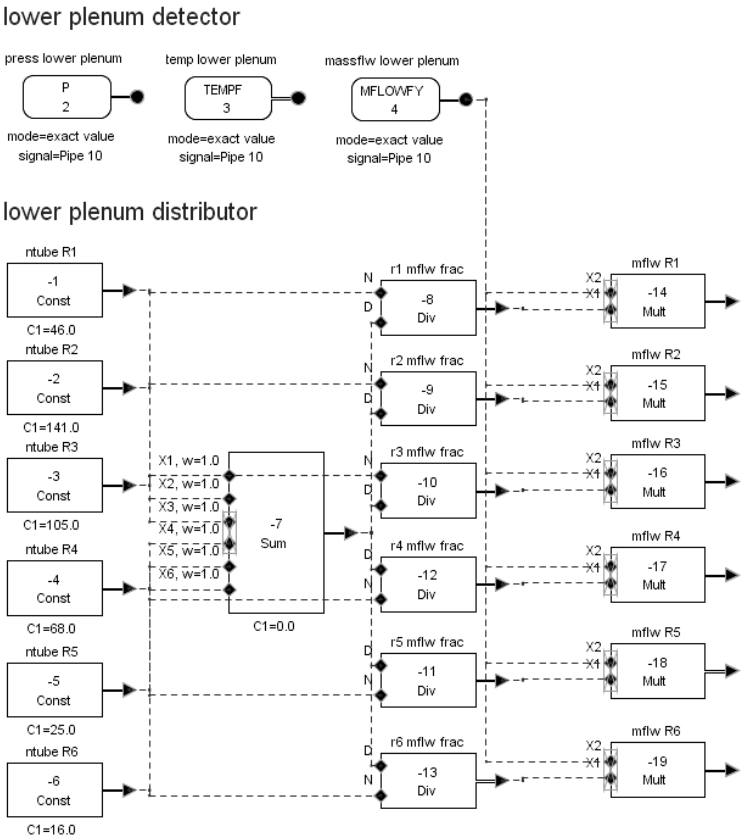


**Figure 7.5**: Control system of the GMSR flow distributor

3. TRACE calculated the temperatures for each node and these new temperatures were read by the DCC module and were compared with the initial temperatures. If the error converges, TRACE outputs the final result. Additionally, the fuel salt composition was also finely tuned during the simulation in order to obtain a proper $k_{eff}$ value.

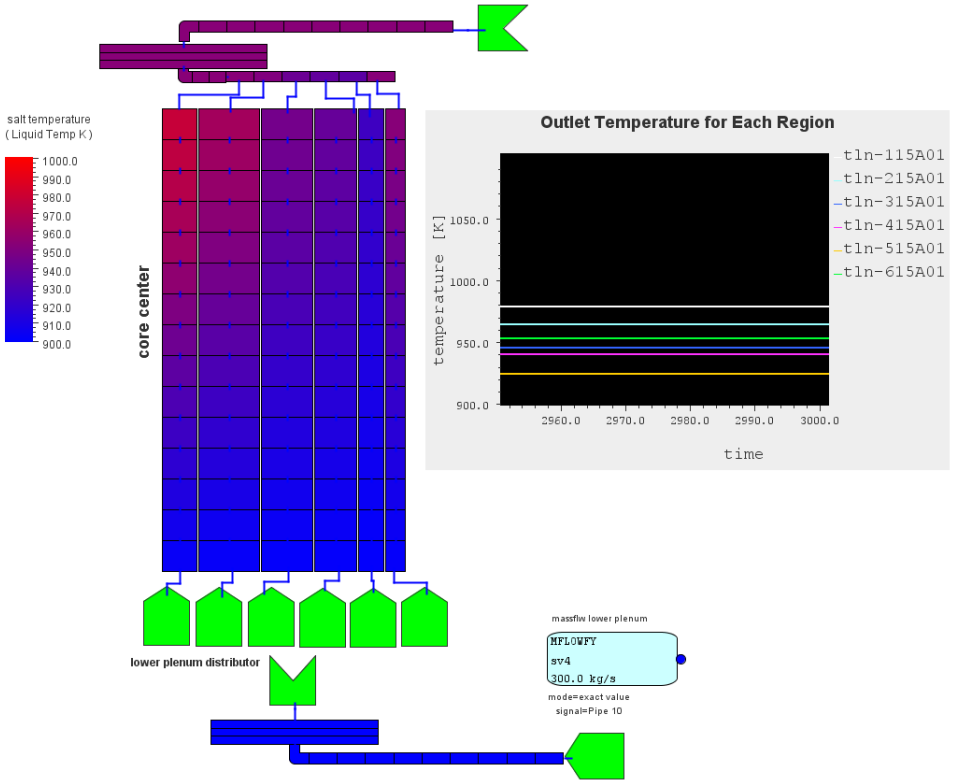


**Figure 7.6**: Steady-state Temperature distribution through the GMSR core

Consequently, a reasonable temperature distribution was produced by TRACE (Figure 7.6), because a similar result can be found in the reference study [66]. Additionally, it was observed that the temperature in "region 6" is higher than the one in "region 5". This is because the SERPENT has a reflector outside, which induced larger neutron flux in "region 6" than in "region 5".

Generally, the goal of this study is to find the possibility of doing the coupled-physical simulations with a new combination of the current codes. The result proves the feasibility of performing the simulation for the steady state by coupling a 1D system code like TRACE to a Monte Carlo code like SERPENT. It enables the description of the power or the temperature distribution through the entire core, which is considered relatively difficult so far, because for the MSR with the multi-channel design (usually thousands of or even more channels) it is computationally too heavy-loaded when applying a 3D CFD code coupled with a Monte Carlo code or a neutron diffusion code.

## 7.3 Preliminary Study on the TRACE's Suitability for the Simulation of the DFR Concept

The feasibility of using TRACE for the DFR's simulation was also investigated. With the same approach of adapting TRACE for the MSRE's simulation, the "circuit solver" (Figure 7.7) built by "Control Blocks" to solve the point-kinetic equations and a simplified thermal-hydraulic model were constructed in TRACE (Figure 7.8). For this time the "circuit solver" was improved, which means the circuit was built based on 4th order of the *Taylor Series* that can produce more accurate result than the FEU method. On the other hand, the hydraulic models of the "fuel tube bundle" and the "coolant flow channel" in Figure 7.8 were sliced into 15 axial nodes and each model has the same hydraulic diameter as well as the same flow area as their design data in order to have the same fluid conditions during the simulation. The design data is listed in Table 7.2. Furthermore, the DFR was operated with the liquid lead as the coolant and with the similar liquid fluoride fuel used in MSRE, however, the typical fuel vector of the SNF from the commercial LWRs was extra introduced into the carrier salt. Hence, the main job of this section is to find the possibility of operating SNF for the DFR concept. The point-kinetic parameters were derived by SERPENT and is listed in Table 7.3, where the temperature coefficient was averaged from Table 2.8.

**Table 7.2**: Design data of the DFR for the demonstration of the TRACE code

| item | value | unit |
|---|---|---|
| reactor core diameter | 3.0 | m |
| fuel tube diameter | 0.094 | m |
| inner radius of the hexagonal | 0.05 | m |
| thickness of the fuel tube | 0.001 | m |
| number of fuel tubes | 816 | – |
| reflector thickness | 0.5 | m |
| reactor thermal power | 240 | MW |
| fuel inlet temperature | 973 | K |
| coolant inlet temperature | 850 | K |
| flow velocity of the fuel salt | 2.3 | m/s |
| flow velocity of the coolant | 5.0 | m/s |

The results were illustrated in Figure 7.9, which gives a reasonable and typical power transient during the step insertion of reactivity. Therefore, the applicability of the

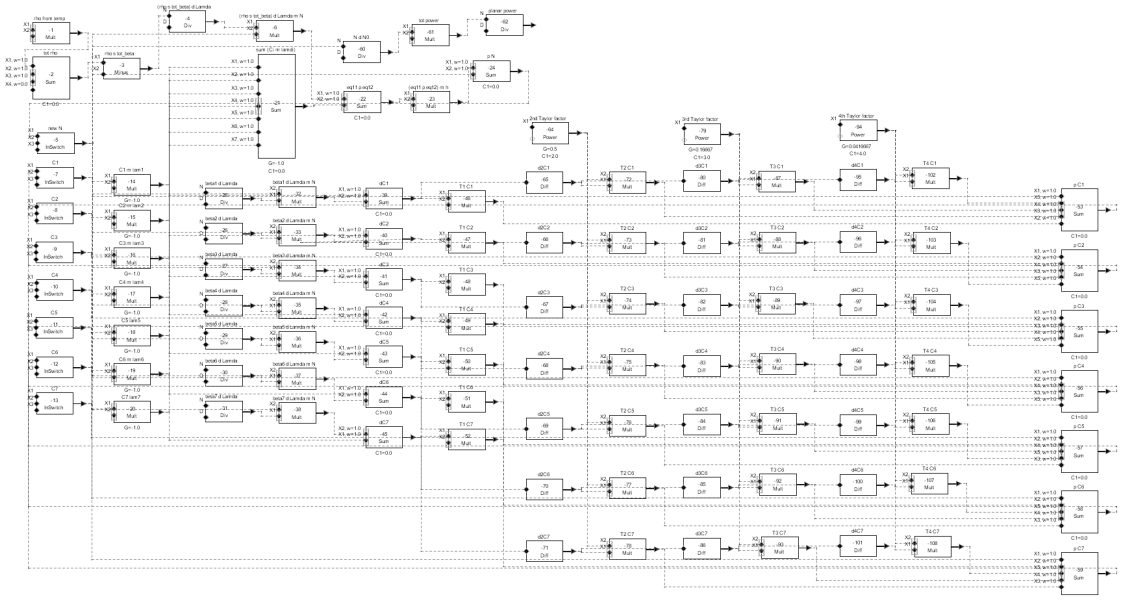

**Figure 7.7**: Circuit solver with 4th order of Taylor Series

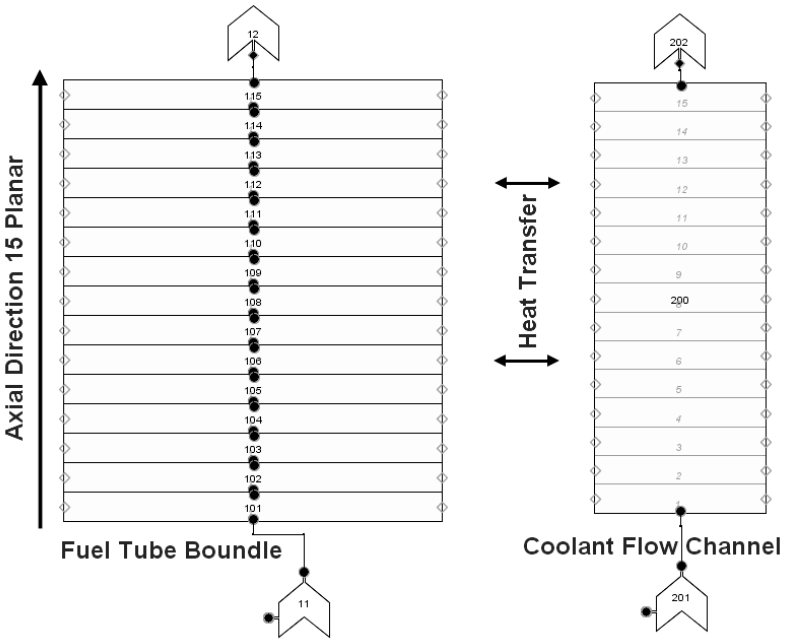


**Figure 7.8**: Thermal-hydraulic model of the DFR built with TRACE

methodology of adapting the modified TRACE code for the MSRE's simulation was demonstrated to be suitable for the DFR's simulation. However, as mentioned in *Section 5.2.4* the "circuit-solver" based on the explicit numerical method has the risk to cause the numerical instability when solving the stiff point-kinetic equations and building an implicit solver with high order looks very difficult based on the approach

**Table 7.3**: Point-kinetic parameters for the DFR obtained from SERPENT calculation

| item | value | unit |
|---|---|---|
| decay constant of DNP group 1 | 0.0126 | 1/s |
| decay constant of DNP group 2 | 0.0300 | 1/s |
| decay constant of DNP group 3 | 0.1093 | 1/s |
| decay constant of DNP group 4 | 0.3154 | 1/s |
| decay constant of DNP group 5 | 1.1940 | 1/s |
| decay constant of DNP group 6 | 4.3763 | 1/s |
| delayed neutron fraction group 1 | 8.09E-5 | – |
| delayed neutron fraction group 2 | 6.27E-4 | – |
| delayed neutron fraction group 3 | 4.76E-4 | – |
| delayed neutron fraction group 4 | 1.04E-4 | – |
| delayed neutron fraction group 5 | 3.32E-4 | – |
| delayed neutron fraction group 6 | 8.72E-5 | – |
| prompt neutron life time | 3.33E-6 | s |
| temperature coefficient of reactivity | -10 | pcm/K |

of the current "circuit solver". Therefore, to externally couple TRACE with a more robust ODE-solver for the point-kinetic equations or the neutron diffusion equations should be one of the key points of the future work.

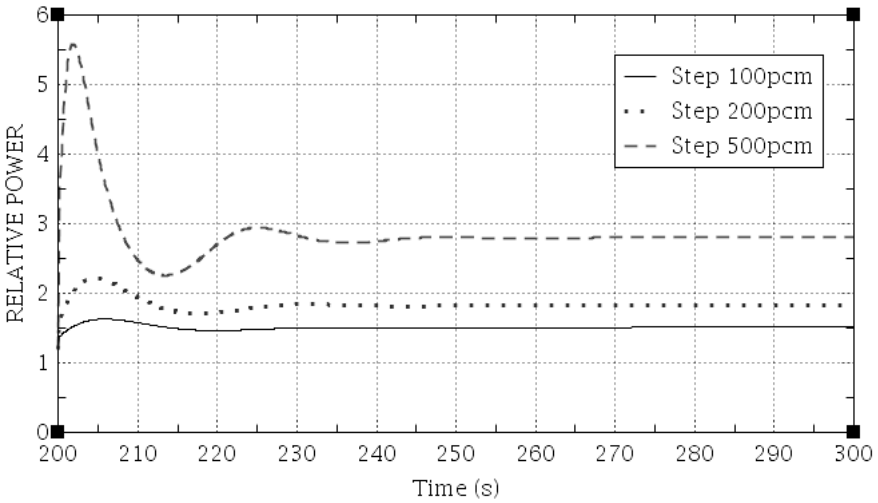


**Figure 7.9**: Relative power responses to different step-wise insertions of reactivity

# Chapter 8

# Conclusion

Generally, this thesis has presented the achievements of the two main projects about the molten salt reactor (MSR) in the framework of the Ph.D. program in the past three years. The first project was basically about the validation of the current computer code for an old MSR design (MSRE), while another one was all about fundamental and theoretical calculations for a completely new MSR concept (DFR). Recently it seems that MSR draws a great interest throughout the academia and industry. It happens because MSR can promise foreseeable or even technically proven advanced safety features, which are difficult for the current commercial light water reactors (LWR) to achieve. As known, the LWR is dominant all over the world at the moment, partly because the working fluid, namely the water, is one of the best-known working fluids for the industry. The thorough understanding about water reduces the uncertainty of the reactor operation, which somehow improves the reactor safety. However, on the other hand, the water in the LWRs has to be pressurized up to 15MPa (PWR) or 8MPa (BWR) to reach high liquid temperature in order to achieve sufficient heat removal and the commercial power production. Thus the existence of the high pressure vessels in the LWR system is permanently a potential risk of radioactive leakage and explosion. Second, the phase change of the water (liquid to gas) is principally unfavorable inside the reactor vessel, because it is connected to the over heating of the fuel rod cladding. Moreover, the avoidance in water caused by the evaporation reduces the moderator's efficiency leading to worse neutron economy and fuel utility. In recent years the design of the LWRs especially the PWRs of generation III has made a remarkable progress in their safety system, which is called the "Passive Safety System", for instance, the passive residual heat removal system (PRHRS). Although this system can nearly prevent the reactor from

the core melting accident in any case, but it is not able to reduce the probability of this accident down to zero. From this point of view the MSR opens the possibility to thoroughly eliminate the core melting accident, which the LWRs always face as the hugest challenge. In other words, the MSR is inherently safe in this respect. Additionally, the MSR can be operated at a very low pressure, for instance, 0.2 to 0.5MPa or even at the atmospheric pressure. This can enormously reduce the damage of the reactor explosion, when extreme accidents occur. Other advantages of the MSR can be found in *Chapter 1*.

In the following parts all the other chapters were reviewed and concluded. The perspectives were given in the last paragraph.

**TRACE Validation for the MSRE**

The discussion of adapting TRACE for the MSRE's simulation was started in *Chapter 2*. The first part of this chapter introduced the universal R&D approach for the MSR's study, which was called ND-TH (Neutron Dynamics - Thermal-Hydraulics) coupling method due to the strongly interwoven properties existing commonly in the MSRs. For the preliminary study, the neutron diffusion equations were reduced to the modified point-kinetic equations considering the precursor drift. Besides, the second part of *Chapter 2* presented the methodology of adapting TRACE for the MSRE in detail. This work was divided into two parts: to build new ODE-solver for the point-kinetic equations and to embed the molten salts into the fluid library. Specifically, The derivation of the forward Euler (FEU) method was opted to build the new ODE-solver with "Control Blocks". Using FEU method was based on the consideration of the balance among the system complexity, time efficiency and the computational accuracy. Moreover, some mathematic verification was done previously in order to support the selection of the proper numerical solver. On the other hand, embedding new working fluids meas the necessity of the source code modification. For this purpose, the fluid-property-related subroutines were found and the temperature-dependent properties of the two former working fluids, namely the lead-bismuth and sodium, were replaced by the new formulas.

*Chapter 3* mainly focused on the description and modeling approaches for the main

components of the MSRE system. As the TRACE is basically a 1D thermal-hydraulic code and some components in the MSRE system had unconventional structures or special features, these components had to be built in the equivalent way.

The simulation results as well as the analysis was given in *Chapter 4*. The aim of this part was trying to reproduce the results of the ORNL's simulations done in 1960s. To this end, several same or similar scenarios were investigated. Consequently, TRACE showed in general good agreements with the ORNL's results and the errors appeared were predictable and acceptable. This means the validation of the TRACE code for the MSRE succeeded. Additionally, successful reproduction of the ORNL's simulations and experiments proved the safety features of the MSRE such as the self-regulating against the reactivity accidents and the good shutdown safety.

**Preliminary Study on the DFR**

In the second part of this thesis, a preliminary dynamic analysis about the DFR was presented. The so-called multi-physical modeling approach was also introduced, as most MSRs share a common characteristic, which is the strongly-coupled neutronic and thermo-hydrodynamic properties of the materials. The simulation results give a basic understanding about the operating features and transient responses of the DFR concept.

Since the DFR project is still in the phase of the conceptual design, the reactor geometry was estimated previously. Then the 10×10 nodalized reactor core model was built with SERPENT and MATLAB for the neutronic and heat transfer calculation respectively. Thereafter, the coupled criticality calculation was performed to show the basic feasibility of this reactor concept. Related to this, the existence of a daily-operated PPU was postulated, which means the criticality value was expected to be slightly above 1. From this point of view, the fuel vector producing the most reasonable $k_{eff}$ was selected as the optimized fuel vector for the further investigation. On the other hand, an even more important purpose of this criticality calculation was to output the point-kinetic parameters as well as the steady-state conditions for the following transient simulations.

The study of the dynamic behavior focused on the single fuel channel including the domains of the fuel salt, coolant lead and fuel tube. To this end, the coupled-physical modeling using the 1D point-kinetic equations and the 1D energy conservation equations was conducted. Furthermore, the proper numerical solver was selected according to its numerical stability and accuracy for faster reactors. The impacts of the group number, the node number as well as various reactivity feedback coefficients were also assessed. Consequently, the decision was made to build the channel model with 10 axial nodes and 6 groups, which produced 90 ODEs to be solved for each channel.

The investigation for the DFR transient responses were implemented in *Chapter 6*. Here the simulations with different scenarios were separately done on the 10 independent single channels to represent the behavior of the corresponding core sub-regions. Except the conventional transients or accidents like the step-wise insertion of reactivity, fluctuation of pump flow and pump trip, the power production and distribution influenced by the flow velocity of the fuel salt were also evaluated. On the other hand, the simulation for the load-following feature was performed to find out the operation flexibility and safety of the DFR concept. As a result, the capability of self-regulating or safe self-shutdown in channel-scale have been proven, which can be reasonably extended up to the entire core scale of the DFR.

The DFR is a completely new reactor concept thus massive fundamental work still needs to be done. First, the experimental work on the material properties is required, for instance, to obtain more accurate description about the temperature-dependent density of the fuel salt, which is a crucial parameter to the reactor dynamics. Second, more advanced model is needed. The model in present work is the 1D single channel model, which is eventually limited in describing the reactor behavior in a large scale. Therefore, a finer multi-channel model is planned to be developed to take the mass and heat transfer between channels into account. Third, all the fuel salt in the DFR system is circulated directly to a running PPU instead of being used for the power output. This design leads to a result that the behavior of the reprocessing unit can significantly influence the reactor dynamics, thereby designing a PPU including the parameters about the rate of refueling and fission product

removal should be an indispensable preparation for the future study on the DFR.

Molten salt reactor can be the most special and potential reactor type among those GEN-IV reactors, because it not only integrates most advantages of other reactor types in one such as fuel sustainability, online refueling and reprocessing, minimum waste, high temperature, high efficiency, low operating pressure, advanced safety and so on, but also it has its unique inherent safety feature, for instance, the core-melting accident is thoroughly eliminated. So far, there appears to be three technology roadmaps in MSR's development in the future. The first one is the graphite-moderated MSR using $^{232}$Th-$^{233}$U fuel cycle. This type can be regarded as a conservative and mature design, because this design has been technically demonstrated by the MSRE project. The second one is the pool-type molten salt fast reactor (MSFR) using $^{238}$U-$^{239}$Pu fuel cycle. This design has the potential not only for the power production and fuel breeding but also for consuming the waste from the current LWRs. The third one can be the dual fluid reactor (DFR) discussed in this thesis. Therefore, it seems that the MSR offers us diversified options for our future energy demand. On the other hand, most of the MSR projects are nevertheless still in the stage of the theoretical calculations at the moment and only a few of them begin to do some experimental works. Moreover, except massive specific technical problems, such as the salt properties, material improvement and standard code development, there are still others like technology standard and licensing issue, which require great efforts in the future.

# Bibliography


[1] https://www.gen-4.org/gif/jcms/c_42150/molten-salt-reactor-msr (accessed 16.11.2015)

[2] Cottrell, W. B., Hungerford, H. E., Leslie, J. K. and Meem J. L., *Operation of the Aircraft Reactor Experiment* ORNL-1845, 1955

[3] Fraas, A. P., Savolainen, A. W., *Design Report on the Aircraft Reactor Test* ORNL-2095, 1956

[4] Haubenreich, P. N. and Engel, J. R., *Experience with the Molten Salt Reactor Experiment*, Nuclear Application & Technology, Vol. 8, 1970, pp.118.

[5] MacPherson H. G., *The Molten Salt Reactor Adventure*, Nuclear Science and Engineering, Vol. 90, No. 4, 1985, pp.374-380.

[6] Thornton, G., *Introduction to Nuclear Propulsion* GEMP-190a, 1963

[7] http://www.ornl.gov/science-discovery/nuclear-science/research-areas/reactor-technology/advanced-reactor-concepts/fluoride-salt-cooled-high-temperature-reactors, (accessed 25.Jul.2015 )

[8] Andreades, C., Cisneros, A. T., Choi, J. K., Chong, A. Y. K., Fratooni, M., et al. (10) *Technical Description of the "Mark 1" Pebble-Bed Fluoride-Salt-Cooled Hight-Temperature Reactor (PB-FHR) Power Plant*, UCBTH-14-002, 2014, pp. 13

[9] http://flibe-energy.com/, (accessed 25.Jul.2015 )

[10] *Technical White Paper*, Transatomic Power, V 1.0.1, 2014, pp. 3

[11] http://www.the-weinberg-foundation.org/2013/11/01/china-eyes-thorium-msrs-for-industrial-heat-hydrogen-revises-timeline/, (accessed 25.Jul.2015 )

[12] http://www.thoriumenergyreport.org/, (accessed 25.Jul.2015 )

[13] Jérôme Serp and et al. (14), *The Molten Salt Reactor (MSR) in Generation IV: Overview and Perspectives*, Progress in Nuclear Energy, Vol. 77, 2014, pp. 308-319

[14] http://www.world-nuclear.org/info/Current-and-Future-Generation/Molten-Salt-Reactors/, (accessed 25.Jul.2015 )

[15] http://terrestrialenergy.com/imsr-technology/, (accessed 26.Jul.2015)

[16] *Chapter X. MSR-FUJI General Information, Technical Features, and Operating Characteristics* http://www.uxc.com/smr/Library%5CDesign%20Specific/Fuji%20MSR/Papers/MSR-FUJI%20General%20Information,%20Technical%20Features,%20and%20Operating%20Characteristics.pdf, (accessed 16.11.2015)

[17] http://www.world-nuclear.org/info/Nuclear-Fuel-Cycle/Power-Reactors/Small-Nuclear-Power-Reactors/, (accessed 26.Jul.2015)

[18] http://www.uxc.com/smr/uxc_SMRDetail.aspx?key=Fuji%20MSR, (accessed 26.Jul.2015)

[19] http://dual-fluid-reaktor.de/dokumente, (accessed 26.Jul.2015)

[20] http://www.nrc.gov/about-nrc/regulatory/research/safetycodes.html#th, (accessed 28.07.2015)

[21] *TRACE V5.0 Theory Manual - Field Equations, Solution Methods and Physical Models*, U. S. Nuclear Regulatory Commission, 2012, pp. 32

[22] Cantor, S., Cooke, J. W., Dworkin, A. S., Robbins, G. D., Thoma, R. E. et al.(1), *Physical Properties of Molten-salt Reactor Fuel, Coolant and Flush Salts*, ORNL-TM-2316, 1968

[23] Cantor, S., *Density and Viscosity of Several Molten Fluoride Mixtures*, ORNL-TM-4308, 1973

[24] Robertson R. C., *MSRE Design and Operation Report Part I: Description of Reactor Design*, ORNL-TM-0728, 1965

[25] Spinelli, B., *Preliminary Analysis of the MSRE Dynamic Behaviour*, `https://www.politesi.polimi.it/bitstream/10589/2069/3/2010_07_Spinelli.pdf`, (accessed 17.Oct.2015)

[26] Nestor C. W., *MURGATROYD - An IBM 7090 Program for the Analysis of the Kinetics of the MSRE*, ORNL-TM-203, 1962

[27] Nestor C. W., *ZΦRCH - An IBM 7090 Program for the Analysis of Simulation MSRE Power Transients with a Simplified Space-dependent Kinetic Model*, ORNL-TM-345, 1962

[28] Haubenreich, P. N., Engel, J. R., Prince, B. E. and Claiborne, H. C., *MSRE Design and Operations Report Part III: Nuclear Analysis*, ORNL-TM-0730, 1964, pp.137-144

[29] Beall, S. E., Haubenreich, P. N., Lindauer R. B. and Tallackson, J. R., *MSRE Design and Operations Report Part V: Reactor Safety Analysis Report*, ORNL-TM-0732, 1964

[30] Engel, J. R. and Haubenreich, P. N., *Temperature in the MSRE Core during Steady-state Power Operation*, ORNL-TM-0378, 1962, pp.36-46

[31] Haubenreich, P. N. and Engel, J. R., *Safety Calculations for MSRE*, ORNL-TM-0251, 1962

[32] Ball, S. J. and Kerlin, T. W., *Stability Analysis of the Molten-salt Reactor Experiment*, ORNL-TM-1070, 1966

[33] Steffy, R. C. and Wood, P. J., *Theoretical Dynamic Analysis of the MSRE with $^{233}U$ Fuel*, ORNL-TM-2571, 1969

[34] Steffy, R. C., *Experimental Dynamic Analysis of the MSRE with $^{233}U$ Fuel*, ORNL-TM-2997, 1970, pp.9

[35] Prince, B. E. and Engel, J. R., *Temperature and Reactivity Coefficient Averaging in the MSRE*, ORNL-TM-0379, 1962

[36] Kerlin, T. W. and Ball, S. J., *Experimental Dynamic Analysis of the Molten-salt Reactor Experiment*, ORNL-TM-1647, 1966

[37] Poppendiek, H. F. and Palmer, L. D., *Forced Convection Heat Transfer in Pipes with Volume Heat Source within the Fluids* ORNL-1395

[38] Poppendiek, H. F. and Palmer, L. D., *Forced Convection Heat Transfer between Parallel Plates and in Annuli with Volume Heat Source within the Fluids* ORNL-1701, 1954

[39] Holcomb, D. E., Flanagan, G. F., Patton, B. W., Gehin, J. C., Howard, R. L., et al. (1), *Fast Spectrum Molten Salt Reactor Options*, ORNL/TM-2011/105, 2011

[40] Suzuki, N and Shimazu, Y, Reactivity-Initialized Accident Analysis without Scram of a Molten Salt Reactor, *Journal of Nuclear Science and Technology*, Vol. 45, No. 6, (2008) 575-581

[41] Mahadevan, V. S., Ragusa, J. C. and Mousseau, V. A., A Verification Exercise in Multiphysics Simulations for Coupled Reactor Physics Calculations, *Progress in Nuclear Energy*, 55 (2012) 12-32

[42] Cammi, A., Fiorina, C., Guerrieri, C. and Luzzi, L., Dimensional Effects in the Modeling of MSR Dynamics: Moving on from Simplified Schemes of Analysis to a Multi-physics Modeling Approach, *Nuclear Engineering and Design*, 246 (2012) 12-26

[43] Lapenta, G., Mattioda, F. and Ravetto, P., Point kinetic model for fluid fuel systems, *Annals of Nuclear Energy*, 28 (2001) 1759-1772

[44] Cammi, A., Marcello, V. D., Guerrieri, C. and Luzzi, L., Transfer Function Modeling of Zero-power Dynamics of Circulating Fuel Reactors, *Journal of Engineering for Gas Turbines and Power*, 133 (2011) 052916-1-8

[45] Nahla, A. A. and Zayed, E. M. E., Solution of the Nonlinear Point Nuclear Reactor Kinetics Equations *Progress in Nuclear Energy* 52 (2010) 743-746

[46] Taube, M. and Ligou J., Molten Plutonium Chloride Fast Breeder Reactor Cooled by Molten Uranium Chloride, *Annals of Nuclear Science and Engineering*, 1 (1974) 277-281

[47] Krepel, J., Grundmann U., Rohde U. and Weiss F. P., DYN1D-MSR Dynamics Code for Molten Salt Reactors, *Annals of Nuclear Energy*, 32 (2005) 1799-1824

[48] Krepel, J., Rohde U., Grundmann U. and Weiss F. P., DYN3D-MSR Spacial Dynamics Code for Molten Salt Reactors, *Annals of Nuclear Energy*, 34 (2007) 449-462

[49] Wang, S., Rineiski, A. and Maschek, W., Molten Salt Related Extensions of the SIMMER-III Code and its Application for a Burner Reactor, *Nuclear Engineering and Design*, 236 (2006) 1580-1588

[50] He, X., Macián-Juan, R. and Seidl, M., Simulation of the System Dynamics for the Molten Salt Reactor Experiment Using Modified TRACE, *Proceedings of 23th International Conference of Nuclear Engineering*, 17th-21st May, Chiba, Japan, 2015

[51] He, X., Macián-Juan, R. and Seidl, M., Simulation of Reactivity Initialized Transients at Different Power Levels for Molten Salt Reactor Using Modified TRACE, *Proceedings of the International Congress on Advances in Nuclear Power Plants 2015* 3rd-6th May, Nice, France, 2015

[52] *Annual Report of Generation IV International Forum (GIF) 2014*

[53] Institut für Festkörper und Kernphysik, IFK, *Dual Fluid Reactor*, `http://festkoerper-kernphysik.de/dfr.pdf`, accessed 26.08.2015

[54] Huke, A., Ruprecht, G., WeiÃ§bach, D., Gottlieb, S., Hussein, A., et al.(1), A New Reactor and Safety Concept, *Proceedings of the International Congress on Advances in Nuclear Power Plants (ICAPP2015)*, 3rd-6th May, Nice, France, 2015

[55] Kaltiaisenaho T., *Statistical Tests and the Underestimation of Variance in Serpent 2* Research Report VTT-R-00371-14, 2014, pp.5-9

[56] Baehr, H. D. and Stephan, K., (translated by Park, N. J.), *Heat and Mass Transfer*, Springer-Verlag Berlin Heidelberg, printed in Germany, 1998, ISBN 3-540-63695-1

[57] Welty, J. R., Wicks, C. E., Wilson, R. E. and Rorrer, G., *Fundamentals of Momentum, Heat, and Mass Transfer*, 4th Edition, John Wiley & Sons, Inc, printed in U. S., 2001, ISBN 0-471-38149-7, pp.221

[58] Incropera, F. P. and DeWitt, D. P., *Fundamentals of Heat and Mass Transfer*, 5th Edition, John Wiley & Sons, Inc, printed in U. S., 2002, ISBN 0-471-38650-2, pp.407-427

[59] Stacey W. M., *Nuclear Reactor Physics*, 2rd Edition, Wiley-VCH Verlag GmbH & Co. KGaA, Weinheim, 2007, ISBN 978-3-527-40679-1, pp.147

[60] Wang D., Li F., Guo, J., Wei J., Zhang, J., et al. (1), Improved Nodal Expansion Method for Solving Neutron Diffusion Equation in Cylindrical Geometry, *Nuclear Engineering and Design*, 240 (2010) 1997-2004

[61] Todreas N. E. and Kazimi, M. S., *Nuclear Systems I: Thermal Hydraulic Fundamentals*, Taylor & Francis Group LLC, New York, 1990, ISBN 1-56032-051-6

[62] Luzzi, L., Marcello, D.V., Cammi, A., *Multi-Physics Approach to the Modeling and Analysis of Molten Salt Reactors*, Nova Science Publishers, Inc., New York, 2012, ISBN 978-1-6470-000-5

[63] Guerrieri, C., Luzzi, L. and Cammi, A., An Approach to the MSR Dynamics and Stability Analysis, *Progress in Nuclear Energy*, 67 (2013) 56-73

[64] Nicolino, C., Lapenta, G., Dulla, S., and Ravetto, P., Coupled Dynamics in the Physics of Molten Salt Reactors, *Annals of Nuclear Energy*, 35 (2008) 314-322

[65] Wang, X., Seidl, M. and Macián-Juan, R., Preliminary Analysis of Basic Reactor Physics of the Dual Fluid Reactor Concept, *Proceedings of the International Congress on Advances in Nuclear Power Plants 2015*, 3rd-6th May, Nice, France, 2015

[66] Guo, Z., Zhou, J., Zhang, D., Chaudri, K. S., Tian, W., et al.(2) Coupled Neutronics/Thermal-hydraulics for Analysis of Molten Salt Reactor, *Nuclear Engineering and Design*, 258 (2013) 144-156

[67] Desyatnik, V. N., Katyshev, S. F., Raspopin, S. P. and Yu., F. and Chervinskii, Density, Surface Tension and Viscosity of Uranium Trichloride-Sodium Chloride Melts, *Atomic Energy*, 39 (1975) 649-651

[68] Munro, R. G., Material Properties of a Sintered $\alpha$-SiC, *Journal of Physical and Chemical Reference Data*, Vol. 26, No. 5, (1997) 1195-1203

[69] Judd, A. M., *An Introduction to the Engineering of Fast Nuclear Reactors*, Cambridge University Press, New York, 2014, pp.3, ISBN 978-1-107-03464-8

[70] Hairer, E, N$\phi$rsett, S. P. and Wanner, G., *Solving Ordinary Differential Equations I*, Springer-Verlag Berlin Heidelberg, corrected 3rd printing, 2008, ISBN 978-3-540-56670-0

[71] Hairer, E and Wanner, G., *Solving Ordinary Differential Equations II*, Springer-Verlag Berlin Heidelberg New York, corrected 2nd printing, 2002, ISBN 3-540-60452-9

[72] Van den Eynde, G., The Reactor Point-Kinetic Equations: Semi-analytical Methods versus Numerical Methods *Proceedings of the 17th International Association for Mathematics and Computers in Simulation (IMACS)*, Paris, France, 11th-15th July, 2005

[73] Aufiero, M., Cammi, A., Geoffroy, O., Losa, M., Luzzi, L., et al. (2), Development of an OpenFOAM model for the Molten Salt Fast Reactor Transient Analysis, *Chemical Engineering Science*, 111 (2014) 390-401

[74] Sobolev, V., *Database of Thermophysical Properties of Liquid Metal Coolants for GEN-IV*, SCK·CEN-BLG-1069, ISSN 1379-2407, 2010

[75] Janz, G. J., Tomkins, R. P. T., Allen, C. B., Downey, J. R., Gardner, G. L., et al.(2), *NIST Database: Molten Salts: Volume 4, Part 2, Chlorides and Mixtures*, 1976, pp.896-897

[76] Grena-Hardy, C., Thermodynamics of $UCl_3$ Dissolved in Molten Alkali Chlorides, *Journal of Nuclear Materials*, 25 (1968) 337-339